1-28-2015

Strongly Nonlinear Phenomena and Singularities in Optical, Hydrodynamic and Biological Systems

Sergey Dyachenko

Follow this and additional works at: https://digitalrepository.unm.edu/math_etds

Sergey Dyachenko

Mathematics and Statistics

This dissertation is approved, and it is acceptable in quality and form for publication:

Approved by the Dissertation Comitee:

Pavel Lushnikov,   Chairperson

Alexander Korotkevich,

Evangelos Coutsias,

Jean-Claude Diels.

Strongly Nonlinear Phenomena and Singularities in Optical, Hydrodynamic and Biological Systems

by

Sergey Alexandrovich Dyachenko

B.S, Moscow Institute of Physics and Technology, 2007

DISSERTATION

Submitted in Partial Fulfillment of the
Requirements for the Degree of

Doctor of Philosophy
Mathematics

The University of New Mexico

Albuquerque, New Mexico

August, 2014

Acknowledgments

I would like to express my deepest gratitude to my scientific advisor Pavel Lushnikov and my co-advisor Alexander Korotkevich for all the knowledge they have been sharing with me and the extreme patience that they expressed while doing that.

I would like to thank the faculty Department of Mathematics and Statistics at the University of New Mexico, and in particular Natalia Vladimirova, Daniel Appelö, Stephen Lau and Deborah Sulsky who provided a lot of very helpful ideas and discussions.

I would also like to acknowledge all the very helpful discussions from Professors David H. Dunlap and Mansoor Sheik-Bahae from the Physics and Astronomy Department at the University of New Mexico.

Strongly Nonlinear Phenomena and Singularities in Optical, Hydrodynamic and Biological Systems

by

Sergey Alexandrovich Dyachenko

B.S, Moscow Institute of Physics and Technology, 2007

Ph.D., Mathematics, University of New Mexico, 2014

Abstract

Singularity formation is an inherent feature of equations in nonlinear physics, in many situations such as in self-focusing of light nonlinearity is essential part of the model and physical events cannot be captured by linearized equations.

There are nonlinear systems, such as 1D NLSE where singularities in analytic continuation would follow a soliton solution at fixed distances and while it is true that soliton determines the position of all the singularities, it is also true that evolution of singularities determines the solution on the real axis.

Before we go further to discuss 2D problems, we want to be more specific about analytic continuation in a 2D problem: it is well-known that collapse in 2D NLSE is radially symmetric and introducing radial variable $r = \sqrt{x^2 + y^2}$ the problem becomes effectively one-dimensional. If we expand the interval spanned by r from $[0, +\infty)$ to $(-\infty, +\infty)$ and continue all the functions evenly across the origin, it starts to make sense to further expand r to complex plane $\mathbb{C}$ and talk about analytic continuation of functions in $r \in \mathbb{C}$.

In 2D nonlinear Schrödinger equation (NLSE) it is common to think that a singularity appears in finite time, but one can also say that a singularity already exists in the analytic continuation of initial data and at critical time t_c, the singularity touches the real axis and solution reaches its maximal interval of existence. The latter point of view captures evolution in more detail, in particular it allows to ask many questions that would seem quite meaningless if you follow the "philosophy" of a singularity just appearing at a finite time. In particular, one can ask question what is the trajectory of singularity in complex plane and how does the type of singularity change as $t \to t_c$.

For 2D focusing NLSE and Keller-Segel model (KSE) of chemotactic bacteria, the singularities evolve towards the real axis if sufficient conditions are met by initial distribution of laser intensity (NLSE) and bacteria density (KSE) respectively. Well-established conditions are included in the text and are cited upon in corresponding sections. The central subject of this work is the study of onset of singularity towards the real axis in radially symmetric 2D NLSE and 2D reduced KSE models (RKSE [1, 2]) combining two approaches: direct numerical simulations of collapse and asymptotic analysis in the limit $t \to t_c$. The benefit of this two-sided approach is evident when comparing results of classic theory of critical collapse in 2D NLSE (see Refs. [3,4]) to numerical simulations: the collapse exhibits dependence on initial data even when intensity reaches enormous magnitudes and as a result is inconsistent with classical theory (e.g loglog law [5]).

An intervention of numeric approach allowed us to perform sanity checks of many assumptions and estimate regions of applicability of approximations that were used in asymptotic approach and resulted in a new corrected theory that is able to consistently describe the onset of singularity even for moderate-amplitude, developed collapse while still recovering classic theory in the limit $t \to t_c$.

The problem of 2D potential flow of ideal fluid in free surface hydrodynamics

is another example of nonlinear system containing solutions with singularities. The focus of our investigation lies in fully nonlinear travelling waves on the surface of fluid also known as Stokes waves and in particular we are interested in singularities that are present in the analytic continuation of Stokes waves. These waves computed as a part of this dissertation range from linear waves to the limit of extremely nonlinear waves that were never observed before, in addition a predicted phenomenon of parameter oscillation [6, 7] was confirmed for strongly nonlinear waves.

Contents

Contents

Contents

List of Figures

List of Tables

Chapter 1

Introduction

The approach of singularity to the axis is accompanied by dramatic events, such as unbounded growth of intensity in 2D NLSE description of self-focusing in Kerr media, also known as "blow-up" or collapse. Numerous works focus attention to this classical problem in nonlinear science and very detailed reviews can be found in references [3, 4, 9] with the last reference also giving detailed review of application of NLSE to problems of self-focusing and filamentation in plasma. The motivation to approach the problem of collapse in 2D NLSE comes from the fact that despite extensive theory being available, the notorious discrepancy between theory and experiments would deem theory questionable for applications. The combined effort of our group [5] resulted in a significant improvement of the existing theory by incorporating "memory" of initial conditions in the logarithmic corrections to self-similar scaling of collapse. As a result corrected theory becomes reliable even once peak intensity increases tenfold compared to peak intensity of initial condition, while classic theory needs unreasonably large values of intensity to be somewhat accurate. One of the important features of our approach to the problem was a combination of numerics and theoretical analysis that allowed us to validate every step and succeed in correcting existing theory.

In the classical problem of 2D free surface hydrodynamics, the onset of singularity is a very wide problem, and we focused our effort to one of the sides of it - the nonlinear travelling waves on the surface of ideal fluid. Our approach to this problem is largely based on the framework established in the works [10,11] as well as numerous references focused directly on Stokes waves [12–20] and general numerical methods described in [21,22]. The result of this work has been fruitful, in particular we were able to obtain Stokes waves numerically in regimes where nonlinearity becomes dominant, verify parameter oscillations in waves of extreme steepness and even improve the estimate for the steepness of limiting Stokes wave. From the point of view of singularities, we were able to capture the position of leading singularity, identify it as a branch cut and determine its character. The critical exponent for the law of approach of singularity as a function of wave steepness has been determined as well. A big deal of effort was given to determine numerically the jump on the branch cut with hope to shed some light and construct a sound theoretical model of singularities in Stokes waves and current progress seems increasingly fruitful. The results of work performed in this field have been partially published in [8].

The approach of singularity in RKSE model shares many similarities with collapse in 2D NLSE, the quantity that is collapsing in RKSE model is bacteria density and from the physical standpoint is regularized at the scale of size of bacteria, when description in terms of density becomes not applicable. However, until this scale is reached the rapid growth of bacteria density is an adequate model of chemotaxis [23–27] in addition the same model has been applied to clusters of self-gravitating brownian particles such as for instance in cosmic dust clouds [28,29]. In our work on singularity approach we developed a numerical method that employs dynamic adaptive mesh refinement (AMR) based on the self-similar nature of collapse and performed simulations to validate and improve existing theory of collapse in RKSE. The results of this work have been published in [1,2].

Chapter 1. Introduction

The dissertation is organized as follows, the remainder of this introduction describes the ways in which one can arrive to the models described above as well some of the basic facts relevant to these models. After each of the subsections is a reference to the appropriate chapter that contains an extensive review of established theory and results relevant to that model, as well as new results and description of methods by means of which these results were obtained.

In section 1.1, we discuss the application of NLSE in nonlinear optics context and derivation of NLSE from Maxwell's equation. Chapter 2 is entirely dedicated to classical theory of 2D NLSE, the description of new corrected theory, results of simulations and the comparison of existing theory, corrected theory and numerics.

In section 1.2, we formulate the model of free surface hydrodynamics in ideal fluid under the assumption of potential flow. Chapter 3 gives extensive details on the well-established theory as well as entirely new results that were obtained for this model. We give an overview of numerical methods and present results of numerical simulations. Finally, we analyze the obtained solutions from the point of view of singularity locations.

In section 1.3, we discuss a biological system that consists of bacteria in Petri dish that employs chemotaxis to navigate in surrounding media. We state the Keller-Segel system as a description of dynamics and discuss collapse in 2D RKSE as aggregation of bacteria into a colony. Chapter 3 provides detailed investigation into RKSE model and in particular to the properties of collapse in RKSE. We present a theory of collapse that takes into account logarithmic corrections depending on parameters of initial condition and finally provide comparison of theory with numerical simulations.

1.1   Nonlinear Schrödinger equation

Nonlinear Schrödinger equation(NLSE) is an equation of motion for many Hamiltonian systems in the regimes of weak nonlinear interactions. We will give a brief derivation of NLSE from Maxwell equations, that is relevant to describe Kerr effect in nonlinear $\chi^{(3)}$ crystals, however under the assumption of weak nonlinearity NLSE can be derived for water waves, Bose-Einstein condensates and many other systems.

In the absence of free charges and free currents:

$$\nabla \cdot \mathbf{D} = 0, \qquad \nabla \cdot \mathbf{B} = 0,$$

$$\nabla \times \mathbf{E} = -\frac{\partial B}{\partial t}, \qquad \nabla \times \mathbf{B} = \mu_0 \frac{\partial D}{\partial t},$$

where $\mathbf{E}$ is electric field, $\mathbf{D} = \epsilon_0 \mathbf{E} + \mathbf{P}$ is electric displacement vector, $\mathbf{P}$ is polarization of media and $\mathbf{B}$ is magnetic field.

In a regular nonlinear media polarization vector $\mathbf{P}$ can be expanded in Taylor series of $\mathbf{E}$ by introducing the notion of nonlinear susceptibility tensors $\chi_{ij}^{(2)}$, $\chi_{ijk}^{(3)}$ and etc. (See Reference [30]). Assuming that we have a linearly polarized light, we will omit tensor structure of nonlinear susceptibilities $\chi^{(k)}$, $k = 2, \ldots$, one can simply write:

$$\mathbf{P} = P\hat{\mathbf{j}},$$

$$P = P^{(1)} + P^{(2)} + P^{(3)} + \cdots = \epsilon_0 \chi^{(1)} E + \epsilon_0 \chi^{(2)} E^2 + \epsilon_0 \chi^{(3)} E^3 + \ldots,$$

where $P^{(1)}$ is linear polarization and nonlinear polarization can be written as $P^{NL} = P^{(2)} + P^{(3)} + \ldots$ and presents a small correction to linear polarization $P^{(1)}$.

Most nonlinear media are centro-symmetric, thus making $\chi^{(2)}$ zero by symmetry considerations and making $P^{(3)}$ term the first nontrivial correction to polarization. We make use of vector identities and write Maxwell equations in the following form:

$$\nabla^2 E - \frac{n^2}{c^2}\frac{\partial^2 E}{\partial t^2} = \frac{\chi^{(3)}}{c^2}\frac{\partial^2 E^3}{\partial t^2}.$$

We make slowly varying envelope approximation, i.e. we assume that the electric field is a quasimonochromatic wave in which the changes in the envelope profile are on much longer scale than that given by the carrier frequency ω_0:

$$E(\mathbf{r}, t) = A(\mathbf{r}, \omega - \omega_0)e^{-ik_0 z + i\omega_0 t} + c.c.$$

$$\nabla^2 A - 2ik_0 \frac{\partial A}{\partial z} - k_0^2 A + \frac{n^2 \omega^2}{c^2} A = -\frac{3\chi^{(3)} \omega_0^2}{c^2} |A|^2 A,$$

here A is complex amplitude and *c.c.* denotes complex conjugate quantity. Recall that wave number k in media is defined as $k = \frac{n\omega}{c}$, and the slowly varying envelope approximation implies $|\frac{\partial^2 A}{\partial z^2}| \ll |k_0 \frac{\partial A}{\partial z}|$, we have:

$$\nabla_\perp^2 A - 2ik_0 \frac{\partial A}{\partial z} + (k^2 - k_0^2)A + 3\chi^{(3)} \omega_0^2 c^2 |A|^2 A = 0.$$

Taking into account Taylor expansion of $k(\omega)$ and define group velocity as $v_g = \dfrac{d\omega}{dk}$ we have that:

$$k(\omega) = k_0 + \frac{\partial k}{\partial \omega}(\omega - \omega_0) + \frac{1}{2} \frac{\partial^2 k}{\partial \omega^2}(\omega - \omega_0)^2.$$

We introduce direct and inverse Fourier transform(FT) of a function $u(t)$ in time and frequency domains as follows:

$$\hat{u}(\omega) = \int_{-\infty}^{\infty} u(t)e^{-i\omega t}\, dt,$$

$$u(t) = \frac{1}{2\pi} \int_{-\infty}^{\infty} \hat{u}(\omega)e^{i\omega t}\, d\omega.$$

Hence, it is easy to see that taking a derivative in time corresponds to multiplication by $i\omega$ in frequency domain and $k(\omega)$ can be expressed as follows:

$$k(\omega) = k_0 - i\frac{1}{v_g}\frac{\partial}{\partial t} + \frac{1}{2}\left(\frac{1}{v_g^2}\frac{dv_g}{d\omega}\right)\frac{\partial^2}{\partial t^2}.$$

We introduce retarded time $\tau = t - \frac{z}{v_g}$ and obtain the dimensional form of 3D NLSE:

$$\nabla_\perp^2 A - 2ik_0 \frac{\partial A}{\partial z} + \frac{1}{2}\frac{k_0}{v_g^2}\frac{dv_g}{d\omega}\frac{\partial^2 A}{\partial \tau^2} + 3\chi^{(3)}\omega_0^2 c^2 |A|^2 A = 0. \tag{1.1}$$

Further reductions of equation (1.1) are possible and the most common are the paraxial approximations which is done by neglecting the transverse laplacian $\nabla_\perp^2 A$, resulting in 1D NLSE. This reduction and its generalizations are commonly used to simulate pulse propagation in optical fibers, plasma, and describes propagation of nonlinear waves in general nonlinear systems with cubic nonlinearity. This system is integrable with inverse scattering transform [31] leading to global existence of solution (solutions exists for all values z).

Another common reduction of 3D NLSE is done by neglecting group velocity dispersion (GVD) and results in 2D NLSE that governs self-focusing and defocusing of light in Kerr media. We will follow quantum mechanical notation now on, and we will interchange the variable propagation length z with time t:

$$i\frac{\partial \psi}{\partial t} + \nabla^2 \psi + \alpha |\psi|^2 \psi = 0,$$

where $\psi = \psi(x, y, t)$ is a complex function of (x, y) and time t and equation is written in nondimensional form. The coefficient $\alpha = \pm 1$ determines whether it is a focusing NLSE ($\alpha = +1$), or a defocusing NLSE ($\alpha = -1$).

This model has many peculiar features, and has been subject to numerous investigations [4, 9]. This model describes a Hamiltonian system and it admits solutions blowing-up in finite time (focusing case only). Time evolution of solutions approaching blow-up is the central subject of our study. Detailed overview and recent results for focusing NLSE can be found in chapter 2.

1.2   Free Surface Hydrodynamics in Ideal Fluid

The problem of hydrodynamics with free surface is a classical problem in fluid dynamics and has been a subject of extensive study for quite a while. Naturally applications of this model are often associated with water waves in ocean, water wave turbulence

and etc. In this problem we assume an incompressible $2-$dimensional fluid occupies an infinite half-plane and is acted upon by a force of gravity. The surface of the fluid $y = \eta(x, t)$ is a 1-dimensional curve that separates the fluid below and the air above. For all practical purposes the pressure of the air on the surface will be neglected. The flow is assumed to be potential, i.e. the velocity field $v(x, y, t)$ can be written as a gradient of potential $\Phi(x, y, t)$, $v = \nabla \Phi$. The incompressibility condition then requires for $\nabla^2 \Phi = 0$ and the tricky part comes into play from the fact that region occupied by fluid as well as boundary conditions are varying in time. The region and boundary conditions at the surface consist of two equations - the statement of the fact that surface is moving with the fluid

$$\frac{\partial \eta}{\partial t} = \left.\frac{\partial \Phi}{\partial y}\right|_{y=\eta} - \frac{\partial \Phi}{\partial x}\frac{\partial \eta}{\partial x},$$

and Bernoulli equation, stating the balance of forces at the surface $y = \eta(x, t)$:

$$\left.\frac{\partial \Phi}{\partial t}\right|_{y=\eta} = -\frac{1}{2}\left.(\nabla \Phi)^2\right|_{y=\eta} - g\eta.$$

Note, that in order to integrate equations for Φ and η in time one requires the value of normal derivative of Φ at the surface. Dirichlet-Neuman operator comes into play here: given the value of Φ at the surface, it gives the normal derivative $(\nabla \Phi \cdot \mathbf{n})$. The fact that this operator is nonlocal adds to the complexity of the problem.

Hamiltonian structure for free surface hydrodynamics was discovered in 1968 by Zakharov [10]. Following the works [11] we obtain equations of motion from Hamilton's principle and present new discoveries about the structure and properties of propagating solutions known as Stokes waves.

1.3 Keller-Segel model of bacterial aggregation

Another nonlinear model sharing many features of collapse with 2D NLSE is Keller-Segel model of bacterial collapse and can be derived for bacteria that experience

brownian motion superimposed with biased motion via chemotactic influence.

Chemotaxis is a process of secretion and detection of a substance called chemoattractant. This chemoattractant diffuses through media and when detected by other bacteria biases their random walk toward its gradient. Thus chemotaxis acts as nonlocal attraction between bacteria.

The motion of colonies of bacteria is a competition between diffusion and chemotactic attraction.

When averaged, the macroscopic density of bacteria is described by the so-called Keller-Segel model, see e.g., $[25, 27, 32\text{--}45]$ and references therein:

$$\partial_t \rho = D\nabla^2 \rho - \nabla\big[k\rho \nabla c\big], \tag{1.2}$$

$$\partial_t c = D_c\nabla^2 c + \alpha\, \rho, \tag{1.3}$$

where $\rho(\mathbf{r}, t)$ and $c(\mathbf{r}, t)$ are bacterial density and chemoattractant density at a point $\mathbf{r}$ and time t respectively; D and D_c are the diffusion coefficient of bacteria and chemoattractant; and α is the production rate of chemoattractant, the coefficient $k > 0$ characterizes the strength of chemotactic interaction.

The Keller-Segel model is a mean-field approximation of the behavior of a large number of bacteria, and can be derived from the dynamics of individual bacteria using macroscopic averaging over an ensemble of realizations of stochastic bacteria motion. A starting point of the derivation can be, e.g., the description of an ensemble of bacteria as point-wise objects subject to a white noise force, as in Ref. [43]. Such description is most relevant to procaryotic bacteria like *Escherichia coli* with small rigid shapes.

If the initial density of bacteria is low, the bacterial diffusion typically dominates attraction and bacterial density remains low. For instance, a typical time scale for the evolution of a low-density *Escherichia coli* distribution in a petri dish is

about a day [36] (see Figure 3A in Ref. [36]). However, if initial density is high enough, attraction dominates, and bacteria aggregate (see Figure 3B in Ref. [36]). The typical time scale for such aggregation in experiments with *Escherichia coli* is several minutes [36], so aggregation is three orders of magnitude faster and has an explosive character compared to the evolution of bacteria outside the aggregation area. The aggregation is described by the "collapse of bacterial density" in the approximation of the Keller-Segel model (1.2)-(1.3).

The diffusion of chemoattractant is usually much faster than the diffusion of bacteria, i.e., $D/D_c \ll 1$. For instance, $D/D_c \sim 1/40 - 1/400$ for the cellular slime mold *Dictyostelium* [46], and $D/D_c \sim 1/30$ for microglia cells and neutrophils [47,48]. (Here, we refer to bacteria and cell as synonyms.) Thus Eq. (1.3) evolves on a much smaller time scale than Eq. (1.2), so we can neglect the time derivative in (1.3). In addition, we assume that D, D_c, α, and k are constants, and recast all variables in dimensionless form: $t \to t_0 t$, $r \to t_0^{1/2} D^{1/2} r$, $\rho \to (D_c/t_0 \alpha k)\rho$, and $c \to (D/k)c$, where t_0 is a typical timescale of the dynamics of ρ in Eq. (1.2). The resulting system is called the reduced Keller-Segel model:

$$\partial_t \rho = \Delta \rho - \nabla \cdot (\rho \nabla c),$$
$$\Delta c = -\rho, \tag{1.4}$$

The analysis and simulations of bacterial aggregation in the framework of reduced Keller-Segel model is presented in chapter 4.

Chapter 2

Nonlinear Phenomena in Nonlinear Schrödinger Equation

2.1 Introduction to Nonlinear Schrödinger model

2.1.1 NLSE in Hamiltonian framework.

In this section we discuss well-established results that can be also found in many References (e.g. [3, 4]). We consider NLSE as a hamiltonian system and provide some variational ideas, that will help us infer the qualitative properties of solution to NLSE. We start out with the central object, the hamiltonian of NLSE:

$$H = \int |\nabla \psi|^2 d\mathbf{r} - \frac{a}{2} \int |\psi|^4 d\mathbf{r},$$

where $a = \pm 1$ corresponds to focusing and defocusing cases respectively. In this chapter we restrict our discussion to focusing case. NLSE appears as a result of extremizing the above Hamiltonian, so

$$i\partial_t \psi = \frac{\delta H}{\delta \bar{\psi}} = -\Delta \psi - a|\psi|^2 \psi, \tag{2.1}$$

where $\bar{\psi}$ denotes complex conjugate of ψ. The fact that Hamiltonian is sign-indefinite in focusing NLSE leads to the possibility of simultaneous unbounded growth of both kinetic and potential energy with Hamiltonian staying fixed.

We will show now that in addition to Hamiltonian, another conserved quantity exists in NLSE which is often referred to as number of particles (also known as optical power). Consider number of particles defined as $N = \int |\psi|^2 \, d\mathbf{r}$, then the evolution of N in time is given by:

$$\frac{dN}{dt} = \int \left(\psi_t \bar{\psi} + c.c \right) d\mathbf{r} = i \int \left(\bar{\psi} \Delta \psi - \psi \Delta \bar{\psi} \right) d\mathbf{r}$$
$$= i \int \left(|\nabla \psi|^2 - |\nabla \psi|^2 \right) d\mathbf{r} = 0.$$

An object that plays a central role in dynamics of 1D NLSE is called "soliton", the term soliton is coined for an integrable system, but is often loosely used to refer to solitary wave in a hamiltonian system that is known to be not integrable. In this text, we will use terms "soliton" and solitary wave interchangeably to refer to localized solutions of NLSE that have trivial time dependence of the form

$$\psi(r,t) = R(r)e^{i\lambda t}$$

where $R(r)$ is a real-valued function and λ is a constant.

2.1.2 Multidimensional stability of NLS solitons

The possiblity of collapse is tied to the stability of solitons in multidimensional NLSE. Let us consider nonlinear stability of $d-$dimensional solitons by investigating the extrema of hamiltonian. Assume that we have found a soliton solution of NLSE and denote it by $\psi_s(r,t)$; now consider a perturbation of $\psi_s(r,t)$ such that it holds number of particles fixed, i.e.:

$$|\psi(r,t)| = \frac{1}{L^{d/2}} |u(r/L,t)|,$$

$$N[\psi] = \int |\psi(r)|^2 d\mathbf{r} = \int |\psi(r)|^2 r^{d-1} dr = \frac{1}{L^d} \int |u(r/L)|^2 r^{d-1} dr$$

$$= \int |u(r/L)|^2 (r/L)^{d-1} d(r/L) = N[u].$$

The change in L of the perturbed solution in hamiltonian rescales the kinetic and potential energy terms differently (unless $d = 2$, which is treated separately):

$$H[\psi] = \int |\nabla\psi|^2 d\mathbf{r} - \frac{1}{2} \int |\psi|^4 d\mathbf{r}$$

$$= \frac{1}{L^{d+2}} \int |\nabla u(r/L)|^2 r^{d-1} dr - \frac{1}{2L^{2d}} \int |\psi|^4 r^{d-1} dr = \frac{\|\nabla u\|_2^2}{L^2} - \frac{\|u\|_4^4}{L^d}.$$

Hence the extrema is a minimum in $d < 2$ dimensions and soliton has nonlinear stability; in the case $d > 2$ the extrema is a maximum and soliton is unstable.

The borderline case $d = 2$ is called critical, and both kinetic and potential energy terms in hamiltonian have the same scaling. This means that the above analysis cannot give a conclusive answer about the stability of solitons for the case $d = 2$ (the case is often referred to as critical NLSE or NLSE in critical dimensions).

2.1.3 Critical NLSE

In order to find a conclusive answer to the problem of stability of solitons in critical NLSE, we define a positive definite quantity (sometimes called virial) $V = \int r^2 |\psi|^2 d\mathbf{r}$. Recall that $|\psi|^2$ is probability density and is a positive quantity, and hence $V > 0$ and gives the average of square width of a wave packet. If we investigate V_{tt}:

$$V_{tt} = \frac{\partial}{\partial t}\left[\int |\psi|^2 |x|^2 d\mathbf{x}\right] = \frac{\partial}{\partial t}\int |x|^2 \left(\psi_t\bar\psi + \psi\bar\psi_t\right) d\mathbf{x}$$

$$= i\frac{\partial}{\partial t}\int |x|^2 \left(\bar\psi\nabla^2\psi - \psi\nabla^2\bar\psi\right) d\mathbf{x} = 8\left[\int |\nabla\psi|^2 d\mathbf{r} - \frac{1}{2}\int |\psi|^4 d\mathbf{r}\right] = 8H.$$

Since Hamiltonian is a conserved quantity and is uniquely determined by initial data, and V_{tt} prescribes the evolution of average width as follows:

$$V(t) = 4Ht^2 + c_1 t + c_0.$$

As a consequence depending on the sign of the hamiltonian a positive definite quantity will either hit zero at finite time if $H < 0$ or will grow indefinitely if $H > 0$. This leads to the fact that any perturbation of soliton that pushes hamiltonian away from zero, leads to either collapse ($H < 0$) or dispersion into linear waves ($H > 0$). The ground state soliton of critical NLSE is called the Townes ground soliton and has the property of having Hamiltonian $H = 0$ and $N = N_c$. Townes ground soliton is unstable by the discussion above.

Townes ground soliton

Townes ground soliton is a localized solution of a focusing 2D NLSE that has the property of having exactly zero Hamiltonian. It can be found as a solution of NLSE in the form:

$$\psi = R(r)e^{it},$$

with $R > 0$ for ground state soliton. The resulting equation for R is a second-order ODE with boundary conditions:

$$R'' + \frac{1}{r}R' - R + R^3 = 0,$$
$$R'(0) = 0,$$
$$R(0) = R_0,$$

where $R_0 \approx 2.206\ldots$, the value of R_0 and the profile $R(r)$ are found in conjunction using shooting method to satisfy boundary conditions at $r \to \infty$. According to [4], the asymptotic decay of $R(r)$ as $r \to \infty$ is:

$$R(r) = e^{-r}[A_R r^{-1/2} + O(r^{-3/2})],$$
$$A_R \equiv 3.518062\ldots.$$

Also R defines the critical power

$$N_c \equiv 2\pi \int R^2 r\, dr = 11.7008965\ldots \tag{2.2}$$

2.2 Collapse in Critical NLSE

The solution of 2D NLSE with $H < 0$ experiences a finite time collapse and the solution has finite interval of existence $t \in [0, t_c)$, where t_c - denotes the time of collapse. The onset of collapse marks rapid increase in the amplitude and decrease in the width of ψ. However, the growth of amplitude and decrease in width is not independent, in fact they obey a scaling law that is described in the following section.

2.2.1 Adiabatic approximation and Townes soliton

As $t \to t_c$, the collapsing solution of NLSE quickly approaches a cylindrically symmetric profile, and following the results obtained [3], it is convenient to introduce the followng change of variables:

$$\psi(r,t) = \frac{1}{L} V(\rho, \tau) e^{i\tau + iLL_t \rho^2/4}, \tag{2.3}$$

where we use the notation $r = \sqrt{x^2 + y^2}$ and $L(t)$ is a time-dependent width of solution. The new independent variables are:

$$\rho = \frac{r}{L}, \tag{2.4}$$

$$\tau = \int \frac{dt}{L^2}. \tag{2.5}$$

With simple balancing of the terms in NLSE one can easily show that to leading order $L \simeq \sqrt{t_c - t}$, assume that solution to NLSE is written in the form:

$$\psi(r,t) = \frac{1}{L} U(\rho, \tau).$$

In addition, assume that width of solution $L(t) = (t_c - t)^\alpha$, then:

$$i\partial_t \psi + \nabla^2 \psi + |\psi|^2 \psi = i\frac{1}{L^3}\left(\partial_\tau U - L'LU + \nabla_\rho^2 U + |U|^2 U\right) = 0.$$

In order to balance the terms in the parentheses, one has to have $L'L \simeq const$, so that:

$$L'L = \alpha(t_c - t)^{2\alpha-1} \simeq const, \quad \alpha = \frac{1}{2}.$$

With this choice of α, we have:

$$\tau = \int \frac{dt}{L^2} \approx \int \frac{dt}{t_c - t} = \tau_0 - \ln(t_c - t).$$

The instance of collapse is moved to $\tau \to \infty$ with this choice of τ. It is more convenient to work in these so-called selfsimilar or blow-up variables, since instead of having finite time of collapse for ψ, we have a solution $V(\rho, \tau)$ that converges to Townes ground soliton as $\tau \to \infty$.

The transformation (2.3) was inspired by the discovery of an additional conformal symmetry of NLSE which is called the "lens transform" [4, 49, 50]. It follows that $V(\rho, \tau)$ satisfies the following partial differential equation:

$$i\partial_\tau V + \nabla_\rho^2 V - V + |V|^2 V + \frac{\beta}{4}\rho^2 V = 0, \tag{2.6}$$

with

$$\beta = -L^3 L_{tt}. \tag{2.7}$$

As $t \to t_c$, β approaches zero adiabatically slowly and $V(\rho)$ approaches the ground state soliton $R(\rho)$ [4].

2.2.2   New Scaling Law for Collapse

In the limit $t \to t_c$ the solution of (2.6) converges to Townes ground state soliton $R(\rho)$, this implies that the derivative $\partial_\tau V$ in (2.6) is a small correction to other terms.

The excess number of particles in the collapsing core $N_b - N_c$ is proportional to β [4, 51] and we define the collapsing core as a disk of radius $\rho_b = \frac{2}{\sqrt{\beta}}$ and thus:

$$N_b = \int_0^{\rho_b} |V|^2 \rho' \, d\rho',$$

$$\beta \simeq N_b - N_c,$$

and N_c is the critical number of particles.

Refs. [52] and [53] found that the leading order dependence of $L(t)$ has the following square-root-loglog form

$$L \simeq \left(2\pi \frac{t_c - t}{\ln |\ln(t_c - t)|} \right)^{1/2}. \tag{2.8}$$

(Ref. [52] has a "slip of pen" in a final expression, see e.g. [54] for a discussion.) The validity of the scaling (2.8) at $t \to t_c$ was rigorously proven in Ref. [55]. However, numerous attempts to verify the modification of $L \propto (t_c - t)^{1/2}$ scaling have failed to give convincing evidence of the loglog dependence (see e.g. [56, 57]). Lack of validity of loglog law was also discussed in Ref. [4]. Note that without logarithmic modification, the scaling $(t_c - t)^{1/2}$ implies $\beta = const$, $N = \infty$, and infinitely fast rotation of the phase for $r \to \infty$ with $\beta \neq 0$. Thus, the logarithmic modification is necessary and is responsible for the adiabatically slow approach of β to 0.

Following qualitatively some ideas of [2, 58], in the paper [59] we develop the perturbation theory about the self-similar solution of (2.6) with $V \simeq R(\rho)$ and show that the scaling (2.8) dominates only for very large amplitudes and instead of pursuing an unrealistic limit, we show that the perturbation theory agrees with simulations for quite moderate increase of amplitudes (typically ~ 3 times above initial Gaussian pulse) and suggest and verify the following new expression as a practical choice for the experimental and theoretical study of self-focusing:

$$L = [2\pi(t_c - t)]^{1/2} \left(\ln A + 4\ln \frac{\ln A}{3} + \frac{16\ln \frac{\ln A}{3} - 4}{\ln A} + \right.$$

$$\left. + \frac{-28 - \pi^2 c_1 + 80\ln \frac{\ln A}{3} - 32[\ln \frac{\ln A}{3}]^2}{[\ln A]^2} \right)^{-1/2} \tag{2.9}$$

with

$$A = -3^4 \frac{\tilde{M}}{2\pi^3} \ln \left[[2\pi(t_c - t)]^{1/2} \frac{e^{-b_0}}{L(t_0)} \right], \quad \tilde{M} = 44.773\ldots$$

where b_0 is:

$$b_0 = \frac{2\beta_0^2 e^{\frac{\pi}{\sqrt{\beta_0}}}}{\pi \tilde{M}} \left(1 + \frac{4\beta_0^{1/2}}{\pi} + \frac{(20 + \pi c_1)\beta_0}{\pi^2} + \frac{6(20 + \pi c_1)\beta_0^{3/2}}{\pi^3} + \right.$$

$$\left. + \frac{(840 + 42\pi^2 c_1 + \pi^4 c_2)\beta_0^2}{\pi^4} \right).$$

$$c_1 = 4.793\ldots, c_2 = 52.37\ldots,$$

here $\beta_0 = \beta(t_0)$ and $L_0 = L(t_0)$ and the extra parameter t_0 is discussed below.

The introduction of A and b_0 is purely for the sake of brevity and to provide more compact form of the expression (2.9). $L(t)$ is only weakly sensitive to the choice of $t_0 < t_c$ provided t_0 is larger than the smallest time for which the collapsing solution has assumed an approximate self-similar form (2.3).

Figure 2.1 demonstrates poor agreement of loglog law and the excellent agreement between the analytical expression (2.9) and numerical simulations of NLSE (2.1). Figure 2.2 shows the relative error between $L(t)$ obtained from the numerical simulations of NLSE (2.1) and $L(t)$ from equation (2.9). The relative errors decreases with the decrease of $(N - N_c)/N_c$. The only exception is the curve for a significantly larger power $N/N_c = 1.208$ which is formally beyond the applicability of

equation (2.9). Equation (2.9) is derived in the limit $(N - N_c)/N_c \to 0$, as explained below. However, even in the case of $N/N_c = 1.208$ the relative error $\lesssim 6\%$.

To evaluate (2.9) we picked the parameters $L_0 = L(t_0)$ and $\beta_0 = \beta(t_0)$ at time t_0 at the points marked with thick dots in Figures 2.1, 2.1 and 2.2. The time t_0 is chosen, when the amplitude of collapse exceeds the amplitude of initial data by a factor of five, i.e.:

$$\frac{\max\limits_{\mathbf{r}} |\psi(\mathbf{r}, t_0)|}{\max\limits_{\mathbf{r}} |\psi(\mathbf{r}, 0)|} = 5.$$

A different choice of t_0, say when the collapse has grown tenfold compared to the initial data, proves to result in only a minor improvement of dashed lines in the Figure 2.1. As a result we can speculate that the accuracy of the analytical expression 2.9 is weakly dependent on t_0.

2.2.3 Reduction of NLSE collapsing solution to ODE system for $L(t)$ and $\beta(t)$

To determine $\beta_\tau(\beta)$ analytically, we consider the ground state soliton solution $V_0(\beta, \rho)$ of (2.6) given by

$$\nabla_\rho^2 V_0 - V_0 + V_0^3 + \frac{\beta}{4} \rho^2 V_0 = 0. \tag{2.10}$$

The time-dependent solution $V(\beta, \rho)$ of (2.6) can approximated with a stationary solution $V_0(\beta, \rho)$ for $\rho \lesssim 1$.

However, the small but nonzero value of $\partial_\tau V_0 = \beta_\tau \frac{dV_0}{d\beta}$ provides an imaginary contribution to V. To account for the imaginary contribution at the leading order, we allow V_0 to be complex (replacing it by $\tilde{V}_0$), similar to the approach of [4,60]. We

formally add an exponentially small term $i\nu(\beta)\tilde{V}_0$ to (2.10) as follows,

$$\nabla^2\tilde{V}_0 - \tilde{V}_0 + |\tilde{V}_0|^2\tilde{V}_0 + \frac{\beta}{4}\rho^2\tilde{V}_0 - i\nu(\beta)\tilde{V}_0 = 0.$$

The yet unknown $\nu(\beta)$ accounts for the loss of power of $\tilde{V}_0$ by emission into the tail. One can reinterpret the resulting equation as a linear Schrödinger equation with a self-consistent potential $U \equiv -|\tilde{V}_0|^2 - \frac{\beta}{4}\rho^2$ and a complex eigenvalue $E \equiv -1 - i\nu(\beta)$. (This type of nonself-adjoint boundary value problems was introduced by Gamov in 1928 in the theory of α-decay [61].) Assuming $\beta \ll 1$, we identify two turning points, $\rho_a \sim 1$ and $\rho_b \simeq 2/\beta^{1/2}$, at which $Re(E) + U = 0$. Using the WKB (Wentzel-Kramers-Brillouin) approximation we consider the tunneling from the collapsing region $\rho \lesssim 1$ through the classically forbidden region $\rho_a < \rho < \rho_b$, and obtain, similar to [60] that

$$\tilde{V}_0 = e^{-\frac{\pi}{2\beta^{1/2}}}\exp\left[i\frac{\beta^{1/2}}{4}\rho^2 - i\beta^{-1/2}\ln\rho - i\tilde{\phi}_0\right]$$

$$\times \frac{2^{1/2}A_R}{\beta^{1/4}}[\rho^{-1} + O(\rho^{-3})], \quad \tilde{\phi}_0 = const, \quad \rho \gg \rho_b, \tag{2.11}$$

where A_R results from the matching of the asymptotic of R with the WKB solution. We also note that the tail (2.11) is derived in the adiabatic approximation which is valid for large but finite values of radius, $2/\beta^{1/2} \ll r/L \ll A\left(2/\beta^{1/2}\right)$, where $A(t) \gg 1$ is a slowly changing factor in comparison with $L(t)$. Even though for $r/L \gtrsim A\left(2/\beta^{1/2}\right)$ the solution is not self-similar [9,54,62], its large-radius asymptotic has no influence of $L(t)$ and is not considered here.

We define the power (the number of particles) N_b in the collapsing region $\rho < \rho_b$ as

$$N_b = \int_{r<\rho_b L} |\psi|^2 d\mathbf{r} = 2\pi \int_{\rho<\rho_b} |V|^2 \rho d\rho. \tag{2.12}$$

and a flux P beyond the second turning point $\rho_b = 2/\sqrt{\beta}$ as

$$P = 2\pi\rho\left[iVV_\rho^* + c.c.\right]\big|_{\rho=\rho_b},$$

where c.c. stands for complex conjugate terms. From conservation of N, the flux P determines the change of N_b as

$$\frac{dN_b}{d\tau} = -2\pi\rho \left[iVV_\rho^* + c.c. \right], \quad \rho \gg \rho_b, \tag{2.13}$$

where we approximated P at $\rho = \rho_b$ through its value at $\rho \gg \rho_b$ taking advantage of almost constant flux to the right of the second turning point. Using the adiabatic assumption that $\frac{dN_b}{d\tau} = \beta_\tau \frac{dN_b}{d\beta}$, and approximating V in (2.13) by (2.11) we obtain that

$$\beta_\tau = -4\pi A_R^2 \left(\frac{dN_b}{d\beta} \right)^{-1} e^{-\frac{\pi}{\beta^{1/2}}}. \tag{2.14}$$

Recalling the definition of $\nu(\beta)$, one can also find $\nu(\beta) \simeq (2\pi A_R^2/N_b)e^{-\frac{\pi}{\beta^{1/2}}}$ from (2.14).

The next step is to find $\frac{dN_b}{d\beta}$ in (2.14). We based our derivation on a crucial observation that the absolute value $|V(\beta, \rho)|$ of the numerical solution of (2.6) coincides with $V_0(\beta, \rho)$ for $0 \leq \rho \lesssim \rho_b$, as shown in Figure 2.3. the approximation:

$$V_0(\beta, \rho) \simeq R(\rho) + \left. \frac{\partial V(\beta, \rho)}{\partial \beta} \right|_{\beta=0} \beta$$

used previously (see e.g. [4]) is limited to $\rho \ll \rho_b$ because the amplitude c of the tail of V_0 has the essential complex singularity $c \propto e^{-\pi/(2\beta^{1/2})}$ for $\beta \to 0$. Approximating N_b through replacing V in (2.12) by $V_0(\beta, \rho)$ we obtain the following series

$$\frac{dN_b}{d\beta} = 2\pi M \left[1 + c_1\beta + c_2\beta^2 + c_3\beta^3 + c_4\beta^4 + c_5\beta^5 \right], \tag{2.15}$$

where

$$M \equiv (2\pi)^{-1} dN_b/d\beta|_{\beta=0} = (1/4) \int_0^\infty \rho^3 R^2(\rho)d\rho = 0.55285897\ldots$$

and coefficients

$$c_1 = 4.74280, \, c_2 = 52.3697, \, c_3 = 297.436, \, c_4 = -4668.01, \, c_5 = 10566.2$$

are estimated from the numerical solution of (2.10). Here the value of c_1 is obtained from the numerical differentiation:

$$c_1 = (2\pi M)^{-1} \left. \frac{d^2 N_b}{d\beta^2} \right|_{\beta=0}.$$

In principle one can find the coefficients $c_2, c_3, \ldots$ from high order numerical differentiation at $\beta = 0$. However, the radius of convergence of the corresponding Taylor series is $\beta \sim 0.04$. Yet the range of β resolved in our NLSE simulations is $\beta \gtrsim 0.05$ as seen in Figure 2.1.

The usage of Taylor series expansion at $\beta = 0$ would prove inefficient to approximate $\frac{dN_b}{d\beta}$ in (2.15) for $\beta \gtrsim 0.05$. Instead we approximate $c_2, \ldots, c_5$ from the polynomial fit in the range $0.0 < \beta < 0.23$. This procedure gives the numerical values given above. The relative error between the exact value of $\frac{dN_b}{d\beta}$ and the polynomial interpolation (2.15) is $< 1.6\%$ in the range $0 \le \beta < 0.23$. If only c_1 and c_2 are taken into account in (2.15), then the relative error is $< 1.0\%$ in the range $0 \le \beta < 0.09$. Figure 2.1 shows that equations (2.14) and (2.15) approximate well the full numerical solution for $\beta \lesssim 0.18$. Indeed, $\beta_\tau(\beta)$ from (2.14) with $dN_b/d\beta$, obtained either numerically via $V_0(\beta, \rho)$ or by using equation (2.15), are indistinguishable on the plot (they are both shown by the dashed line). The dotted line corresponds to equation (2.15) with only c_1 and c_2 taken into account.

For comparison, the dash-dotted line in Figure 2.1 shows the standard approximation for $\beta_\tau(\beta)$ [4], which corresponds to (2.15) with the expression in square brackets replaced by 1. As we see, the standard approximation fails all way down to $\beta \approx 0.05$. Further decrease of β is unresolvable in our simulations (which typically reach $\max |\psi| \sim 10^{15}$).

From equations (2.4),(2.7),(2.14) and (2.15) we obtain a closed system

$$\frac{d\beta}{d\tau} = -\frac{2A_R^2 e^{-\frac{\pi}{\beta^{1/2}}}}{M(1 + c_1\beta + c_2\beta^2 + c_3\beta^3 + c_4\beta^4 + c_5\beta^5)}, \tag{2.16a}$$

$$\frac{d^2L}{dt^2} = -L^{-3}\beta, \tag{2.16b}$$

$$\frac{d\tau}{dt} = L^{-2}, \tag{2.16c}$$

from which the unknowns $\beta(t)$ and $L(t)$ can be determined. The above system of ODEs can be easily reformulated to exclude variable τ with (2.16c).

2.3   Simulations of 2D NLSE

We performed simulations of radially symmetric NLSE in 2D on a spatial grid that spans a circle $r \in [0, L]$:

$$i\partial_t\psi + \Delta\psi + |\psi|^2\psi = 0,$$

and if we explicitly write down the Laplacian ∇^2 in polar coordinates:

$$i\partial_t\psi + \frac{\partial^2\psi}{\partial r^2} + \frac{1}{r}\frac{\partial\psi}{\partial r} + |\psi|^2\psi = 0. \tag{2.17}$$

These equations have to be supplemented with initial conditions(IC) and boundary conditions(BC) at $r = 0$ and at $r = L$.

BC at the origin come naturally from the regularity of ψ at $r = 0$, we require ψ to be even i.e. $\partial_r\psi|_{r=0} = 0$ and similarly all odd derivatives. In addition, at the origin equation (2.17) has a singular term, which becomes regular only with the assumption that ψ is even:

$$\frac{1}{r}\frac{\partial\psi}{\partial r}\bigg|_{r=0} = \left[\frac{1}{r}\left(\frac{\partial\psi}{\partial r} + r\frac{\partial^2\psi}{\partial r^2}\right) + \mathrm{O}\left(r\right)\right]\bigg|_{r=0} = \frac{\partial^2\psi}{\partial r^2}\bigg|_{r=0}.$$

Hence at the origin we are solving:

$$i\partial_t \psi + 2\frac{\partial^2 \psi}{\partial r^2} + |\psi|^2 \psi = 0,$$

and assume even parity for ψ for all times.

The BC at the boundary of the circle $r = L$ is of lesser importance as long as waves from collapsing core do not have the time to reach the boundary $r = L$ and reflect back to influence the collapse dynamics. We always take the radius circle L large enough for this condition to apply and during the simulation time there is virtually no dynamics for large r and we observe only the tails of IC in this region.

At $r = L$ we are forcing no flow BC:

$$\left.\frac{\partial \psi}{\partial r}\right|_{r=L} = 0.$$

The initial conditions for simulations were picked to be gaussian in the form:

$$\psi(r) = A \exp\left(-\frac{r^2}{\sigma^2}\right). \tag{2.18}$$

The parameter $\sigma = 1$ and values of A were picked so that the resulting gaussian has the number of particles in slight excess of critical number of particles $N_c = 11.7008965\ldots$ in these simulations we picked $A = 2.78$, $A = 2.80$, $A = 2.84$ and $A = 3.00$ which correspond to $\frac{N}{N_c} = 1.0375, 1.0525, 1.0828$ and $\frac{N}{N_c} = 1.208$ respectively.

The simulations were performed using adaptive mesh refinement (AMR) technique [3,63]; spatial derivatives are calculated using 8th order finite difference scheme and complemented with the sixth-order Runge-Kutta time advancement method. The code that was used to perform simulations of NLSE is also used for the simulations of Keller-Segel, it is described in much detail in section 4.3 and [58].

The spatial domain, $r \in [0, L]$, is divided in several nonintersecting uniform subgrids with distinct spatial resolution. The spacing between computational points

is constant for each subgrid, and differs by a factor of two between adjacent subgrids. The rightmost subgrid, farthest from the collapse, has the coarsest resolution; the spatial step decreases in the inward direction. The grid structure adapts during the evolution of the collapse to keep the solution well resolved. When a refinement condition is met, the leftmost subgrid is divided in two equal subgrids with the interpolation of up to 10th order used to initialize the data on the new subgrid.

The solution on all subgrids is evolved with the same timestep, $\Delta t = C_{\text{CFL}} h^2$, where h is the spatial step of the finest grid, and C_{CFL} is a constant. Typically we choose $C_{\text{CFL}} = 0.05$, but we also tested convergence for various values of C_{CFL}.

We will comment on how to find the values of L and β from simulations; first, we compute the value of L as follows:

$$L = \frac{1}{|\psi|} \left(1 + 2\frac{|\psi|_{rr}}{|\psi|^3} \right)^{-1/2} \Bigg|_{r=0}$$

this expression can be derived from the expansion of $V_0(\beta, \rho)$ in Taylor series for $\rho \ll 1$ in (2.10).

Secondly, we determine $\beta(t)$ from a nonlinear condition:

$$|\psi(0, t)| = \frac{1}{L} V_0(\beta, 0)$$

using the pre-computed values of $V_0(\beta, 0)$ from the solution of (2.10). The description of how we obtain the solution to (2.10) is given in section 2.4.1.

We found that this procedure gives much better accuracy in determining L and β than the alternative procedures reviewed e.g. in Ref. [4].

2.3.1 Simulation Challenges

Implications of Collapse

The principle obstacle for simulations arises from the unbounded growth of solution as $t \to t_c$. Consider an eighth order discretization of a second derivative of ψ with a finite difference scheme:

$$\psi_{rr} = D_r^{(2)}\psi + C\psi_r^{(10)}h^8,$$

where $D_r^{(2)}$ is an eighth order central difference stencil for second derivative, and $\psi_r^{(10)}$ is the tenth derivative and h is the spatial step of the grid. Assume now, that the solution is close to blow-up and can be roughly approximated by a rescaled Townes soliton V_0 with $\beta = 0$:

$$|\psi(r)| = \frac{1}{L}V_0(r/L). \tag{2.19}$$

Here $V_0(\rho)$ denotes Townes ground state soliton with $\beta = 0$ and $\rho = \frac{r}{L}$. Hence the relative error in discretization of second derivative is:

$$\epsilon = \frac{||\psi_{rr} - \psi_{rr}^{approx}||}{||\psi_{rr}||} = \frac{Ch^8||V_0^{(10)}||}{L^8||V_0''||}. \tag{2.20}$$

It becomes obvious that if spatial step would remain fixed during the evolution of blow-up, the relative error of discretization of derivative will degrade as $\frac{1}{L^8}$. In order to fix the spatial resolution one would want to hold the ratio h/L fixed during the simulation.

For these qualitative description it is sufficient to define L as

$$L = \frac{1}{|\psi|}\bigg|_{r=0}.$$

And hence $h\,|\psi|\big|_{r=0}$ has to be held fixed. We do not satisfy this criterion at every point in time, but instead we enforce it as follows: once $|\psi(t)|\big|_{r=0}$ increases by a

factor of 2, we refine the spatial grid by a factor of two. The missing points are obtained by interpolation of data in existing points. Refinement is performed on half the length of the existing grid, since the typical width of solution also decreases by a factor of two (2.19). A variant of this type of mesh refinement is also illustrated in Figure 4.5.

2.4 Simulation Results

2.4.1 Finding soliton for $\beta = 0$ and finite β

As one of the crucial steps to investigate time evolution of $\beta(\tau)$ one has to compute highly accurate profile of Townes soliton not only in the limit $\beta \to 0$, but also for finite values of β. In order to obtain these profiles, one has to solve a second order ODE:

$$\nabla_\rho^2 V_0 - V_0 + V_0^3 + \frac{\beta}{4}\rho^2 V_0 = 0. \tag{2.21}$$

However, not every solution of this equation has any physical meaning, in fact there is only a discrete set of solutions that decay as $\rho \to \infty$.

The equation (2.21) is solved with shooting method, since the equation is a second order ODE, one would think that it is necessary to supply the values of $V_0(\beta, 0)$ and its derivative at $\rho = 0$. However, if we recall that regularity of $V_0(\beta, \rho)$ requires even parity in ρ, it becomes obvious that it is only necessary to vary one value on the boundary. I.e. we solve equation (2.21) together with:

$$V_0(\beta, \rho)|_{\rho=0} = v_0,$$
$$\left.\frac{\partial V_0(\beta, \rho)}{\partial \rho}\right|_{\rho=0} = 0.$$

Assume for the sake of clarity that we can solve the equation (2.21) numerically on a semiinfinite interval $\rho \in [0, \infty]$, then one would vary v_0 in such a way that $V_0 \to 0$ as $\rho \to \infty$ and the the resulting solution would be a Townes soliton (for $\beta \geq 0$).

However, for the purposes of numerics we can only have a finite interval $\rho \in [0, \rho_{max}]$. In order to find solution decaying at infinity we would need to somehow enforce the right boundary condition at $\rho = \rho_{max}$. This can be done as follows, starting from a certain value of $\rho_b = \frac{2}{\sqrt{\beta}}$ approximate the solution of (2.21) with the solution of a linearized equation:

$$\nabla^2_\rho V_0 - V_0 + \frac{\beta}{4}\rho^2 V_0 = 0. \tag{2.22}$$

that has 2 linearly independent complex solutions that decay at $\rho \to \infty$ and are expressed in terms of hypergeometric functions. The function $V_0(\beta, \rho)$ is real and has an oscillating tail,

$$V_0(\beta, \rho) = c\rho^{-1} \cos\left[\frac{\beta^{1/2}}{4}\rho^2 - \beta^{-1/2}\ln\rho + \phi_0\right] + O(\rho^{-3}),$$

with $c, \phi_0 = const$ and $\rho \gg 2/\beta^{1/2}$. Here, by ground state soliton V_0, we mean the real function such that it minimizes $|c|$ in the tail. It implies that V_0 has only small amplitude oscillations with $|c| \ll 1$ for $0 < \beta \ll 1$.

2.4.2   Conclusions and Discussion

Our simulations allowed us to compute accurate profiles of the solution ψ up to amplitudes of the order 10^{15} as well as confirm the law of evolution of β in simulations of NLSE.

In these simulations we were able to see that when taking various initial data, the derived parameters β and β_τ quickly converge to the predicted curve, however

no such universality is observed in $L(t)$. The explanation of this startling fact lies in the fact that:

$$\frac{d\beta}{d\tau} = -\frac{2A_R^2 \exp\left(-\frac{\pi}{\beta^{1/2}}\right)}{M(1 + c_1\beta + c_2\beta^2 + c_3\beta^3 + c_4\beta^4 + c_5\beta^5)}$$

is a second order ordinary differential equation (ODE) and requires two initial conditions to find a particular solution. If one wants to go to the limit when $\tau \to \infty$ and expect the dependence on the initial data to vanish, one must note that this happens only for unrealistically large values of amplitude, e.g.:

$$|\psi| \approx 10^{10^{100}}.$$

These unrealistically high values are to be expected since the corrections to the limiting log-log law have double-logarithm nature and hence vary extremely slow.
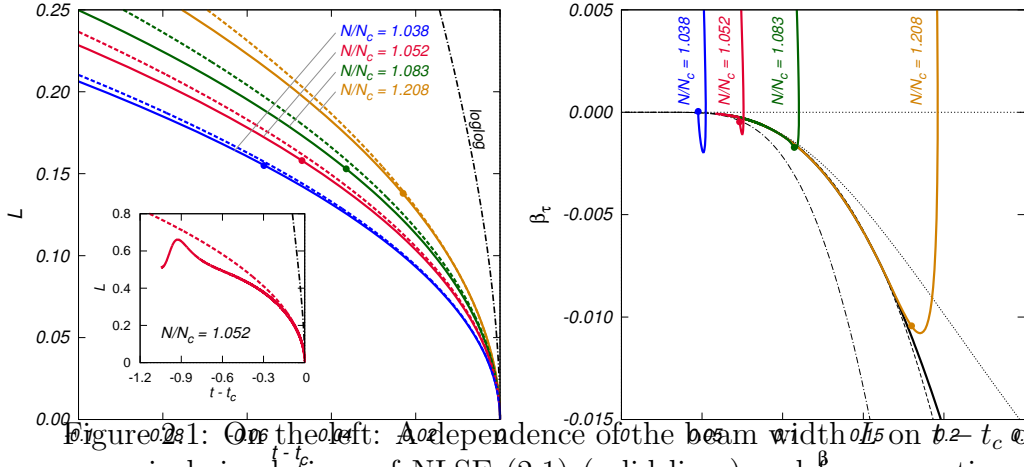
Figure 2.1: On the left: A dependence of the beam width L on $t - t_c$ obtained from numerical simulations of NLSE (2.1) (solid lines) and from equation (2.9) (dashed lines) for different initial conditions. Each pair of closely spaced solid and dashed lines corresponds to the same Gaussian initial condition $\psi(r,0) = pe^{-r^2}$. The curves are labeled by the power $N = \pi p^2/2$ (scaled by the critical power N_c). The dash-dotted line shows L from the loglog law (2.8). The dashed lines are obtained from equation (2.9) using the parameters $L_0 = L(t_0)$ and $\beta_0 = \beta(t_0)$ taken from numerical simulations at locations $t = t_0$. The inset shows $L(t)$ for $N/N_c = 1.052$ starting from the beginning of simulation, $t = 0$. It is seen in the inset that about 2-fold decrease of L compare with the initial value $L(0)$ already produces a good agreement between the simulation of NLSE (2.1) and equation (2.9).

On the right: Solid lines show $\beta_\tau(\beta)$ from numerical simulations of NLSE (2.1) with the same initial conditions as in Figure 2.1. It is seen that the solid curves converge to a single universal $\beta_\tau(\beta)$ curve after the initial transient evolution. The universal curve is independent on initial conditions. Similar to Figure 2.1, the thick dots mark the locations of $t = t_0$ at each solid line, i.e. they indicate the pairs of points $(\beta(t_0), \beta_\tau(t_0))$. The dashed line corresponds to $\beta_\tau(\beta)$ from (2.14) obtained numerically. See also the text for the description of the dash-dotted and dotted lines.
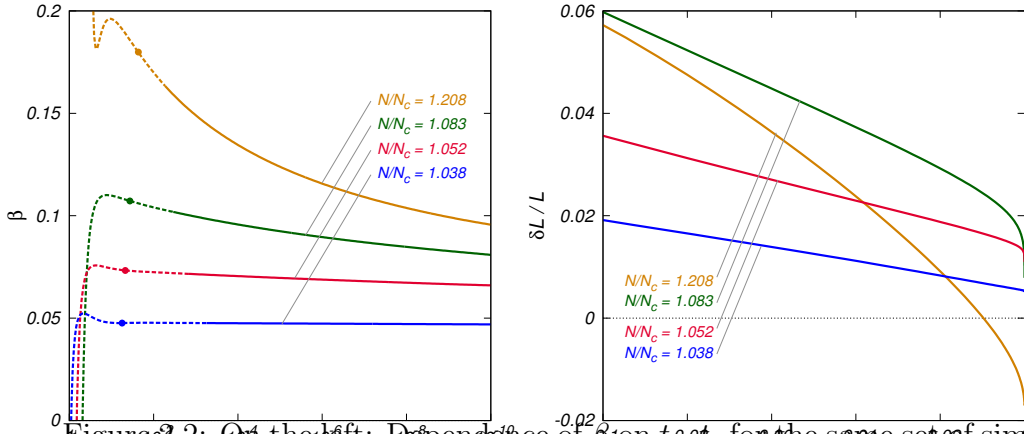
Figure 2.2: On the left: Dependence of β on $t - t_c$ for the same set of simulations as in Figure 2.1. The initial fast evolution is responsible for the formation of the quadratic phase (see equation (2.3)) and is specific to our Gaussian initial conditions with zero phase. The evolution slows down after β passes through the local maximum; the following change in β is especially slow for smaller values of N/N_c. The transitions from dashed to solid lines indicate the collapse of the corresponding $\beta_\tau(\beta)$ curves onto the single universal curve shown in Figure 2.1. The relative difference of 10^{-3} between a particular simulation curve and the universal curve is used as a transition criterium. Similar to Figure 2.1, the thick dots mark the locations of $t = t_0$.

On the right: The relative error, $\delta L/L$, between $L(t)$ obtained from the numerical simulations of NLSE (2.1) and $L(t)$ from equation (2.9) for the same set of simulations as in Figure 2.1. It is seen that the relative errors decreases as $(N - N_c)/N_c$ approaches zero. The exception is the curve for much larger value $N/N_c = 1.208$, where equation (2.9) is formally on the boundary of its range of applicability.
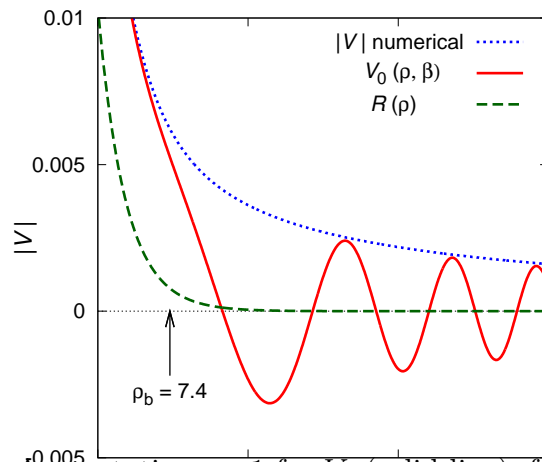
Figure 2.3: Asymptotic $\rho \gg 1$ for V_0 (solid line), full numerical solution $|V|$ (dotted line) and R (dashed line) for $\beta = 0.073$. It is seen that V_0 and $|V|$ almost coincide for $\rho < \rho_b$.

Chapter 3

Nonlinear Phenomena in Free Surface Hydrodynamics

The dynamics of ocean waves has been extensively studies through weak turbulence approach [64] which considers the weak nonlinear interaction of water waves in the approximation of small surface steepness. All current wave forecasting models are based on modified Hasselmann kinetic equation [65] which is the core of the weak turbulence theory. In particular, predicted weak turbulence spectrum for direct cascade of surface gravity waves is ω^{-4}, where ω is the wave frequency, was observed in open field experiments [66,67], as well as in numerous numerical experiments [68–71]. Phillips spectrum ω^{-5} was also observed [72] [71, 73]. In recent works the direct connection between Phillips spectrum and dissipation due to whitecapping was established analytically [74] and it was shown that Phillips spectrum can still be described in the framework of weak turbulence augmented with the additional dissipation [71, 75, 76]. The phenomenological dissipation terms have been used for a long time in wave forecasting models [77, 78]. But the particular expressions of this terms were changing significantly from generation to generation of these models [77, 78]. It suggests that the description of wavebreaking or whitecapping from the

first principles is in need.

3.1   Statement of the Problem

A two-dimensional potential flow of an ideal incompressible fluid with a free surface is described with conformal mapping of a domain occupied by fluid into a complex lower half-plane $\mathbb{C}^-$. We study nonlinear solutions of 2D free surface hydrodynamics in the regimes when nonlinear effects dominate as opposed to the weakly nonlinear regimes (e.g. NLSE in free surface hydrodynamics [10]).

A fully nonlinear gravity wave propagating with constant velocity is known as a Stokes wave and it is going to be the central subject of this chapter with some results for non-trivial time-dependent solutions will be described at the end of this chapter. We will give a brief overview of the mathematical foundations of free surface 2D hydrodynamics and continue on to the new results.

What are Stokes Waves?

As we mentioned before a Stokes wave is a solution of equations of 2D hydrodynamics that propagate with a constant velocity c, i.e. denote the function describing surface elevation by $\eta(x, t)$, then a Stokes wave is a periodic surface elevation with a trivial dependence on time in the form:

$$y = \eta(x, t) \equiv \eta(x - ct).$$

The height of Stokes wave is the difference between the surface elevation at the crest and at the trough, however it is more natural to use a non-dimensionalized parameter that is a height of Stokes wave scaled by its wavelength λ. The increase of the scaled wave height H/λ from the linear limit $H/\lambda = 0$ to the critical value H_{max}/λ marks

the transition from the limit of almost linear wave to a strongly nonlinear limiting Stokes wave. Here H is the wave height and λ is the wavelength.

We performed simulations of fully nonlinear Euler equations reformulated in terms of conformal variables to find Stokes waves for different values of H/λ . We have performed some analysis of analytical structure of Stokes waves and their analytic continuation into the complex plane $\mathbb{C}$.

3.1.1   Equations of motion

In physical coordinates (x, y) a velocity $\mathbf{v}$ of $2D$ potential flow of inviscid incompressible fluid is determined by a velocity potential Φ as $\mathbf{v} = \nabla\Phi$. A closed set of equations is formed by boundary condition at large depth $\Phi(x, y, t)|_{y=-h} = 0$, and kinematic and dynamic boundary condition

$$\frac{\partial \eta}{\partial t} = \left(-\frac{\partial \eta}{\partial x}\frac{\partial \Phi}{\partial x} + \frac{\partial \Phi}{\partial y} \right)\bigg|_{y=\eta(x,t)} \tag{3.1}$$

$$\left(\frac{\partial \Phi}{\partial t} + \frac{1}{2}\left(\nabla\Phi\right)^2 \right)\bigg|_{y=\eta(x,t)} + g\eta = 0 \tag{3.2}$$

at the free surface $y = \eta(x, t)$. We define the boundary value of the velocity potential as $\Phi(x, y, t)|_{y=\eta(x,t)} \equiv \psi(x, t)$.

3.1.2   Conformal Variables and Dirichlet-Neumann problem

We introduce a conformal map of the region occupied by fluid $z = x + iy$, $z \in [-\pi, \pi] \times [-h, \eta]$ to a rectangular domain $w = u + iv$, $w \in [-\pi, \pi] \times [-h, 0]$ on figure 3.1. Because the surface of the fluid η is time-dependent, so is the conformal map $z = z(w, t)$.

The potential $\Phi(z)$ is harmonic $\nabla^2_{x,y}\Phi = 0$ and because $z(w)$ is conformal, so is
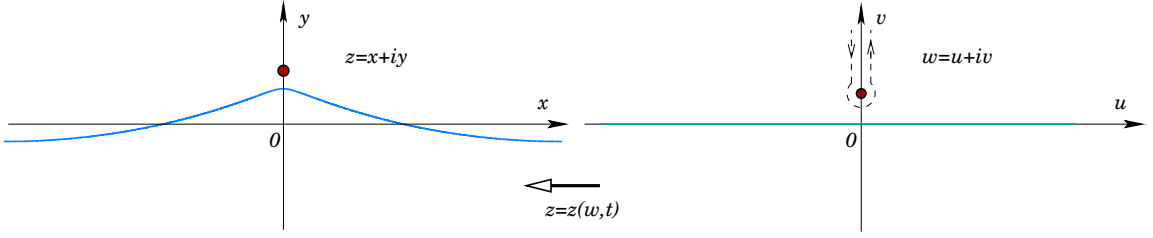
Figure 3.1: Conformal mapping of the region occupied by fluid in physical variables $z = x + iy$, $z \in [-\pi, \pi] \times [-h, \eta]$ to the lower halfplane $\mathbb{C}^-$.

$\Phi(z(w))$. In order to keep notation simple we redefine $\Phi(w) = \Phi(z(w))$ and

$$\nabla^2_{u,v}\Phi = \partial^2_u \Phi + \partial^2_v \Phi = 0.$$

We can solve Laplace equation for $\Phi(u, v)$ with boundary conditions $\partial_v \Phi = 0$ at $v = -h$ and $\Phi = \psi(u)$ at $v = 0$ with much less effort than in original variable z.

$$\Phi(u, v) = \sum \phi_k(v) \exp(iku), \qquad \psi(u) = \sum \hat{\psi}_k \exp(iku),$$
$$\nabla^2 \Phi = \sum (\phi''_k - k^2 \phi_k) \exp(iku),$$
$$\phi_k(v) = a_k \cosh(kv) + b_k \sinh(kv), \qquad \phi_k(0) = \hat{\psi}_k.$$

But $\partial_v \phi_k = 0$ at $v = -h$, then

$$-ka_k \sinh(kh) + kb_k \cosh(kh) = 0,$$
$$b_k = a_k \tanh(kh).$$

So we have:

$$\Phi(u, v) = \sum \hat{\psi}_k (\cosh(kv) + \tanh(kh) \sinh(kv)) \exp(iku). \tag{3.3}$$

Now lets find the harmonic conjugate(stream function) for $\Phi(w)$ and denote it by $\Theta(w)$, by Cauchy-Riemann:

$$\Theta(u, v) = \int \Phi_u dv = i \sum \hat{\psi}_k (\sinh(kv) + \tanh(kh) \cosh(kv)) \exp(iku).$$

At the free surface $v = 0$ this reduces to:

$$\Phi(u, 0) = \sum \hat{\psi}_k \exp(iku),$$

$$\Theta(u, 0) = \sum i \tanh(kh) \hat{\psi}_k \exp(iku),$$

$$\Pi(u, 0) = \Phi(u, 0) + i \left[i \tanh(kh) \right] \Phi(u, 0) = \psi + i \hat{R} \psi,$$

where $\hat{R}$ is multiplication of Fourier coefficients by $i \tanh(kh)$. The problem of finding the appropriate relation between normal derivative $\frac{\partial \Phi}{\partial v}\big|_{v=0}$ and ψ is the essence of Dirichlet-Neumann problem. Here this is done as follows:

$$\frac{\partial \Phi}{\partial v}\bigg|_{v=0} = - \frac{\partial \Theta}{\partial u}\bigg|_{v=0} = -\hat{R}\psi_u, \qquad (3.4)$$

where operator $-\hat{R}\partial_u$ is the Hilbert-Neumann operator. Note that in order for any function $f(w)$ to be analytic in the w, the following relation between its real and imaginary part has to be satisfied:

$$\mathcal{Im} f = \hat{R} \mathcal{Re} f.$$

The statement is a consequence of the uniqueness of solution to the boundary value problem for Laplace equation. Operator inverse to $\hat{R}$ is denoted $\hat{T}$ and is also defined as multiplication in Fourier space, we denote Fourier coefficients of a periodic function $f(u)$ as f_k. Then the following relations follow:

$$\mathcal{F}[\hat{R}f] = R_k f_k = i \tanh(kh) f_k,$$

$$\mathcal{F}[\hat{T}f] = T_k f_k = -i \coth(kh) f_k,$$

$$\mathcal{F}[\hat{T}\hat{R}f] = \mathcal{F}[\hat{R}\hat{T}f] = f_k,$$

here $\mathcal{F}$ denotes Fourier transform. Note that in order for the above relations to work, one has to add an extra restriction on the zero-th Fourier coeficient:

$$f_k = 0 \quad \text{for } k = 0$$

otherwise inverse operator $\hat{T}$ is singular for 0-th Fourier mode.

3.1.3 Hamiltonian framework

Consider an inviscid potential flow in the presence of gravity, then in physical variables Hamiltonian is simply kinetic energy and gravity-induced potential energy:

$$H = T + P = \frac{1}{2} \int dx \int_{-h}^{\eta(x,t)} (\nabla\Phi)^2 dy + \frac{g}{2} \int \eta^2 dx, \tag{3.5}$$

where g is free fall acceleration. The potential energy P is defined on the surface and poses no obstacle to further analysis, but kinetic energy on the other hand involves velocity field in the entire region w, but we want equations of motion only to involve quantities at the free surface. Kinetic energy in the Hamiltonian (3.5) can be simplified by using Green's identity:

$$
\begin{aligned}
T &= \frac{1}{2} \iint_D (\nabla\Phi)^2 dx\,dy \\
&= \frac{1}{2} \int_{\partial D} \Phi(\nabla\Phi \cdot d\Gamma) - \frac{1}{2} \iint_D \Phi \nabla^2 \Phi dx\,dy \\
&= \frac{1}{2} \int_0^{2\pi} (\Phi\Phi_y)|_{y=-h}\,dx + \frac{1}{2} \int_{-h}^{\eta(2\pi)} (\Phi\Phi_x)|_{x=2\pi}\,dy + \\
&\quad + \frac{1}{2} \int_0^{2\pi} \psi\,(\nabla\Phi \cdot \mathbf{n})|_{y=\eta(x)}\,d\mathbf{l} - \frac{1}{2} \int_{-h}^{\eta(0)} (\Phi\Phi_x)|_{x=0}\,dy \\
&= \frac{1}{2} \int \psi(\Phi_x y_u - \Phi_y x_u)|_{v=0}\,du.
\end{aligned}
$$

Expressing Φ_x, Φ_y in terms of Φ_u and Φ_v we find the desired result:

$$T = -\frac{1}{2} \int \psi \hat{R} \psi_u du$$

by virtue of (3.4), also see Reference [79]. Hence hamiltonian can be written in conformal variables as simply:

$$H = T + U = -\frac{1}{2} \int \psi \hat{R} \psi_u du + \frac{g}{2} \int y^2 x_u du \tag{3.6}$$

Here we denote $y = y(u,t)$ and $x = u + \tilde{x}(u,t)$ defined by the conformal map.

Deep Water Equations

We will reduce the the complexity of the problem by taking the limit $h \to \infty$, in this limit we consider surface elevations that are much smaller than the depth of domain. This implies that the previously introduced operator $\hat{R}$ and its inverse $\hat{T}$ converge to:

$$\hat{R} = i \tanh kh \to i \operatorname{sgn} k = \hat{H},$$

$$\hat{T} = i \coth kh \to -i \operatorname{sgn} k = -\hat{H}.$$

Here the operator $\hat{H}$ is a circular Hilbert transform defined as follows:

$$\hat{H}f(t) = \frac{1}{2\pi} \int_{-\pi}^{\pi} f(x) \cot\left(\frac{x - t}{2}\right) dx.$$

The analyticity of z implies that:

$$y = \hat{H}x \quad \text{and} \quad \tilde{x} = \hat{H}y. \tag{3.7}$$

The system (3.1) to (3.2) was originally recast into the conformal variables in Ref. [80] and later independently in Ref. [81] taking the following form [81]:

$$y_t x_u - x_t y_u + \hat{H}\psi_u = 0 \tag{3.8}$$

for the kinematic boundary condition and

$$\psi_t y_u - \psi_u y_t + g y y_u = -\hat{H}\left(\psi_t x_u - \psi_u x_t + g y x_u\right) \tag{3.9}$$

for the dynamic boundary condition. The same equations of motion can also be obtained from extremizing the hamiltonian (3.6). As shown in Ref. [82] these equations can be rewritten as evolution equations for complex $z = x + iy$ and ψ:

$$z_t = z_u(\hat{H} - i)\frac{\hat{H}\psi_u}{|z_u|^2}, \tag{3.10a}$$

$$\psi_t + gy = -\frac{(\psi_u + i\hat{H}\psi_u)^2}{2|z_u|^2}. \tag{3.10b}$$

3.1.4 The Stokes Wave and Its Approximations

The equation for Stokes wave is found by assuming constant speed of propagation in (3.10):

$$z(u,t) = u + \tilde{z}(u - ct), \tag{3.11a}$$

$$\psi(u,t) = \psi(u - ct), \tag{3.11b}$$

where both ψ and $\tilde{z}$ are the periodic functions of $u - ct$. We transform into the moving frame of reference, $u - ct \to u$, and assume that the crest of the Stokes wave is located at $u = 0$ as in Fig. 3.1 and L is the period in u variable for both ψ and $\tilde{z}$ in (3.11). The Stokes solution requires $y(u)$ to be the even function while $\tilde{x}(u)$ needs to be the odd function. Taking into account the periodicity of $\tilde{x}(u)$ in (3.11) it implies that $\tilde{x}(\pm L/2) = 0$. Then the spatial period of the Stokes solution is the same, $L = \lambda$, both in x variable (i.e. for $\eta(x - ct)$) and u variable (i.e. for (3.11)).

It follows from (3.10a) and (3.10b) that $\psi = -c\hat{H}y$ and then excluding ψ from (3.9) we obtain that

$$-c^2 y_u + gyy_u + g\hat{H}[y(1 + \tilde{x}_u)] = 0. \tag{3.12}$$

We now apply $\hat{H}$ to (3.12), use (3.7) to obtain a closed expression for y, and introduce the operator $\hat{k} \equiv -\partial_u \hat{H} = \sqrt{-\nabla^2}$ which results in the following expression

$$\hat{L}_0 y \equiv \left(\frac{c^2}{c_0^2} \hat{k} - 1 \right) y - \left(\frac{\hat{k}y^2}{2} + y\hat{k}y \right) = 0, \tag{3.13}$$

where $c_0 = \sqrt{g/k}$ is the phase speed of linear gravity wave with $k = 2\pi/\lambda$ and we made all quantities dimensionless by the following scaling transform $u \to u\lambda/2\pi$, $x \to x\lambda/2\pi$, $y \to y\lambda/2\pi$. In these scaled units the period of ψ and $\tilde{z}$ is 2π.

3.2 Finding the Stokes Wave

3.2.1 Numerical methods

We solve (3.13) numerically to find $y(u)$ with two different methods each of them beneficial for different range of parameters.

Generalized Petiashvili Method (GPM)

The first method is inspired by a Petviashvili method [83] which was originally proposed to find solitons in nonlinear Schrodinger equation (NLSE) as well as it was adapted for nonlocal NLS-type equations, see e.g. [84]. Here we use a generalized Petviashvili method (GPM) [85] designed to solve the general equation $\hat{L}_0 y \equiv -\hat{M}y + \hat{N}y = 0$ for the unknown function $y(u)$, where $\hat{L}_0$ is the general operator which includes a linear part $-\hat{M}$ and a nonlinear part $\hat{N}$. For our particular form of $\hat{L}_0$ in (3.13) we have that:

$$-\hat{M} = \frac{c^2}{c_0^2}\hat{k} - 1,$$

$\hat{M}$ is invertible on the space of 2π-periodic functions because Stokes wave requires $1 < c^2/c_0^2 < 1.1$ [86]. The convergence of GPM [85] is determined by the smallest negative eigenvalue of the operator $\hat{M}^{-1}\hat{L}$. Here $\hat{L}$ is the linearization operator of $\hat{L}_0$ about the solution y of (3.13):

$$\hat{L}\delta y = -\hat{M}\delta y - \left(\hat{k}(y\delta y) + y\hat{k}\delta y + \delta y\hat{k}y \right).$$

It is assumed that $\hat{M}^{-1}\hat{L}$ has only a single positive eigenvalue 1 determined by $\hat{L}y = \hat{M}y$. GPM iterations [85] are given by:

$$y_{n+1} - y_n = \left(\hat{M}^{-1}L_0 y_n - \gamma \frac{\langle y_n, \hat{L}_0 y_n \rangle}{\langle y_n, \hat{M}y_n \rangle} y_n \right) \Delta\tau, \tag{3.14}$$

where $\Delta\tau > 0$ is the parameter that controls a convergence speed of iterations and $\gamma = 1 + \frac{1}{\Delta\tau}$ is chosen to project iterations into the subspace orthogonal to y (the only eigenfunction y with the positive eigenvalue). In practice this method allowed to find high precision solutions up to $H/\lambda < 0.1388$ as GPM requires significant decrease of $\Delta\tau$ with the growth of H/λ to have convergence.

Newton Conjugate Gradient Method(Newton-CG)

The second method is Newton-CG [21, 87] and is a combination of linearization process and Conjugate Gradient (CG) method for solving the resulting linear system.

The idea of Newton-CG method is simple and aesthetic: first - linearize (3.13) about the current approximation y_n:

$$\hat{L}_0 y_n + \hat{L}_1 \delta y = 0,$$

where

$$\hat{L}_1 = -\hat{M}\delta y - \left(\hat{k}(y_n \delta y) + y_n \hat{k}\delta y + \delta y \hat{k} y_n \right)$$

is a linearization of $\hat{L}_0$ on the current approximation y_n.

As a second step, we solve the resulting linear system for δy with one of our favourite numerical methods, the CG method to obtain next approximation:

$$y_{n+1} = y_n + \delta y$$

It should be noted that monotonic convergence of CG method is proven only for positive definite operators, while in our case $\hat{L}_1$ is indefinite. Nevertheless, both methods were converging to the solutions, and convergence was much faster than when GPM was used.

Newton-CG method can be written in either Fourier space, or in physical space. We considered both cases, however Newton-CG method in physical space requires

six discrete Fourier transforms (DFTs), while if written in Fourier space requires it requires four DFTs per CG/CR step. In addition, the ordering of these four DFTs is such, that they can be performed in parallel on 2 computing threads, this feature is also implemented in our code for numerical simulations of Stokes wave.

An additional performance improvement can be achieved by using a preconditioner matrix. We used a diagonal preconditioner $\hat{M}$ based on the linear part of the operator $\hat{L}_0$. A further performance improvement might be possible with a more elaborate choice of preconditioner.

We found the region of convergence of the Newton-CG method (3.13) to be quite narrow and to require an initial guess $y^{(0)}$ to be quite close to the exact solution y for highly nonlinear waves. In practice we first run GPM and then choose $y^{(0)}$ for Newton-CG methods as the last available iterate of GPM, i.e we start Newton-CG method with the last available Stokes wave computed with GPM and vary velocity parameter c by small amounts.

3.2.2   Simulation Challenges

Before we discuss the simulation challenges, we must mention that the equation (3.12) can be efficiently solved with a spectral method. recall that the application of operator $\hat{k}$ is local in Fourier space and therefore the choice of spectral method for finding Stokes wave comes naturally with the problem. If N is the number of samplng points on u-axis the cost of finding $\hat{k}y$ is $\mathcal{O}(N \log N)$ for spectral method as opposed to $\mathcal{O}(N^2)$ for finite difference method.
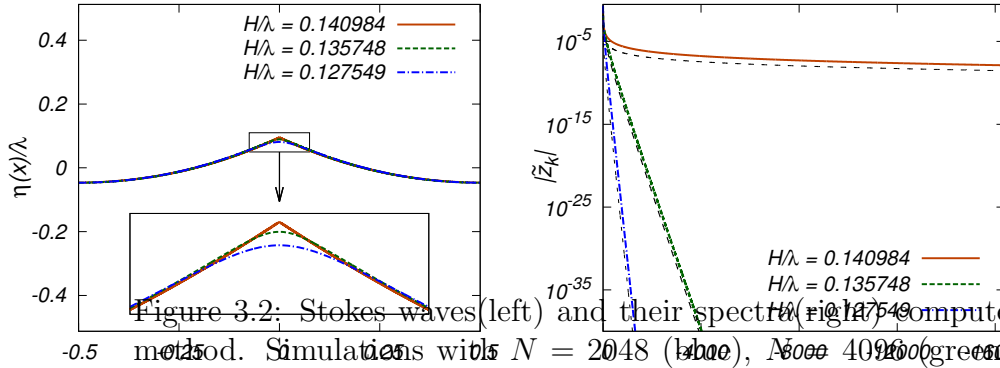
Figure 3.2: Stokes waves (left) and their spectra (right) computed with Newton-CG method. Simulations with $N = 2048$ (blue), $N = 4096$ (green) and $N = 4194304$ (orange) Fourier modes. Black dashed lines are asymptotic decay predicted by theory.

Approximation of a Nearly Singular Profile

An approximation of a function with a singular derivative with Fourier series requires many modes N because the decay of Fourier coefficients is algebraic:

$$\frac{1}{|k|^2} < |f_k| < \frac{1}{|k|} \quad \text{as} \quad |k| \to \infty,$$

in fact in our simulations we used up to $128 \times 2^{20} \approx 128 \times 10^6$ Fourier modes. As a result it becomes essential that the singularities of nonlimiting Stokes waves are close to real axis, but are always at a finite distance v_c from it and hence provide additional exponential decay to Fourier coefficients. In our simulations we were able to reach Stokes waves with $v_c \approx 3.12 \cdot 10^{-7}$, but the everwidening spectrum presents a major obstacle for finding solutions with singularity closer to real axis.

Non-Unique dependence on Velocity Parameter

Secondly, the control parameter c that appears in the equation:

$$\left(\frac{c^2}{c_0^2}\hat{k} - 1\right) y - \left(\frac{\hat{k}y^2}{2} + y\hat{k}y\right) = 0,$$

turns out to be not a monotonic function of steepness H/λ see Figure 3.3. Thus in some range of velocities c, for a single value of c there exists several distinct solutions, therefore having found one of the solutions, we need to have some means of reaching the remaining solutions.

The algorithm of dealing with this problem is as follows: find a solution for a value of c in monotonic region, then go along the curve $c(H/\lambda)$ with small steps in c while using the existing solution with previous value of c as an approximation $y^{(0)}$. When we reach extremum on $c(H/\lambda)$ curve keep the previous value c and as a restart point use the data for this existing c, but perturb it in a special way. Denote the Fourier coefficient for starting approximation with y_k^*, then:

$$y_k^* = y_k e^{|k|\delta},$$

where y_k is the Fourier coefficent of an already computed Stokes wave near the extrema point of $c(H/\lambda)$. A good choice of δ that was typically used in simulations is taking $\frac{\delta}{v_c} \approx 10\%$, where v_c is the distance to singularity of the already computed Stokes wave. The detailed discussion on how to recover the position of singularity from Fourier spectrum in the following section.

Figure 3.3: The propagation speed c as a function steepness H/λ at large scale(left) and zoom-in to the maximum(right).
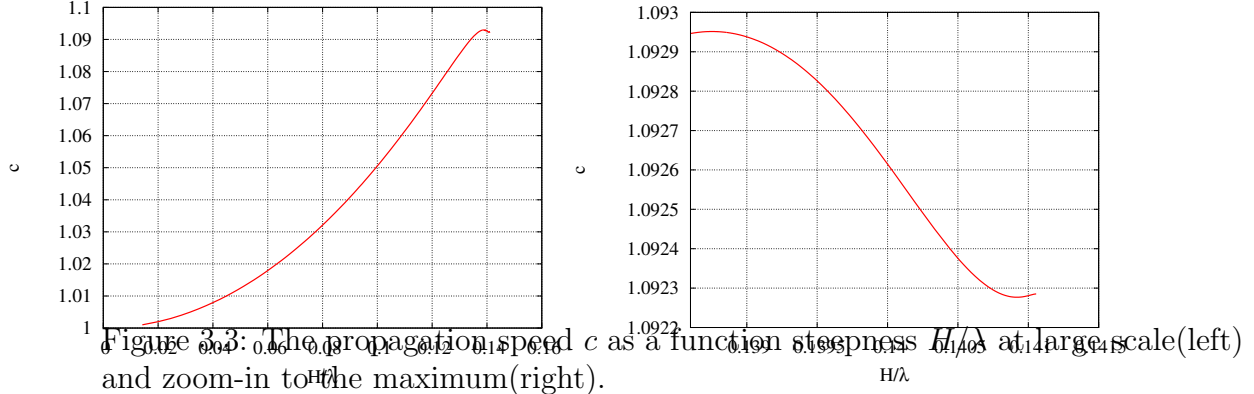
3.2.3   Results

Finding Singularity from Fourier Spectrum

Assume that a singularity of $\tilde{z}$ closest to real axis in w complex plane is a root-type branching point

$$\tilde{z} \simeq c_1(w - iv_c)^\beta, \tag{3.15}$$

as $w \to iv_c$, where c_1 is the complex constant, $v_c > 0$ and β are real constants. By periodicity in u, similar branch points are located at $w = iv_c + 2\pi n$, $n = \pm 1, \pm 2, \ldots$ We expand $\tilde{z}(u)$ in Fourier series:

$$\hat{\tilde{z}}_k = \frac{1}{2\pi} \int\limits_{-\pi}^{\pi} \tilde{z}(u)e^{-iku} \, du, \tag{3.16}$$

$$\tilde{z}(u) = \sum_{k=-\infty}^{0} \hat{\tilde{z}}_k \exp[iku], \tag{3.17}$$

where $\hat{\tilde{z}}_k$ is Fourier coefficient and the sum is taken over nonpositive integer values of k which ensures both 2π-periodicity of $\tilde{z}(u)$ and analyticity of $\tilde{z}(w)$ in $\mathbb{C}^-$. We evaluate (3.16) in the limit $k \to -\infty$ by moving the integration contour from $-\pi < u < \pi$

into $\mathbb{C}^+$ until it hits the lowest branch point (3.15) so it goes around branch point and continues straight upwards about both side of the corresponding branch cut as shown by the dashed line in right panel of Fig. 3.1. Here we assume that branch cut is a straight line connecting $w = iv_c$ and $+i\infty$. Then the asymptotic of $|\hat{\tilde{z}}_k|$ is given by

$$|\hat{\tilde{z}}_k| \propto |k|^{-1-\beta} e^{-|k|v_c}, \quad k \to -\infty. \tag{3.18}$$

In simulations we expand $y(u)$ in cosine Fourier series using FFT to speed up simulations. After that we can immediately recover $\tilde{z}(u)$ by (3.7). We calculated $\tilde{z}(u)$ with high accuracy for different values of H/λ using computations in quad precision (32 digits) to have wide enough dynamic range for Fourier spectrum to recover v_c in (3.18) with high precision. The Figure 3.2 shows the spatial profiles of Stokes waves for several values of H/λ in physical variables (x, y). The Stokes wave quickly approaches the profile of limiting wave except a small neighborhood of the crest.

We have compiled a correspondence of the scaled height of a Stokes wave versus its propagation speed in table 3.1, we assume here that free fall acceleration $g = 1$:

3.3 Analytic Continuation of Stokes Wave

In this section we describe a more powerful tool that we used in combination with Fourier method (described in previous section) to discover the types and positions of singularities of conformal map $z(w)$.

3.3.1   Alpert-Greengard-Hagström Method (AGHM)

In complex analysis there are three types of isolated singularities: poles, removable and essential singularities, as well as all non-isolated singularities (e.g. branch cuts, accumulation points of isolated singularities and etc.).

It is a well known fact that a limiting Stokes wave forms a 120° degree angle at the crest, which corresponds to:

$$\tilde{z}(w) \simeq (iw)^{2/3},$$

and hence a branch-cut type of singularity, in addition according to Ref. [18], the type of singularity relevant for the nonlimiting Stokes wave is also a branch-cut type:

$$\tilde{z}(w) \simeq (iw + v_c)^{1/2}.$$

From a numerical point of view branch cut is a collection of pole-type singularities placed along the curve that is determined by the location of this branch cut. One can obtain the positions and residues of these poles from constructing a Pade approximation of the function $z(w)$ sampled at the real line $w = u + i0$. The main obstacle on this path is the fact that Pade approximation is an ill-conditioned numerical procedure and typically for a function that is known at a uniform grid with double precision, one can expect to find no more than 10 poles with reliable accuracy.

However, there is a way to bypass the ill-posedness of Pade approximation that was discovered by a group of Alpert, Greengard and Hagström [22] originally for the purposes of fast evaluation of convolution for wave propagation equation. This method for finding Padé approximation turned out to be very general and applicable in many scenarios.

The AGHM is an iterative process of computing two polynomials $P^{(i)}(\zeta)$ and

$Q^{(i)}(\zeta)$, so that $\deg Q = \deg P + 1 = d$ and the ratio:

$$\frac{P^{(i)}(\zeta)}{Q^{(i)}(\zeta)} \to \tilde{z}(\zeta) \quad \text{as} \quad i \to \infty$$

in the least square sense, i.e.:

$$\int_{-\infty}^{\infty} \left| \frac{P^{(i)}(\zeta)}{Q^{(i)}(\zeta)} - z(\zeta) \right|^2 d\zeta \to 0 \quad \text{as} \quad i \to \infty. \tag{3.19}$$

Chosen a initial guess $P^{(0)}(\zeta)$ and $Q^{(0)}(\zeta)$ the following L_2-norm is minimized for every i:

$$\min_{P^{(i+1)}, Q^{(i+1)}} \int_{-\infty}^{\infty} \left| \frac{P^{(i+1)}(\zeta)}{Q^{(i)}(\zeta)} - \frac{Q^{(i+1)}(\zeta)}{Q^{(i)}(\zeta)} z(\zeta) \right|^2 d\zeta \tag{3.20}$$

Note, that minimization of (3.20) is a linear weighted least square problem with weight:

$$w^{(i)}(\zeta) = \frac{1}{|Q^{(i)}(\zeta)|^2}$$

The problem (3.20) is solved via Gramm-Schmidt algorithm with reorthogonalization in a C code written with the use multiprecision library called MPFR. It allows to use variable precision arithmetic as opposed to having a fixed double or quadruple precision.

The Application of AGHM to Stokes Wave

In order to have an efficient representation of a periodic function, it is convenient to introduce an extra conformal mapping of the complex plane $w = u + iv$ to $\zeta = \kappa + i\chi = \tan(\frac{w}{2})$. The convenience comes from the property of this map that expands the interval $u \in [-\pi, \pi]$ to the line $\kappa \in (-\infty, \infty)$ and $\chi = 0$.

The application of AGHM to construct Padé approximation to Stokes wave $z(\zeta)$ gave us the results presented on Figure 3.4. It is essential to underline that AGHM

is searching for a rational approximation of $z(\zeta)$ and does no assumption on where the zeros of $Q(\zeta)$ lie, nevertheless as seen on figure 3.4 the positions of the poles lie on the interval of the imaginary line $\chi = \tanh\left(\frac{v}{2}\right) \in [\chi_c, 1]$.

It is necessary to mention here, that after finding the rational approximation $\frac{P(\zeta)}{Q(\zeta)}$ we do a Newton search with zero suppression (see for example Refs. [22, 88]) to find all the zeros of $Q(\zeta)$ which we denote by χ_k with $k = 1, \ldots, d$. The residues at the poles can be found as:

$$\gamma_k = \frac{P(\chi_k)}{Q'(\chi_k)} \quad \text{for} \quad k = 1, \ldots, d$$

Now we can write the form of the surface $z(\zeta)$ as follows:

$$\tilde{z}(\zeta) = z_0 + \sum_{k=1}^{d} \frac{\gamma_k}{\zeta - \chi_k}, \tag{3.21}$$

from the observation of pole locations and residues, we found that $Im(\gamma_k) = 0$ and $Re(\chi_k) = 0$. Here $z_0 = z(u = \pm\pi) = z(\kappa \to \pm\infty)$.

3.3.2 Branch Cut in Stokes Wave

It is only natural to infer that what we are dealing with, is in fact a branch cut between points χ_c and 1 that is being discretized by a finite number of poles. In order to check that assumption, we introduce the spacing between the poles and residue density as follows:

$$\Delta_k = \frac{\beta_{k+1} - \beta_{k-1}}{2},$$
$$\rho(\chi_k) = \frac{\gamma_k}{\Delta_k}.$$

So that the sum (3.21) becomes:

$$\tilde{z}(\zeta) - z_0 = \sum_{k=1}^{d} \frac{\rho(\chi_k)\Delta_k}{\zeta - \beta_k}. \tag{3.22}$$
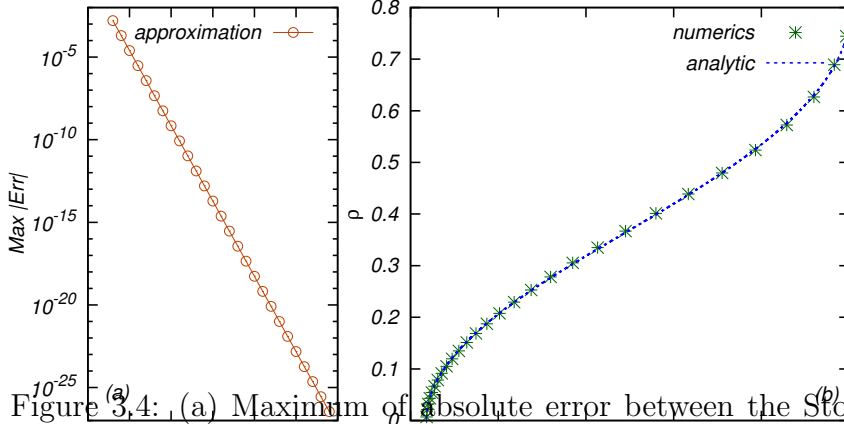
Figure 3.4: (a) Maximum of absolute error between the Stokes wave solution and its approximation by poles as a function of the number of poles for $H/H_{max} = 0.89$, where $H_{max}/\lambda = 0.1410633 \pm 4 \cdot 10^{-7}$ [8]. (b) The density $\rho(\chi)$ from (3.22) along the branch cut of Stokes wave with $\chi = \tanh{(v/2)}$ obtained from the Padé approximation (the asterisks) and the analytical expression (3.24) (the dashed line). The same Stokes wave as in (a) is used.

In order to check that (3.22) really approximates the integral:

$$\tilde{z}(\zeta) - z_0 = \int_{\chi_c}^{1} \frac{\rho(\chi')d\chi'}{\zeta - i\chi'} \approx \sum_{k=1}^{d} \frac{\rho(\chi_k)\Delta_k}{\zeta - i\chi_k}, \qquad (3.23)$$

we reconstruct "residue density" $\rho(\chi)$ using Pade approximants with various number of poles, the result is on the right panel of figure(3.4). The curve for $\rho(\chi)$ appears to be universal in the sense that approximations with distinct number of poles d do approximate the same curve ρ.

The most accurate approximation (black dash-dotted line) was used to evaluate integral in (3.23) and aggreed with the numerical solution of (3.13) up to maximum relative error 0.6%. It also appears that the function $\rho(\chi)$ on Figure 3.4 can be well
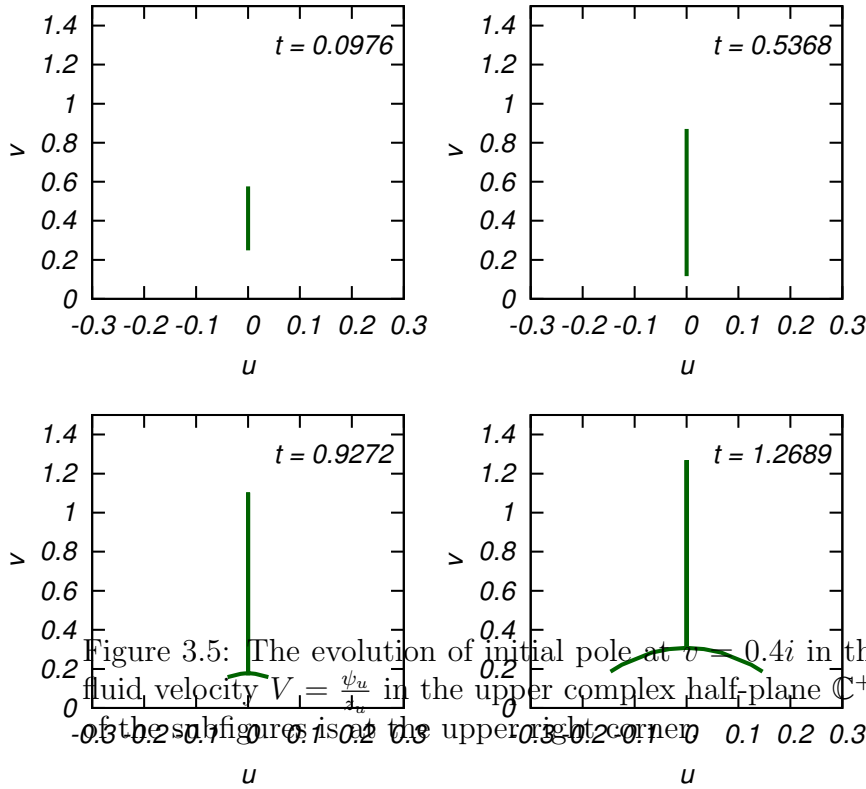
Figure 3.5: The evolution of initial pole at $v = 0.4i$ in the analytic continuation of fluid velocity $V = \frac{\psi_u}{4_u}$ in the upper complex half-plane $\mathbb{C}^+$. The timestamp for each of the subfigures is at the upper right corner

approximated with:

$$\rho(\chi) = 0.5\sqrt{\chi - \chi_c}\left[1 + 0.3(\chi - \chi_c)^{3/2} + 0.43(\chi - \chi_c)^{12}\right]. \tag{3.24}$$

3.3.3 Discussion

Our current effort is concentrated on exploring the properties of $\rho(\chi)$ and writing a closed set of equations to determine the form of $\rho(\chi)$ efficiently from simulations. At this point we have been able to observe the branch cut of a Stokes wave for the first time, we expect that this new knowledge will be crucial to advance the current state

of surface gravity waves.

It turns out that not only Stokes' waves can be efficiently represented as Cauchy integral of the form (3.23), we have been able to observe branch cuts in the full dynamic problem (3.10) and the results of this application of AGHM to surface profiles generated from initial conditions in the form:

$$z(u, t = 0) = u,$$
$$\psi_u(u, t = 0) = \frac{\alpha}{\tan\left(\frac{u}{2}\right) - \beta}.$$

The initial data for ψ_u has to be modified to have zero average, this can be easily done by subtracting the zero Fourier mode from the above expression for ψ_u. The evolution of this initial data is presented in Fig. 3.5

Table 3.1: Correspondence of scaled height H/λ on the propagation speed c and distance to singularity v_c

Scaled height, H/λ	Speed Parameter, c	Distance to Singularity, v_c
0.02012162	1.00200000	1.762552e+00
0.02463768	1.00300000	1.562996e+00
0.02844202	1.00400000	1.421489e+00
0.03179119	1.00500000	1.312058e+00
0.03481678	1.00600000	1.223011e+00
0.03759700	1.00700000	1.148423e+00
0.04018282	1.00800000	1.083616e+00
0.04260965	1.00900000	1.026940e+00
0.04490327	1.01000000	9.761489e-01
0.04708315	1.01100000	9.306224e-01
0.04916445	1.01200000	8.891526e-01
0.05115918	1.01300000	8.512077e-01
0.05307712	1.01400000	8.162184e-01
0.05492632	1.01500000	7.835144e-01
0.05671351	1.01600000	7.534728e-01
0.05844437	1.01700000	7.252296e-01
0.06012378	1.01800000	6.986875e-01
0.06175595	1.01900000	6.737018e-01
0.06334453	1.02000000	6.501227e-01
0.06489273	1.02100000	6.277445e-01
0.06640338	1.02200000	6.064548e-01
0.06787900	1.02300000	5.861442e-01
0.06932183	1.02400000	5.669407e-01
0.07073388	1.02500000	5.485353e-01
0.07211698	1.02600000	5.310017e-01
0.07347277	1.02700000	5.141407e-01
0.07480274	1.02800000	4.979615e-01
0.07610825	1.02900000	4.824516e-01
0.07739057	1.03000000	4.674354e-01
0.07865082	1.03100000	4.530576e-01
0.07989008	1.03200000	4.392083e-01
0.08110931	1.03300000	4.258364e-01
0.08230943	1.03400000	4.129088e-01
0.08349126	1.03500000	4.004457e-01
0.08465559	1.03600000	3.883114e-01

Scaled height, H/λ	Speed Parameter, c	Distance to Singularity, v_c
0.08580316	1.03700000	3.765977e-01
0.08693464	1.03800000	3.652536e-01
0.08805067	1.03900000	3.542630e-01
0.08915185	1.04000000	3.435762e-01
0.09023875	1.04100000	3.332095e-01
0.09131190	1.04200000	3.231437e-01
0.09237181	1.04300000	3.133445e-01
0.09341895	1.04400000	3.038315e-01
0.09445377	1.04500000	2.945603e-01
0.09547670	1.04600000	2.855393e-01
0.09648815	1.04700000	2.767542e-01
0.09748852	1.04800000	2.681845e-01
0.09847817	1.04900000	2.598334e-01
0.09945747	1.05000000	2.516909e-01
0.10042680	1.05100000	2.437387e-01
0.10138640	1.05200000	2.359788e-01
0.10233660	1.05300000	2.283981e-01
0.10327780	1.05400000	2.209485e-01
0.10421020	1.05500000	2.137256e-01
0.10513420	1.05600000	2.066717e-01
0.10605000	1.05700000	1.997542e-01
0.10695780	1.05800000	1.929844e-01
0.10785810	1.05900000	1.863538e-01
0.10875100	1.06000000	1.798635e-01
0.10963680	1.06100000	1.735118e-01
0.11051580	1.06200000	1.672796e-01
0.11138820	1.06300000	1.611740e-01
0.11225430	1.06400000	1.551929e-01
0.11311440	1.06500000	1.493308e-01
0.11396870	1.06600000	1.435654e-01
0.11481750	1.06700000	1.379145e-01
0.11566110	1.06800000	1.323691e-01
0.11649990	1.06900000	1.269190e-01
0.11733400	1.07000000	1.215647e-01
0.11816390	1.07100000	1.163082e-01
0.11898990	1.07200000	1.111338e-01
0.11981230	1.07300000	1.060386e-01
0.12063160	1.07400000	1.010332e-01

Scaled height, H/λ	Speed Parameter, c	Distance to Singularity, v_c
0.12144820	1.07500000	9.610608e-02
0.12226250	1.07600000	9.123957e-02
0.12307530	1.07700000	8.644240e-02
0.12388700	1.07800000	8.171412e-02
0.12469830	1.07900000	7.704094e-02
0.12551020	1.08000000	7.242730e-02
0.12632370	1.08100000	6.785867e-02
0.12713980	1.08200000	6.332992e-02
0.12796020	1.08300000	5.883457e-02
0.12878670	1.08400000	5.436199e-02
0.12962160	1.08500000	4.990466e-02
0.13046840	1.08600000	4.544159e-02
0.13133140	1.08700000	4.095734e-02
0.13221720	1.08800000	3.642195e-02
0.13313620	1.08900000	3.178703e-02
0.13410620	1.09000000	2.698520e-02
0.13516290	1.09100000	2.186251e-02
0.13640310	1.09200000	1.602539e-02
0.13654730	1.09210000	1.536084e-02
0.13669770	1.09220000	1.467261e-02
0.13685580	1.09230000	1.395297e-02
0.13702340	1.09240000	1.319669e-02
0.13720330	1.09250000	1.238734e-02
0.13740030	1.09260000	1.151442e-02
0.13762250	1.09270000	1.054030e-02
0.13788790	1.09280000	9.395095e-03
0.13805100	1.09285000	8.701595e-03
0.13814650	1.09287500	8.300750e-03
0.13825830	1.09290000	7.836464e-03
0.13831020	1.09291000	7.622649e-03
0.13836840	1.09292000	7.383294e-03
0.13843660	1.09293000	7.106173e-03
0.13845190	1.09293200	7.043664e-03
0.13847650	1.09293500	6.944618e-03
0.13849420	1.09293700	6.873736e-03
0.13852300	1.09294000	6.757698e-03
0.13853350	1.09294100	6.715856e-03
0.13854440	1.09294200	6.672045e-03

Scaled height, H/λ	Speed Parameter, c	Distance to Singularity, v_c
0.13855590	1.09294300	6.625942e-03
0.13856820	1.09294400	6.577180e-03
0.13858130	1.09294500	6.525110e-03
0.13859540	1.09294600	6.468929e-03
0.13861090	1.09294700	6.407422e-03
0.13862830	1.09294800	6.338670e-03
0.13864840	1.09294900	6.259224e-03
0.13867340	1.09295000	6.160611e-03
0.13868949	1.09295050	6.097707e-03
0.13869321	1.09295060	6.083053e-03
0.13869718	1.09295070	6.067491e-03
0.13870144	1.09295080	6.050880e-03
0.13870609	1.09295090	6.032383e-03
0.13871124	1.09295100	6.012504e-03
0.13871713	1.09295110	5.989520e-03
0.13872417	1.09295120	5.962265e-03
0.13872497	1.09295121	5.958959e-03
0.13872579	1.09295122	5.955754e-03
0.13872664	1.09295123	5.952427e-03
0.13872752	1.09295124	5.948956e-03
0.13872843	1.09295125	5.948839e-03
0.13873359	1.09295130	5.925136e-03
0.13874890	1.09295138	5.864928e-03
0.13885721	1.09294900	5.448004e-03
0.13887704	1.09294800	5.372150e-03
0.13889408	1.09294700	5.308230e-03
0.13890925	1.09294600	5.250599e-03
0.13893580	1.09294400	5.149782e-03
0.13895891	1.09294200	5.063993e-03
0.13897964	1.09294000	4.986394e-03
0.13901618	1.09293600	4.850091e-03
0.13904816	1.09293200	4.732211e-03
0.13906289	1.09293000	4.678035e-03
0.13912785	1.09292000	4.441287e-03
0.13918299	1.09291000	4.243111e-03
0.13923175	1.09290000	4.070029e-03
0.13927597	1.09289000	3.914791e-03
0.13931673	1.09288000	3.773321e-03

Scaled height, H/λ	Speed Parameter, c	Distance to Singularity, v_c
0.13939057	1.09286000	3.521008e-03
0.13945691	1.09284000	3.299065e-03
0.13951778	1.09282000	3.099485e-03
0.13957447	1.09280000	2.916551e-03
0.13970315	1.09275000	2.516861e-03
0.13977394	1.09272000	2.306013e-03
0.13981918	1.09270000	2.174748e-03
0.13994818	1.09264000	1.815813e-03
0.14011097	1.09256000	1.399834e-03
0.14023135	1.09250000	1.120174e-03
0.14033405	1.09245000	9.018416e-04
0.14044297	1.09240000	6.928041e-04
0.14056584	1.09235000	4.852614e-04
0.14072910	1.09230000	2.587326e-04
0.14075177	1.09229500	2.320759e-04
0.14077749	1.09229000	2.031364e-04
0.14080832	1.09228500	1.703587e-04
0.14083140	1.09228200	1.472677e-04
0.14085073	1.09228000	1.289954e-04
0.14087793	1.09227800	1.048609e-04
0.14090406	1.09227700	8.346459e-05
0.14091552	1.09227685	7.465983e-05
0.14093510	1.09227700	6.042460e-05
0.14095119	1.09227750	4.948919e-05
0.14095779	1.09227780	4.520082e-05
0.14096164	1.09227800	4.278010e-05
0.14097010	1.09227850	3.763332e-05
0.14097744	1.09227900	3.334283e-05
0.14098408	1.09227950	2.961935e-05
0.14099022	1.09228000	2.630538e-05
0.14100153	1.09228100	2.054733e-05
0.14101212	1.09228200	1.559259e-05
0.14102256	1.09228300	1.116077e-05
0.14103365	1.09228400	7.002455e-06
0.14104009	1.09228450	4.889193e-06
0.14104891	1.09228500	2.418847e-06
0.14105203	1.09228510	1.688364e-06
0.14105325	1.09228513	1.428002e-06

Chapter 4

Keller-Segel model of chemotaxis

A reduced Keller-Segel equation (RKSE) is a parabolic-elliptic system of partial differential equations which describes bacterial aggregation and the collapse of a self-gravitating gas of brownian particles. We consider RKSE in two dimensions, where solution has a critical collapse (blow-up) if the total number of bacteria exceeds a critical value. We study the self-similar solutions of RKSE near the blow-up point. Near the collapse time, $t = t_c$, the critical collapse is characterized by the $L \propto (t_c - t)^{1/2}$ scaling law with logarithmic modification, where L is the spatial width of collapsing solution. We develop an asymptotic perturbation theory for these modifications and show that the resulting scaling agrees well with numerical simulations. The quantitative comparison of the theory and simulations requires to take into account several terms of the perturbation series.

4.1 Statement of the Problem

4.1.1 Reduced Model

We consider a reduced Keller-Segel equation (RKSE)

$$\partial_t \rho = \Delta\rho - \nabla \cdot (\rho \nabla c),$$
$$\Delta c = -\rho,$$

$$(4.1)$$

which is a system of partial differential equations for two scalar functions, $\rho = \rho(\mathbf{r}, t)$ and $c = c(\mathbf{r}, t)$. Here $\mathbf{r} \in \Omega \subseteq \mathbb{R}^D$ is the spatial coordinate in dimension D and t is the time. We assume that either $\Omega = \mathbb{R}^D$ or Ω is a bounded domain. For $\Omega = \mathbb{R}^D$, we also assume that both ρ and c decay to zero as $|\mathbf{r}| \to \infty$. In the bounded domain case, we assume the zero flux condition for both ρ and c through the boundary $\partial\Omega$.

Equations (4.1) also describe the dynamics of a gas of self-gravitating Brownian particles and has applications in astrophysics including the problem of stellar collapse [28,29,41,89]. In this case, the second equation in (4.1) is the Poisson equation for the gravity potential, $-c$, while ρ is the gas density. (All units are dimensionless). The first equation in (4.1) is a Smoluchowski equation for ρ. Below we refer to ρ and c as the density of bacteria and the concentration of chemoattractant, respectively, but all results below are equally true for the gravitational collapse of a gas of self-gravitating Brownian particles.

4.1.2 Blow-up criterion

Collapses in NLSE and RKSE have much common, as detailed in Ref. [27]. E.g., the number of particles P in NLSE has a similar meaning to the number of bacteria N in RKSE. One can also recall that $|\psi|^2$ is the probability density in quantum mechanics. In two dimensions ($D = 2$), the critical number of particles, $P_c = 11.70\ldots$

(for NLSE), or the critical number of bacteria, $N_c = 8\pi$ (for RKSE), determine the boundary between collapsing and noncollapsing regimes in both systems [3,25,90–94]. The number of bacteria in 2D RKSE is defined as:

$$N = \int \rho(\mathbf{r}') \, d\mathbf{r}'$$

However, unlike NLSE, the number of bacteria provides not only necessary, but also the sufficient conditions for the existence of collapse. That is if $N > N_c$ collapse is guaranteed, while if $N < N_c$ there is global existence of the solution.

Collapse in the critical dimension $D = 2$ is strong for both RKSE and NLSE, which means that a finite number of bacteria (particles) is trapped within the collapsing core.

For the supercritical case $(D > 2)$, collapse in both RKSE and NLSE is weak meaning that the collapse is so fast that particles (bacteria) cannot keep up with the collapse rate and are escaping the collapsing core. A vanishing number of bacteria (particles) is trapped inside the collapsing region in the limit $t \to t_c$.

4.1.3 Self-Similarity of Blow-up

we focus on the 2D self-similar solution of RKSE, Eq. (4.1). We assume that the spatial location of the collapse is $\mathbf{r} = 0$. Near t_c, in the neighborhood of the collapse, the solution has the following radially symmetric form:

$$
\begin{aligned}
\rho &= \frac{1}{L(t)^2} \frac{8}{(1 + y^2)^2}, \\
c &= -2 \ln(1 + y^2), \\
y &= \frac{r}{L(t)}, \quad r := \mathbf{r}, \\
L(t) &\to 0 \quad \text{for} \quad t \to t_c.
\end{aligned}
\tag{4.2}
$$

Here, $L(t)$ is the time-dependent spatial width of solution. We also refer to $L(t)$ as the collapse width. (We sometimes omit the argument of L for brevity.) The self-similar form (4.2) is valid in the limit $t \to t_c$ in the small spatial neighborhood of the collapse point. This local applicability of the self-similar solution is typical for collapses in numerous nonlinear systems [95].

Several authors proposed different scaling laws for the evolution of L, e.g. [35, 39, 41, 96]. However the common ground in all of them is a logarithmic correction to the $\sqrt{t_c - t}$ law.

$$L(t) = c\sqrt{t_c - t}\, e^{-\sqrt{-\frac{\ln(t_c - t)}{2}}} \left[-\ln\left(t_c - t\right)\right]^{(1/4)(-\ln(t_c - t))^{-1/2}}, \tag{4.3}$$

where c is an unknown constant. This scaling was derived in Ref. [35] using formal matched asymptotic expansion of RKSE near (4.2).

Another scaling law:

$$L(t) = 2e^{-\frac{2+\gamma}{2}}\sqrt{t_c - t}\, e^{-\sqrt{-\frac{\ln(t_c - t)}{2}}}, \tag{4.4}$$

was derived in Refs. [39] and [27]. Here $\gamma = 0.577216\ldots$ is the Euler constant. In Ref. [39], the formal matched asymptotic expansion of RKSE was used. The approach in Ref. [27] was based on the expansion of the perturbation around the collapsing solution (4.2) in terms of the eigenfunctions of the linearization operator. Refs. [39] and [27] give different estimates of errors.

And yet another scaling law,

$$L(t) = c\sqrt{t_c - t}\, e^{-\frac{1}{2}\sqrt{-\frac{\ln(t_c - t)\ln[-\ln(t_c - t)]}{2}}}, \tag{4.5}$$

where c is an unknown constant, was obtained in Ref. [41] by somewhat heuristic arguments.

Chapter 4. Keller-Segel model of chemotaxis

We perform high-precision simulations and show that the onset of blow-up expresses logarithmic-type corrections, that are dependent on the structure of initial data. We derive a new scaling law that agrees with direct simulations of RKSE.

Our *first main result* is that $L(t)$ is determined by the solution of the following ordinary differential equation (ODE):

$$
\begin{aligned}
\frac{\partial_\tau a}{a^2} &= -\frac{2}{\ln\frac{1}{a}} + \frac{M}{(\ln\frac{1}{a})^2} + \frac{b_0}{(\ln\frac{1}{a})^3} + O\left(\frac{1}{(\ln\frac{1}{a})^4}\right), \\
M &= -2 - 2\gamma + 2\ln 2, \\
b_0 &= \frac{\pi^2}{3} - 2\ln^2 2 + 4\ln 2 + \gamma(-4 - 2\gamma + 4\ln 2).
\end{aligned}
\tag{4.6}
$$

The adiabatically slow quantity

$$
a = -L(t)\partial_t L(t), \tag{4.7}
$$

evolves over a new time scale described by a new variable, τ, defined as

$$
\tau = \int_0^t \frac{dt'}{L(t')^2}. \tag{4.8}
$$

Here and below, the notation $f(x) = O(x)$ means that there exists a positive constant c such that $|f| \le c|x|$ as $x \to 0$. It follows from (4.8) that $\tau \to \infty$ as $t \to t_c$, so that $\tau(t)$ maps the collapse time $t = t_c$ into $\tau = \infty$ in full analogy with the "lens transform" of NLSE [4, 49, 50]. The decrease of $L \to 0$ as $t \to t_c$ implies that $a > 0$, and the logarithmic modification of $L(t) \propto \sqrt{t_c - t}$ scaling results in $a \to 0$ as $t \to t_c$. The logarithmic modification also makes a a slow function of $(t_c - t)^{1/2}$, compared with L. These scalings, as well as the definition of a, are in qualitative analogy with the scaling for NLSE collapse.

Our *second main result* is that the asymptotic solution of (4.6) in the limit $t \to t_c$,

together with (4.7) and (4.8), is given by

$$
\begin{aligned}
L(t) &= 2e^{-\frac{2+\gamma}{2}}\sqrt{t_c - t}\,\exp\Big\{-\sqrt{-\tfrac{\ln\beta(t_c-t)}{2}} + \tfrac{-1+b\ln x}{2x} \\
&\quad + \tfrac{-1+2b+2\tilde{M}(1-b\ln x)}{4x^2} + O\left(\tfrac{1}{x^2}\right) + O\left(\tfrac{(\ln x)^2}{x^3}\right)\Big\}, \\
x &= \sqrt{-2\ln\beta(t_c - t)} - \tilde{M}, \\
\tilde{M} &= -2 - \gamma + \ln 2, \\
b &= 1 + \tfrac{\pi^2}{6}, \\
\beta &= 2\exp\Big\{2l^* - \tfrac{\tilde{M}^2}{2}\Big\}, \\
l^* &= -\ln L_0 - \tfrac{1}{4}\ln^2 a_0 + \tfrac{\tilde{M}+1}{2}\ln a_0 - \tfrac{b}{2}\left(\ln\ln\tfrac{1}{a_0} + \tfrac{1}{\ln\frac{1}{a_0}}\right), \\
L_0 &:= L(t_0), \quad a_0 := a(t_0) = -L(t_0)\partial_t L(t_0).
\end{aligned}
\tag{4.9}
$$

This scaling was presented without derivation in Ref. [2]. The time $t = t_0 < t_c$ is chosen arbitrarily, provided that at $t = t_0$, the solution is close to the self-similar form (4.2). (More details about choice of t_0 are given in Figure 4.1.) It is seen from (4.9) that $L(t)$ depends on the initial values $L(t_0)$ and $\partial_t L(t_0)$. The order of error terms in (4.9) are discussed below, after Eq. (4.78).

Our *third main result* is the comparison of (4.9) with direct numerical simulations of RKSE. Figure 4.1 shows excellent agreement between the theory and simulations. In the limit $t \to t_c$, the new scaling (4.9) reduces to (4.4). We demonstrate, however, that while (4.4) is asymptotically correct, it is in quantitative agreement with both (4.9) and simulations only for unrealistically small values

$$
L \lesssim 10^{-10000}.
\tag{4.10}
$$

In contrast, the scaling (4.9) is accurate starting from a moderate decrease of $L(t)$ from the initial value $L(0)$. Figure 4.2 shows the simulation with $N = 1.0250N_c$, where (4.9) is accurate (with the relative error $\lesssim 7\%$) for $L(t)/L(0) \lesssim 0.15$.

4.2 Self-similar collapsing solution of the 2D reduced Keller-Segel equation

2D RKSE (4.1) is invariant under the scaling transformations $\rho(\mathbf{r}, t) \to \frac{1}{L^2}\rho(\frac{1}{L}\mathbf{r}, \frac{1}{L^2}t)$, $c(\mathbf{r}, t) \to c(\frac{1}{L}\mathbf{r}, \frac{1}{L^2}t)$ for any $L(t) \equiv L = const > 0$. The static solution to RKSE is easily obtained by assuming radial symmetry and setting time-derivative to zero in equation (4.1):

$$\rho_0 = \frac{8}{(1+r^2)^2},$$
$$c_0 = -2\ln(1 + r^2), \tag{4.11}$$

which corresponds to the critical number of bacteria, $N(\rho_0) = N_c = 8\pi$. This property is another striking similarity with the ground state soliton solution $\psi = R(r)e^{it}$, $R(r) \geq 0$ of NLSE containing exactly the critical number of particles, $P_c = \int R^2 d\mathbf{r}$.

Assume that collapse is centered at $r = 0$. Then the solution of RKSE in the limit $t \to t_c$ approaches a radially-symmetric, self-similar solution. The self-similar solution has the form of the rescaled stationary solution (4.11) with a time-dependent scale (the collapse width) $L(t)$:

$$\rho(r, t) = \frac{1}{L(t)^2}\rho_0\left(\frac{r}{L(t)}\right),$$
$$c(r, t) = c_0\left(\frac{r}{L(t)}\right). \tag{4.12}$$

The scale $L(t)$ approaches zero for $t \to t_c$.

To describe the radially-symmetric solution we introduce the new dependent variable m as follows,

$$m(r, t) = \frac{1}{2\pi}\int_{|r'| \leq r} \rho(\mathbf{r}', t) \, d\mathbf{r}', \tag{4.13}$$

which allows us to rewrite RKSE as the closed equation for m [35]:

$$\partial_t m = r\partial_r r^{-1}\partial_r m + r^{-1}m\partial_r m. \tag{4.14}$$

Here, $m(r,t)$ has the meaning of the mass (the number of bacteria) inside the circle of radius r (up to a factor 2π). Boundary condition for m at $r \to \infty$ is simply related to the total number of bacteria: $m|_{r=\infty} = N/(2\pi)$. In contrast to RKSE, Eq. (4.14) is PDE for m. This simplification is possible only for radially-symmetric solutions of RKSE.

In terms of m, the steady state solution (4.11) of RKSE takes the following form:

$$m_0 = \frac{4r^2}{1+r^2}, \tag{4.15}$$

and the self-similar solution (4.12) becomes

$$m_{selfsimilar} = \frac{4y^2}{1+y^2}, \qquad y = \frac{r}{L}. \tag{4.16}$$

The boundary condition at infinity gives the critical number of bacteria,

$$2\pi m_{selfsimilar}\big|_{y\to\infty} \to 8\pi = const,$$

It also indicates that bacterial collapse is strong in the sense that the number of bacteria trapped within the collapsing region is nearly constant.

Assuming a power law dependence $L(t) \propto (t_0 - t)^\beta$ of the collapse width in the self-similar solution (4.16) one concludes that all terms in Eq. (4.14) are of the same order provided $\beta = 1/2$, which is similar to NLSE where also the collapsing width $\propto (t_0-t)^{1/2}$. Like for NLSE, the self-similar solution (4.16) is not an exact solution of Eq. (4.14). To account for the difference, it is necessary to consider the logarithmic correction to $L(t) \sim (t_0 - t)^{1/2}$: $L = (t_0 - t)^{1/2}f(\ln(t_0 - t))$, where $f(\ln(t_0 - t))$ is a slow function compared with $(t_0 - t)^{1/2}$. This slow function comes from the nearly exact balance between linear and nonlinear terms of RKSE (between diffusion and

attraction). The same slow function allows to introduce a small parameter a, defined in (4.7), which is a slow function of $(t_0 - t)^{1/2}$ compared with L. The balance between linear and nonlinear terms of RKSE improves with decrease of $a \to 0$.

Based on the analogy with the critical NLSE, we introduce in Eq. (4.14) the new independent "blow up" variables [45]:

$$
\begin{aligned}
y &= \frac{r}{L}, \\
\tau &= \int_0^t \frac{dt'}{L(t')^2}.
\end{aligned}
\tag{4.17}
$$

These new variables transform Eq. (4.14) into the equation for a new unknown function

$$
\varphi(y, \tau) \equiv m(r, t)
\tag{4.18}
$$

into the following equation

$$
\partial_\tau \varphi = y \partial_y (y^{-1} \partial_y \varphi) + y^{-1} \varphi \partial_y \varphi - a y \partial_y \varphi,
\tag{4.19}
$$

where a is given by (4.7). The advantage of working in blow up variables is that the collapse occurs at $\tau = \infty$ instead of $t = t_c$, so that the collapse time t_c is eliminated from consideration. Also, the function φ has bounded derivatives.

Figures 4.3a,b shows that as $t \to t_c$, the density $\rho(r)$ grows near $r = 0$ while the tail of $\rho(r)$ is practically frozen for $r \gtrsim 3$ (on a timescale of collapse). In contrast, the solution in the blow up variables is steady at $y \lesssim 1$ and is well-approximated by (4.11) and (4.12), as shown in Figure 4.3c,d. It is also seen that the deviation of solution from (4.11) moves away from the origin $y = 0$ as $t \to t_c$.

Based on our assumption that a is a slow function, it is natural to look at the solutions of Eq. (4.19) in the adiabatic approximation where one can neglect τ-derivative in the left-hand side (lhs) of Eq. 4.19. Then, assuming that $|a| \ll 1$, one can expand the solution of (4.19) in powers of a starting from (4.16) for the power

zero. Unfortunately, the term $-ay\partial_y\varphi$ grows with y and violates the expansion for large y. So, the adiabatic approximation can only work locally and is restricted to not very large y, a situation which is familiar from the analysis of collapse in NLSE. This however does not create a problem because the behavior at large y does not affect the self-similar solution near zero.

It is convenient to present a general solution of Eq. (4.19) in the following form [45]:

$$\varphi(y,\tau) = \frac{4y^2}{1+y^2} + e^{\frac{a}{4}y^2}\frac{y^2}{y^2+1}v(y,\tau), \tag{4.20}$$

where $v(y,\tau)$ includes all corrections with respect to the self-similar solution (4.16). Here, the factor $e^{\frac{a}{4}y^2}$ (which plays a role of a gauge transform) is inspired by a somewhat similar factor $e^{-i\frac{a}{4}y^2}$ in the self-similar solution of NLSE [3]. However, the absence of $-i$ in the exponent makes RKSE case quite distinct from NLSE case.

Substitution of (4.20) into (4.19) gives the following equation:

$$\partial_\tau v + \hat{\mathcal{L}}_a v = F. \tag{4.21}$$

Here

$$\hat{\mathcal{L}}_a = -\frac{1}{y^3}\partial_y y^3 \partial_y - \frac{8}{(1+y^2)^2} + \left[\frac{a^2}{4}y^2 - 2a + \frac{2a}{1+y^2}\right] \tag{4.22}$$

is the linear operator corresponding to the linearization of (4.19) with respect to (4.16). █ The right-hand side,

$$F = -\frac{\partial_\tau a}{4}y^2 v - \frac{8a}{y^2+1}e^{-ay^2/4} + \frac{ay^2 v^2}{2(y^2+1)}e^{ay^2/4} +$$
$$+ \frac{2v^2}{(y^2+1)^2}e^{ay^2/4} + \frac{yv\partial_y v}{y^2+1}e^{ay^2/4} \tag{4.23}$$

is responsible for all other terms. These other terms include terms nonlinear in v, inhomogeneous terms, and linear terms. Generally, F cannot be zero because (4.16)

is not an exact solution of (4.19) for nonzero a. Notice that up to now we have not made any approximations, so Eqs. (4.20)–(4.23) are equivalent to Eq. (4.19).

The advantage of the definition (4.20) is that the operator:

$$\hat{\mathcal{L}}_a = -\frac{1}{y^3}\partial_y y^3 \partial_y + V(y)$$

has the form of the radially symmetric Schrödinger operator in spatial dimension four $(D = 4)$ with the potential

$$V(y) = -\frac{8}{(1+y^2)^2} + \left[\frac{a^2}{4}y^2 - 2a + \frac{2a}{1+y^2}\right]. \tag{4.24}$$

It means that $\hat{\mathcal{L}}_a$ is the self-adjoint operator with the scalar product

$$\langle \psi, \phi \rangle = \int_0^\infty \psi(y)\phi(y)\, y^3\, dy. \tag{4.25}$$

The potential $V(y) \to \infty$ for $y \to \infty$, which ensures that $\hat{\mathcal{L}}_a$ has only discrete spectrum. This allows us to expand arbitrary v in a discrete set of eigenfunctions of $\hat{\mathcal{L}}_a$:

$$v = c_1\psi_1 + c_2\psi_2 + c_3\psi_3 + \ldots, \tag{4.26}$$

where $c_1(\tau)$, $c_2(\tau)$, ... are $\tau-$dependent coefficients of the expansion (below we often omit argument τ for brevity), $\psi_j(y)$ are the eigenfunctions of $\hat{\mathcal{L}}_a$,

$$\hat{\mathcal{L}}_a\psi_j = \lambda_j\psi_j, \tag{4.27}$$

and λ_j are the respective eigenvalues. The eigenvalues are ordered starting from the lowest eigenvalue as $\lambda_1 < \lambda_2 < \ldots$. All eigenvalues are real and non-degenerate as discussed in the next section.

Note that the use of the scalar product (4.25) (which corresponds to the radially symmetric Schrödinger operator in $D = 4$) is simply an auxiliary mathematical trick, which is effective because the operator $\hat{\mathcal{L}}_a$ is self-adjoint with this scalar product. We remind that all solutions obtained below correspond to RKSE (4.1) with $D = 2$.

4.2.1   Spectrum of linearization operator

The eigenvalues (4.27) of the linearization operator $\hat{\mathcal{L}}_a$ are given by the following implicit expression,

$$\frac{\lambda + 2a}{2a} \left[\ln \frac{1}{a} - \Psi \left(-\frac{\lambda}{2a} \right) + K \right] = 1 + \mathrm{O} \left(a^{1/2} \ln \frac{1}{a} \right), \tag{4.28}$$

as it was proven in Ref. [44] using a rigorous version of the method of matched asymptotics. Here $K := \ln 2 - 1 - 2\gamma$, while Ψ is the digamma function, defined as $\Psi(s) = \frac{d}{ds} \ln \Gamma(s)$, where $\Gamma(s)$ is the gamma function.

Solving (4.28) for λ gives the spectrum of $\hat{\mathcal{L}}_a$, starting from the lowest eigenvalues, as follows

$$\frac{\lambda_1}{a} = -2 + \frac{2}{\ln \frac{1}{a}} - \frac{2(K+\gamma)}{(\ln \frac{1}{a})^2} + \left[2(K+\gamma)^2 - \frac{\pi^2}{3} \right] \frac{1}{(\ln \frac{1}{a})^3} + \mathrm{O} \left(\frac{a}{(\ln \frac{1}{a})^4} \right)$$

$$\frac{\lambda_2}{a} = \frac{2}{\ln \frac{1}{a}} - \frac{K+3-\ln 2}{(\ln \frac{1}{a})^2} + \left[2(K+\gamma)^2 - \frac{\pi^2}{3} - 4 \right] \frac{1}{(\ln \frac{1}{a})^3} + \mathrm{O} \left(\frac{a}{(\ln \frac{1}{a})^4} \right)$$

$$\frac{\lambda_3}{a} = 2 + \frac{2}{\ln \frac{1}{a}} - \frac{K+2-\ln 2}{(\ln \frac{1}{a})^2} + \left[2 \left(K + \gamma - \frac{3}{2} \right)^2 - \frac{\pi^2}{3} - \frac{5}{2} \right] \frac{1}{(\ln \frac{1}{a})^3}$$

$$+ \mathrm{O} \left(\frac{a}{(\ln \frac{1}{a})^4} \right) \tag{4.29}$$

Eigenfunctions ψ_j can be also approximated from the method of matched asymptotics.

In Section 4.2.2 we need to calculate multiple integrals which involve ψ_j. For this purpose, it is more convenient to use the variational approximation for eigenfunctions

obtained in Ref. [27]:

$$\tilde{\psi}_1 = \frac{8}{1+y^2}e^{-ay^2/4}$$

$$\tilde{\psi}_2 = \tilde{\psi}_1\left(1 + \frac{ay^2}{2} - \frac{ay^2}{2}\ln\left(1+y^2\right)\right) \qquad (4.30)$$

$$\tilde{\psi}_3 = \tilde{\psi}_1\left(1 + ay^2\left[-\frac{\pi^2\ln\frac{1}{a}}{\pi^2-12} + \frac{-12+\pi^2(2+\gamma-\ln 2)}{\pi^2-12}\right]\right.$$
$$\left. + ay^2\ln\left(1+y^2\right)\frac{12}{\pi^2-12} + \frac{a^2y^4}{4}\left[\ln\frac{1}{a} - 3 - \gamma + \ln 2 - \frac{24}{\pi^2-12}\right]\right)$$

where $\tilde{\psi}_j$ means the variational approximation to ψ_j, $j = 1, 2, \ldots$. We estimate the accuracy of the variational approximation by calculating the variational approxima-tion for the three lowest eigenvalues λ_1, λ_2, and λ_3 as $\lambda_j = \frac{\langle\tilde{\psi}_j,\hat{\mathcal{L}}_a\tilde{\psi}_j\rangle}{\langle\tilde{\psi}_j,\tilde{\psi}_j\rangle}$, $j = 1,2,3$. Expansion of the resulting expressions for integrals λ_1, λ_2, and λ_3 in inverse powers of $\ln\frac{1}{a}$ agrees with exact results (4.29) up to order $O\left(\frac{1}{(\ln\frac{1}{a})^2}\right)$ for λ_1, λ_2 and up to order $O\left(\frac{1}{\ln\frac{1}{a}}\right)$ for λ_3. This is the best result we are able to achieve with the variational approximation. This accuracy will be however sufficient to obtain (4.6).

4.2.2 Amplitude equations

Similar to (4.26), we expand v from (4.21) in a set of approximate variational eigen-functions $\tilde{\psi}_j$, $j = 1, 2, \ldots$ as follows,

$$v = \sum_{j=1}^{\infty} c_j\tilde{\psi}_j, \qquad (4.31)$$

where $c_j(\tau)$ are the coefficients of the expansion. In this Section we derive a set of amplitude equations for $c_1(\tau)$, $c_2(\tau)$, ... from (4.31) which provide a solution of Eq. (4.21). We solve the amplitude equations exploiting the fact that, at the leading order in a, the solution of (4.19) is given by (4.16). (We used that fact in the definition of (4.20)). We expand all expressions below in integer powers of the small parameters a and $\frac{1}{\ln\frac{1}{a}}$, keeping the lowest nontrivial order of a and several orders of $\frac{1}{\ln\frac{1}{a}}$.

We assume the approximate orthogonality of the variational functions,

$$\langle \tilde{\psi}_i, \tilde{\psi}_j \rangle = O(a) \|\tilde{\psi}_i\| \|\tilde{\psi}_j\| \quad \text{for} \quad i \neq j, \tag{4.32}$$

where $\|\tilde{\psi}_i\| := \langle \tilde{\psi}_i, \tilde{\psi}_i \rangle^{1/2}$, $i = 1, 2, \ldots$. Then, the scalar multiplication of (4.21) onto $\tilde{\psi}_j$ (with the scalar product (4.25)) results in

$$\langle \tilde{\psi}_j, \partial_\tau v \rangle + \langle \tilde{\psi}_j, \hat{\mathcal{L}}_a v \rangle - \langle \tilde{\psi}_j, F(v) \rangle$$
$$= \|\tilde{\psi}_i\|^2 \partial_\tau c_j + \sum_{i=1}^{\infty} c_i \langle \tilde{\psi}_j, \partial_\tau \tilde{\psi}_i \rangle + \sum_{i=1}^{\infty} c_i \langle \tilde{\psi}_j, \hat{\mathcal{L}}_a \tilde{\psi}_i \rangle - \langle \tilde{\psi}_j, F(v) \rangle = 0. \tag{4.33}$$

Here, we neglect corrections from nonexact orthogonality (4.32) because, as we show later, these corrections are of the next order in a when compared with other terms in (4.33). In this section, all calculations of scalar products for (4.33) are based on Appendix in Ref. [1] for the variational functions (4.30). For instance, the direct calculation for the variational functions (4.30) gives the following expressions:

$$\|\tilde{\psi}_1\|^2 = -32 \ln a + 32(-1 - \gamma + \ln 2) + O\left(a \ln a\right),$$
$$\|\tilde{\psi}_2\|^2 = 32(\ln a)^2 + 32(1 + 2\gamma - 2\ln 2) \ln a,$$
$$+ \frac{16}{3} \left[\pi^2 + 6(\ln 2 - 1) \ln 2 + 6\gamma(\gamma + 1 - 2\ln 2) \right] + O\left(a \ln a\right),$$
$$\|\tilde{\psi}_3\|^2 = 64(\ln a)^2 + \frac{32\left(-108 - 48\gamma + 13\pi^2 + 4\gamma\pi^2 + 48\ln 2 - 4\pi^2 \ln 2\right)}{(-12 + \pi^2)} \ln a \tag{4.34}$$
$$+ \frac{1}{(-12 + \pi^2)^2} 32 \left[2\gamma^2 \left(-12 + \pi^2\right)^2 + \pi^4[23 + \ln 2(-13 + 2\ln 2)] \right.$$
$$- 24\pi^2[13 + \ln 2(-11 + 2\ln 2)] + 144(-1 + \ln 2)(-7 + 2\ln 2)$$
$$\left. - \gamma\left(-12 + \pi^2\right) \left[108 - 48\ln 2 + \pi^2(-13 + 4\ln 2)\right] \right] + O\left(a(\ln a)^2\right).$$

We assume (based, e.g., on numerical simulations in [25,38] and following Ref. [27]) ▮ that a is the adiabatically slow function of τ: $\partial_\tau a \ll a^2$. As mentioned above, we expand all quantities in the small parameters a and $\frac{1}{\ln \frac{1}{a}}$ (it is also seen in Appedix of Ref. [1] that all integrals involved in (4.33) expand into these parameters) keeping

only a leading order in a and many enough terms in powers of $\frac{1}{\ln\frac{1}{a}}$. Then the adiabatic assumption $\partial_\tau a \ll a^2$ requires $\partial_\tau a = a^2 O\left(\frac{1}{\ln\frac{1}{a}}\right)$. We introduce a normalized function $\tilde{a}_\tau := \frac{\partial_\tau a}{a^2}\frac{1}{\ln\frac{1}{a}} = O(1) + O(a)$. This allows to write $\partial_\tau a$ as an expansion in inverse powers of $\ln\frac{1}{a}$ only:

$$\partial_\tau a = a^2 \frac{1}{\ln\frac{1}{a}} \tilde{a}_\tau, \quad \tilde{a}_\tau = \tilde{a}_\tau^{(0)} + \tilde{a}_\tau^{(1)}\frac{1}{\ln\frac{1}{a}} + \tilde{a}_\tau^{(2)}\frac{1}{\left(\ln\frac{1}{a}\right)^2} + O\left(\frac{1}{(\ln\frac{1}{a})^3}\right), \quad (4.35)$$

where the coefficients $\tilde{a}_\tau^{(0)}$, $\tilde{a}_\tau^{(1)}$ and $\tilde{a}_\tau^{(2)}$ are $O(1)$ and do not depend on τ in the adiabatic approximation. Note that the subscript τ in these coefficients is *not* a partial derivative but rather indication that these are the expansion coefficients for $\tilde{a}_\tau$.

Assume that the expansion coefficients c_1, c_2, c_3, ... in (4.31) are initially $O(1)$. A series expansion of equations (4.33) over small a, using Eq. (4.35) and dividing each jth equation by $\|\tilde{\psi}_j\|^2$, together with (4.34), result at the leading order in the following expressions

$$\partial_\tau c_1 + a - 2ac_1 + O\left(\frac{a}{\ln\frac{1}{a}}\right) = 0,$$

$$\partial_\tau c_2 + O\left(\frac{a}{\ln\frac{1}{a}}\right) = 0,$$

$$\partial_\tau c_3 + 2ac_3 + O\left(\frac{a}{\ln\frac{1}{a}}\right) = 0, \quad (4.36)$$

$$\partial_\tau c_4 + 4ac_4 + O\left(\frac{a}{\ln\frac{1}{a}}\right) = 0.$$

$\dots$

Here, the terms $2a(j-2)c_j$, $j = 1, 2, 3$ originate from eigenvalues for $\tilde{\psi}_j$ (see Eq. (4.29)), while the term a in the first equation comes from the scalar product of $\tilde{\psi}_1$ with the second term in the right-hand side of (4.23). Also the contribution from $\partial_\tau \psi_j = (\partial_\tau a)\partial_a \psi_j$, $j = 1, 2, \dots$ is included into $O(\dots)$ term. It follows from Eqs. (4.36) that the coefficient c_3 initially decays exponentially (because $a > 0$) until it reaches the

adiabatic, quasi-steady state with $c_3 = O\left(\frac{1}{\ln\frac{1}{a}}\right)$. Our conjecture is that the other coefficients, $c_4, c_5, \ldots$, also decay exponentially (they correspond to the larger values λ_j, so that they are assumed to decay as $c_j \propto \exp[-2a(j-2)\tau]$, according to the linear terms in (4.21)). The lack of explicit expressions for $\tilde{\psi}_j$, $j \geq 4$ does not allow us to prove this statement. We conclude that, after an initial transient, the coefficients c_3, $c_4, \ldots$ reach the adiabatic state with their values

$$c_3, c_4, \ldots = O\left(\frac{1}{\ln\frac{1}{a}}\right). \tag{4.37}$$

Below we assume this adiabatic state.

In the first equation of (4.36) we assume that

$$c_1 = \frac{1}{2} + O\left(\frac{1}{\ln\frac{1}{a}}\right) \tag{4.38}$$

to avoid exponential growth of c_1 in τ. (Such artificial exponential growth would result in error in estimating t_c.)

We have now a freedom in selecting c_2, and we choose it so that $v \to 0$ for any y as $a \to 0$. According to (4.30), $\tilde{\psi}_1(y)|_{y=0} = \tilde{\psi}_2(y)|_{y=0} = 8$ so we set

$$c_2 = -\frac{1}{2} + O\left(\frac{1}{\ln\frac{1}{a}}\right). \tag{4.39}$$

In this case, $c_1\tilde{\psi}_1 + c_2\tilde{\psi}_2 = O(a)$ for $y = O(1)$, i.e. v in (4.20) vanishes with $a \to 0$, as we expect from the self-similar solution (4.16).

Equations. (4.37), (4.38), and (4.39) justify the adiabatic approximation, which means that the coefficients c_1, c_2, c_3, $c_4, \ldots$ depend on τ only through a, and one can

expand them in series of inverse powers of $\ln\frac{1}{a}$:

$$
\begin{aligned}
c_1 &= \frac{1}{2} + \sum_{k=1}^{\infty} d_1^{(k)} \frac{1}{(\ln\frac{1}{a})^k} + O(a), \\
c_2 &= -\frac{1}{2} + \sum_{k=1}^{\infty} d_2^{(k)} \frac{1}{(\ln\frac{1}{a})^k} + O(a), \\
c_3 &= \sum_{k=1}^{\infty} d_3^{(k)} \frac{1}{(\ln\frac{1}{a})^k} + O(a),
\end{aligned}
\tag{4.40}
$$

$$\ldots$$

where the expansion coefficients $d_i^{(j)} = O(1)$ for any i, j; the coefficients do not explicitly depend on τ in the adiabatic approximation.

It follows from (4.40) and (4.35) that

$$
\partial_\tau c_j = O\left(\partial_\tau \frac{1}{\ln\frac{1}{a}}\right) = O\left(\frac{a}{(\ln\frac{1}{a})^3}\right), \quad j = 1, 2, 3, \ldots
\tag{4.41}
$$

Similar to derivation of Eqs. (4.36), we now perform a series expansion of equations (4.33) into small a (but in contrast to the derivation of Eqs. (4.36) we proceed to the higher orders of expansion) using Eqs. (4.34),(4.35),(4.40) to obtain following

equations:

$$\partial_\tau c_1 + \frac{a}{\ln\frac{1}{a}}\left[\frac{\tilde{a}_\tau^{(0)}}{2} - 2d_1^{(1)}\right]$$

$$+\frac{a}{(\ln\frac{1}{a})^2}\left[\frac{\tilde{a}_\tau^{(1)}}{2} + 2d_1^{(1)} - 2d_1^{(2)} + 2d_2^{(1)} - \tilde{a}_\tau^{(0)}d_2^{(1)} + 2d_3^{(1)}\right]$$

$$+O\left(\frac{a}{(\ln\frac{1}{a})^3}\right) = 0, \qquad (4.42)$$

$$\partial_\tau c_2 + \frac{a}{\ln\frac{1}{a}}\left[-1 - \frac{\tilde{a}_\tau^{(0)}}{2}\right]$$

$$+\frac{a}{(\ln\frac{1}{a})^2}\left[-1 - \frac{\tilde{a}_\tau^{(1)}}{2} + 2d_2^{(1)} + \tilde{a}_\tau^{(0)}(d_2^{(1)} - 2d_3^{(1)}) - \gamma + \ln 2)\right]$$

$$+\frac{a}{(\ln\frac{1}{a})^3}\left[-1 - \frac{\tilde{a}_\tau^{(2)}}{2} + 2d_1^{(1)} + (2 + \tilde{a}_\tau^{(0)})d_2^{(2)} + 6d_3^{(1)} + 4\tilde{a}_\tau^{(0)}d_3^{(1)} - 2\tilde{a}_\tau^{(1)}d_3^{(1)}\right.$$

$$-2\tilde{a}_\tau^{(0)}d_3^{(2)} + \frac{\pi^2}{6} + \frac{24\tilde{a}_\tau^{(0)}d_3^{(1)}}{-12+\pi^2} - (\ln 2)^2 + d_2^{(1)}(4 + \tilde{a}_\tau^{(1)} + 2\gamma - 2\ln 2)$$

$$\left.+2\ln 2 + \gamma(-2 - \gamma + 2\ln 2)\right] + O\left(\frac{a}{(\ln\frac{1}{a})^4}\right) = 0, \qquad (4.43)$$

$$\partial_\tau c_3 + \frac{a}{\ln\frac{1}{a}}\left[2d_3^{(1)}\right] + \frac{a}{(\ln\frac{1}{a})^2}\left[-1 + 2(1 + \tilde{a}_\tau^{(0)})d_3^{(1)} + 2d_3^{(2)}\right]$$

$$+O\left(\frac{a}{(\ln\frac{1}{a})^3}\right) = 0. \qquad (4.44)$$

Here we have neglected the expansion coefficients c_j for $j > 3$ by setting $c_4 = c_5 = c_6 = \ldots = 0$. In Equations (4.42)-(4.44) we keep the necessary number of orders in $\frac{1}{\ln\frac{1}{a}}$ to obtain the closed expressions for the expansion terms in (4.35). Equations (4.42)-(4.44) can be viewed as the compatibility conditions which ensure that expansions (4.40) and (4.35) are correct, so that a is indeed the adiabatically slow variable.

It follows immediately from Eq. (4.44) in the order $\frac{a}{\ln\frac{1}{a}}$ that

$$d_3^{(1)} = 0, \qquad (4.45)$$

and from Eq. (4.43) in the order $\frac{a}{\ln\frac{1}{a}}$ that

$$\tilde{a}_\tau^{(0)} = -2. \qquad (4.46)$$

Then, from Eq. (4.42) in the order $\frac{a}{\ln \frac{1}{a}}$ we obtain

$$d_1^{(1)} = -\frac{1}{2}. \tag{4.47}$$

Using Eqs. (4.43) and (4.45)-(4.47) we obtain in the order $\frac{a}{(\ln \frac{1}{a})^2}$ that

$$\tilde{a}_\tau^{(1)} = -2 - 2\gamma + 2\ln 2. \tag{4.48}$$

Using Eqs. (4.42) and (4.45)-(4.48) we obtain in the order $\frac{a}{(\ln \frac{1}{a})^2}$ that

$$d_1^{(2)} = \frac{1}{2}(-2 + 4d_2^{(1)} - \gamma + \ln 2). \tag{4.49}$$

Similar, using Eqs. (4.44) and (4.45)-(4.48) we obtain in the order $\frac{a}{(\ln \frac{1}{a})^2}$ that

$$d_3^{(2)} = \frac{1}{2}. \tag{4.50}$$

Equation (4.43) in order $\frac{a}{(\ln \frac{1}{a})^3}$ requires also to take into account $\partial_\tau c_2$ which is given by

$$\partial_\tau c_2 = -\frac{1}{2}\frac{a}{(\ln \frac{1}{a})^3} + O\left(\frac{a}{(\ln \frac{1}{a})^4}\right), \tag{4.51}$$

according to (4.41) and (4.40).

Using Eq. (4.43) in order $\frac{a}{(\ln \frac{1}{a})^3}$ and (4.45)-(4.48), (4.50), (4.51) we obtain the closed expression

$$\tilde{a}_\tau^{(2)} = \frac{\pi^2}{3} - 2(\ln 2)^2 + 4\ln 2 + \gamma(-4 - 2\gamma + 4\ln 2). \tag{4.52}$$

Here, the unknown coefficient $d_2^{(1)}$ has been cancelled out identically.

Equations (4.35), (4.46), (4.48), and (4.52) result in closed ODE (4.6) for a, which is the first main result of this paper.

Figure 4.4 shows $\partial_\tau a$ as a function of a for RKSE simulations with different initial conditions (the same initial conditions as in Figure 4.1). Notice that after an initial transient all curves collapse to the single curve given by Eq. (4.6). This suggests that we can use the proximity of numerical curves to the analytical curve as the criterion for selecting t_0 in equation (4.9). In Figure 4.1, we used the values of t_0 defined for each initial condition as the time $t = t_0$ when the relative difference between numerical and analytical curves reduces down to 20%. Arrows in Figure 4.4 point to locations $(a(t_0), \partial_\tau a(t_0))$ satisfying this criterion. For the simulations of Figure 4.1 we obtained $t_0 = 7.2125\ldots$, $t_0 = 4.5879\ldots$, $t_0 = 3.3257\ldots$, $t_0 = 2.5528\ldots$ for $N/N_c = 1.0250, 1.0375, 1.0500, 1.0625$, respectively. Also in these cases $t_c = 8.12305\ldots$, $t_c = 5.32533\ldots$, $t_c = 3.94247\ldots$, $t_c = 3.12039\ldots$, respectively.

The dashed-dotted curves in Figure 4.1 are only weakly sensitive to the choice of $t_0 < t_c$, provided t_0 is chosen later than the time specified by the 20%-difference criterion. For instance, if we choose t_0 based on 10%-difference criterion (instead of 20%), the $L(t)$ curves in Figure 4.1 would change by $< 5\%$ which is within the relative error of these curves in comparison with the numerics (solid curves in Figure 4.1).

4.2.3 Blow-up rate of self-similar solution

In this section we solve ODE (4.6) together with (4.7) and (4.8) to derive the blow-up rate (4.2). Integration of Eq. (4.6) from an initial value τ_0 to τ gives

$$\frac{1}{a}\left[\ln\frac{1}{a} + \tilde{M} + \frac{b}{\ln\frac{1}{a}} + O\left(\frac{1}{(\ln\frac{1}{a})^2}\right)\right]\Bigg|_{\tau=\tau_0}^{\tau} = 2(\tau - \tau_0),\qquad(4.53)$$

where $\tilde{M} = \frac{M}{2} - 1 = -2 - \gamma + \ln 2$ and $b = \frac{b_0}{2} + \frac{M^2}{4} = 1 + \frac{\pi^2}{6}$ as in (4.9). If we look at Eq. (4.53) as the implicit expression to determine $a(\tau)$ then it turns into a remote relative of the Lambert W-function. Such implicit expression can be solved for a assuming $\tau \gg 1$ by iterations as follows:

$$
\ln \frac{1}{a} = L_1 - L_2 + \frac{L_2}{L_1} + \frac{L_2^2}{2L_1^2} - \frac{L_2}{L_1^2} \frac{\tilde{M}}{L_1} + \frac{-2b + 2\tilde{M} + \tilde{M}^2 - 2\tilde{M}L_2}{2L_1^2}
$$
$$
+ O\left(\frac{L_2^3}{L_1^3}\right),
$$
(4.54)

where $L_1 := \ln\left[2(\tau - \tau^*)\right]$, $L_2 := \ln\ln\left[2(\tau - \tau^*)\right]$, and

$$
\tau^* = \tau_0 - \frac{1}{2a}\left(\ln\frac{1}{a} + \tilde{M} + \frac{b}{\ln\frac{1}{a}}\right)\bigg|_{a=a_0}, \qquad a_0 = a(\tau_0).
$$
(4.55)

At this point, one can proceed in qualitatively similar way to Ref. [27] to determine $L(\tau)$. However that way of calculation results in a slow convergence of the asymptotic series for $L(\tau)$ with the increase of τ. We choose a different path. Our goal is to start with Eq. (4.53), to carry as many steps of exact transformations as possible, and to perform asymptotic expansions as late as possible. Here and below we abuse notation and use the same notations for all functions with the same physical meaning, independently of their arguments: $L = L(t) = L(\tau) = L(a)$, $\tau = \tau(t) = \tau(L) = \tau(a)$ and $a = a(t) = a(\tau) = a(L)$. Similar, for initial values $L_0 = L(t_0) = L(\tau_0) = L(a_0)$, $\tau_0 = \tau(t_0) = \tau(L_0) = \tau(a_0)$ and $a_0 = a(t_0) = a(\tau_0) = a(L_0)$.

We use Eqs. (4.7) and (4.8) to express a through τ-derivative of L as follows

$$
a = -\frac{\partial_\tau L}{L}.
$$
(4.56)

We integrate (4.56) in τ between τ_0 and τ, using the integration by parts, to obtain

$$
-\ln\frac{L}{L_0} = \int_{\tau_0}^{\tau} a(\tau)\,d\tau = a\tau(a) - a_0\tau(a_0) - \int_{a_0}^{a} \tau\,da
$$
$$
= \left[\tau - \tau^*\right]a - \left[\tau_0 - \tau^*\right]a_0 - \int_{a_0}^{a}\left(\tau - \tau^*\right)da.
$$
(4.57)

To evaluate integral over a in (4.57) explicitly we use $\tau(a)$ from (4.53) with (4.55) and obtain

$$-\ln\frac{L}{L_0} = \frac{1}{4}\left[\left(\ln\frac{1}{a}\right)^2 - \left(\ln\frac{1}{a_0}\right)^2\right] + \frac{\tilde{M}+1}{2}\left(\ln\frac{1}{a} - \ln\frac{1}{a_0}\right)$$

$$+\frac{b}{2}\left(\ln\ln\frac{1}{a} - \ln\ln\frac{1}{a_0}\right) + \frac{b}{2}\left(\frac{1}{\ln\frac{1}{a}} - \frac{1}{\ln\frac{1}{a_0}}\right) + O\left(\frac{1}{\ln\frac{1}{a}}\right). \tag{4.58}$$

Note also that the term $O\left(\frac{1}{\ln\frac{1}{a}}\right)$ in (4.58) originates from the next order term $O\left(\frac{1}{(\ln\frac{1}{a})^2}\right)$ in Eq. (4.53). Formally, in Eq. (4.58), the terms $O\left(\frac{1}{\ln\frac{1}{a}}\right)$ and $\frac{b}{2\ln\frac{1}{a}}$ are of the same order. Yet, our numerical simulations indicate that $\frac{b}{2\ln\frac{1}{a}}$ term improves accuracy of the analytic approximation, so we keep this term in its explicit form.

We introduce new variables,

$$l := \ln\frac{1}{L} \quad \text{and} \quad l_0 := \ln\frac{1}{L_0}, \tag{4.59}$$

as well as define

$$l^* = l_0 - \frac{1}{4}\left(\ln\frac{1}{a_0}\right)^2 - \frac{\tilde{M}+1}{2}\ln\frac{1}{a_0} - \frac{b}{2}\left(\ln\ln\frac{1}{a_0} + \frac{1}{\ln\frac{1}{a_0}}\right), \tag{4.60}$$

which allows to rewrite (4.58) as follows:

$$l - l^* = \frac{1}{4}\left(\ln\frac{1}{a}\right)^2 + \frac{\tilde{M}+1}{2}\ln\frac{1}{a} + \frac{b}{2}\left(\ln\ln\frac{1}{a} + \frac{1}{\ln\frac{1}{a}}\right) + O\left(\frac{1}{\ln\frac{1}{a}}\right). \tag{4.61}$$

We now solve Eq. (4.61) for $\ln\frac{1}{a}$. Instead of doing straightforward iterations, we neglect the terms $\frac{b}{2}(\ldots)$, $O\left(\frac{1}{\ln\frac{1}{a}}\right)$ in Eq. (4.61) and solve the remaining part of the equation, $Y_0^2 - 2Y_0 - V = 0$, exactly:

$$Y_0 = 1 + \sqrt{1+V}, \tag{4.62}$$

where we define

$$Y := -\frac{\ln\frac{1}{a}}{\tilde{M}+1} \quad \text{and} \quad V := \frac{4}{(\tilde{M}+1)^2}(l - l^*) \tag{4.63}$$

with Y_0 being the leading order approximation to Y, such that

$$Y = Y_0 + \delta Y. \tag{4.64}$$

To find δY as a function of V, we represent δY through the formal series $\delta Y = \sum_{n=1}^{\infty} \frac{\delta Y_{-n}}{Y_0^n}$ (with Y_0 given by (4.62)). We use this series together with (4.62)-(4.64) to perform a series expansion of Eq. (4.61) in inverse powers of Y_0. It allows to determine the coefficients δY_n recursively at integer inverse powers of Y_0 starting with the power zero. In particular, the zero power gives $Y_{-1} = -\frac{b \ln\left[-(1+\tilde{M})Y_0\right]}{(1+\tilde{M})^2}$. Note that the double logarithm $\ln \ln \frac{1}{a}$ in (4.61) also needs to be expanded. All together it results in

$$\delta Y = -\frac{b \ln\left[-(1+\tilde{M})Y_0\right]}{(1+\tilde{M})^2 Y_0} + \frac{-b(1+\tilde{M})\ln\left[-(1+\tilde{M})Y_0\right] + b}{(1+\tilde{M})^3 Y_0^2} +$$
$$+ O\left(\frac{1}{Y_0^2}\right) + O\left(\frac{(\ln Y_0)^2}{Y_0^3}\right). \tag{4.65}$$

Here, similar to (4.58), we keep the term $\frac{b}{(1+\tilde{M})^3 Y_0^2}$, even though this term is of the same order as $O\left(\frac{1}{Y_0^2}\right)$ term. Here, $\tilde{M} + 1 = -0.884068\ldots$ according to (4.9). Note, that instead of performing an expansion in inverse powers of Y_0, one can simply do it in inverse powers of $V^{1/2}$. This, however, would result in a slower convergence for moderate $(V \gtrsim 1)$ values of V.

We rewrite (4.7) as $-\frac{L\,dL}{a} = dt$, and integrate it between time t_c and t:

$$\int_t^{t_c} dt' = t_c - t = -\int_L^0 \frac{L'}{a(L')}dL', \tag{4.66}$$

where following (4.59) and (4.63) we can represent L through V as $L = \exp\left(-\left[l^* + \frac{(\tilde{M}+1)^2}{4}V\right]\right)$. The dependence $a(L)$ in (4.66) follows from (4.59)-(4.65). Switching from integration

over L to the integration over Y_0 in (4.66) we obtain:

$$
t_c - t = \int\limits_{Y_0}^{\infty} \exp\left(-2\left[l^* + \frac{(\tilde{M}+1)^2}{4}[(Y_0'-1)^2 - 1]\right]\right) \frac{(\tilde{M}+1)^2}{2}(Y_0'-1)
$$

$$
\times \exp\left(-(1+\tilde{M})Y_0' + \frac{b\ln\left[-(1+\tilde{M})Y_0'\right]}{(1+\tilde{M})Y_0'}\right.
$$

$$
\left. - \frac{-b(1+\tilde{M})\ln\left[-(1+\tilde{M})Y_0'\right]+b}{(1+\tilde{M})^2 Y_0'^2} + O\left(\frac{1}{Y_0'^2}\right)\right) dY_0'. \tag{4.67}
$$

Here, the integration cannot be carried explicitly. Instead, we use the Laplace method (see e.g. [97, 98]) to evaluate the integral asymptotically in the limit $Y_0 \gg 1$. We introduce in Eq. (4.9) a new integration variable,

$$
z := Y_0' - Y_0, \tag{4.68}
$$

and rewrite Eq. (4.67) as

$$
t_c - t = \frac{(\tilde{M}+1)^2}{2} \exp\left[-2l^* - \frac{(\tilde{M}+1)^2}{2}Y_0^2 + (\tilde{M}+1)\tilde{M}Y_0\right] \int\limits_0^{\infty} e^{Y_0 S(z,Y_0)} dz, \tag{4.69}
$$

where

$$
S(Y_0, z) = -(\tilde{M}+1)^2 z + \frac{1}{Y_0}\left[-\frac{(\tilde{M}+1)^2}{2}z^2 + (\tilde{M}+1)\tilde{M}z + \ln(Y_0 + z - 1)\right]
$$

$$
+ \frac{b\ln\left[-(1+\tilde{M})(Y_0+z)\right]}{Y_0(1+\tilde{M})(Y_0+z)} - \frac{-b(1+\tilde{M})\ln\left[-(1+\tilde{M})(Y_0+z)\right]+b}{Y_0(1+\tilde{M})^2(Y_0+z)^2}
$$

$$
+ O\left(\frac{1}{Y_0(Y_0+z)^2}\right). \tag{4.70}
$$

To use the Laplace method for asymptotic expansion of the integral in (4.69), we start with the following general expression, [97, 98]:

$$
\int\limits_0^{\infty} e^{Y_0 S(z,Y_0)} dz = e^{Y_0 S(0,Y_0)} \sum_{n=0}^{\infty} c_n Y_0^{-n-1} \tag{4.71}
$$

with

$$c_n = (-1)^{n+1} \left(\frac{1}{S'(z, Y_0)} \frac{\partial}{\partial z} \right)^n \left(\frac{1}{S'(z, Y_0)} \right) \Bigg|_{z=0}, \quad S'(z, Y_0) := \frac{\partial}{\partial z} S(z, Y_0). \quad (4.72)$$

Taking into account two leading terms in (4.71), we obtain from (4.69), (4.70), (4.71), and (4.72) the following expression:

$$t_c - t = \frac{(\tilde{M}+1)^2}{2} \exp\left[-2l^* - \frac{(\tilde{M}+1)^2}{2} Y_0^2 + (\tilde{M}+1)\tilde{M}Y_0 + \ln(Y_0 - 1) \right]$$

$$\times \exp\left[\frac{b \ln\left[-(1+\tilde{M})Y_0 \right]}{(1+\tilde{M})Y_0} - \frac{-b(1+\tilde{M}) \ln\left[-(1+\tilde{M})Y_0 \right] + b}{(1+\tilde{M})^2 Y_0^2} + O\left(\frac{1}{Y_0^2} \right) \right]$$

$$\times \frac{1}{(\tilde{M}+1)^2 Y_0} \left[1 + \frac{\tilde{M}}{(1+\tilde{M})Y_0} + \frac{\tilde{M}^2}{(1+\tilde{M})^2 Y_0^2} + O\left(\frac{\ln Y_0}{Y_0^3} \right) \right]. \quad (4.73)$$

We now define a large parameter

$$x := \sqrt{-2\ln \beta(t_c - t)} - \tilde{M}, \quad (4.74)$$

where

$$\beta := 2 \exp\left\{ 2l^* - \frac{\tilde{M}^2}{2} \right\}. \quad (4.75)$$

We multiply both the lhs and the rhs of (4.73) by β from (4.75) and take logarithm from both sides to obtain $-\frac{x^2}{2}$ on the lhs. We solve the resulting equation for Y_0 by assuming the asymptotic form,

$$Y_0 = b_{-1}x + \sum_{n=0}^{\infty} \frac{b_n}{x^n}. \quad (4.76)$$

and performing a series expansion of both rhs and lhs of that resulting equation in inverse powers of x. The coefficients $b_{-1}, \, b_1, \ldots, \, b_3$ are determined recursively giving

$$Y_0 = -\frac{1}{\tilde{M}+1} \left[x + \frac{1 - b\ln x}{x^2} + \frac{-\frac{1}{2} - 2\tilde{M} + b(\ln x + 2\tilde{M}\ln x - 1)}{x^3} \right]$$

$$+ O\left(\frac{1}{x^3} \right) + O\left(\frac{(\ln x)^2}{x^4} \right). \quad (4.77)$$

Note that the choice of the factor $\exp\left\{-\frac{\tilde{M}^2}{2}\right\}$ in (4.75) is somewhat arbitrary (the lhs and the rhs of (4.73) can be multiplied by an arbitrary positive constant). The factor $\exp\left\{-\frac{\tilde{M}^2}{2}\right\}$ is chosen to speed up convergence of (4.77) for $Y_0 \gtrsim 1$, i.e. for $L(t) \lesssim 1$.

Using (4.59), (4.62), and (4.63) we obtain

$$L(t) = \exp\left[-l^* - \frac{(\tilde{M}+1)^2}{4}(Y_0^2 - 2Y_0)\right]. \tag{4.78}$$

Equations (4.59), (4.60) (4.74), (4.75), (4.77), and (4.78) give the closed expression for $L(t)$ as a function of $t_c - t$ and the initial values $L_0 = L(t_0)$, $a_0 = -LL_t|_{t=t_0}$. To make the comparison with the old scaling (4.5) more transparent, we plug the expression for Y_0 from (4.77) into (4.78) and perform a series expansion of the expression in the exponent into inverse powers of x, obtaining the final expression (4.9). Note that the first term in the exponent of the first equation in (4.9) can be rewritten through x as $-\sqrt{-\frac{\ln\beta(t_c-t)}{2}} = -\frac{x+\tilde{M}}{2}$. Thus, Eq. (4.9) includes terms of orders x and x^0.

The error terms $O\left(\frac{1}{x^3}\right)$ in (4.77) and $O\left(\frac{1}{x^2}\right)$ in (4.9) result from the error term $O\left(\frac{1}{(\ln\frac{1}{a})^4}\right)$ in Eq. (4.6). We, however, chose to write down explicitly the terms of the same orders, $\propto \frac{1}{x^3}$ in (4.77) and $\propto \frac{1}{x^2}$ in (4.9). These terms are independent from the error term $O\left(\frac{1}{(\ln\frac{1}{a})^4}\right)$ of Eq. (4.6). Next order error terms are $O\left(\frac{(\ln x)^2}{x^4}\right)$ in (4.77) and $O\left(\frac{(\ln x)^2}{x^3}\right)$ in (4.9).

4.3   Simulations of RKSE

In our numerical simulation we evolve Eq. (4.14), written in terms of the mass of bacteria $m(r,t)$ within the circle of radius r as defined in (4.13). The density, $\rho(r,t) = \frac{1}{r}\frac{\partial m}{\partial r}$, and other quantities characterizing the evolution of the collapse are computed

from the mass. To find the width of the collapse, we assume that the solution has reached its self-similar form given by Eq. (4.12). Then, the collapse width can be estimated from the density at the center as $L = (\frac{1}{8}\rho|_{r=0})^{-1/2}$. To compute the slow parameter, a, we differentiate $L(t)$, as in (4.7). The self-similar time, τ, is found by integrating $L(t)$ according to Eq. (4.8).

4.3.1 Simulation Challenges

A typical solution for $m(r, t)$ is shown in Figure 4.3b. The spatial extent of the collapse is marked by a large increase in the gradient of the solution $m(r, t)$ near the center, which becomes even larger and moves even closer to the center as time progresses. This requires special treatment to ensure that the solution remains well-resolved.

The results presented in this work are obtained using an adaptive mesh refinement (AMR) technique [3,63], complemented with the sixth-order Runge-Kutta time advancement method. Our spatial domain, $r \in [0, r_{max}]$, is divided into several subdomains (subgrids) with different spatial resolution. The spacing between computational points is constant for each subgrid, and differs by a factor of two between adjacent subgrids. The rightmost subgrid, farthest from the collapse, has the coarsest resolution; the spatial step decreases in the inward direction. The simulations of modified Keller-Segel equation and NLSE were performed with common code and only the computation of right hand side differ.

4.3.2 Numerical Method

The grid structure adapts during the evolution of the collapse to keep the solution well resolved. When a refinement condition is met, the leftmost subgrid is divided

in two equal subgrids. Then, the new leftmost subgrid is refined; that is, additional computational points are placed halfway between the existing points. The values at the new points are obtained with tenth-order interpolation. The condition for grid refinement comes naturally from properties of the self-similar profile. The density at the origin increases by a factor of 4 as the width of profile decreases by a factor of 2 according to Eq. (4.2). To keep the effective number of grid points per L within desired limits, we use the increase of the maximum density by factor of 4 as the condition for refinement.

In the interior of each subgrid, the spatial derivatives are computed using eigth-order central differences on a nine point stencil. At the subgrid boundaries, the data are copied between subgrids to fill in values at "ghost points", as shown by arrows in Figure 4.5. Notice that communication between subgrids is going in both directions: in AMR terminology, data from the fine subgrid is restricted to the coarse grid ghost points, and data from the coarse grid is prolongated to the fine grid ghost points. The data between points of the coarser subgrids needed for finer subgrid ghost points are obtained by tenth order interpolation. The left ghost points of the leftmost subgrid are filled using reflective boundary conditions. The point $r = 0$ is treated in a special way because of the singularity in the rhs of Eq. (4.14). Expanding $m(r,t)$ in a power series in r at the origin and using the definition (4.13) we obtain that $m(r,t) = \frac{\rho(0,t)r^2}{2} + O(r^4)$. This is also consistent with the series expansion in r of rhs of Eq. (4.14). Thus in the spatial discretization we set $m(r = 0, t) = 0$. The right ghost points of the rightmost subgrid are filled with the data from the last point. We found the right boundary conditions to be very forgiving, which is not surprising considering that the mass approaches a constant, as r^{-3}, when $r \to \infty$.

The solution on all subgrids is evolved with the same timestep, $\Delta t = C_{CFL}h^2$, where h is the spatial step of the finest grid and C_{CFL} is the constant. We typically used $C_{CFL} = 0.4$ but also tested convergence in time with various values of C_{CFL}.

We use two kinds of initial conditions. First kind is the Gaussian,

$$m|_{t=0} = A\left(1 - e^{-(r/\sigma)^2}\right),$$

which implies

$$\rho|_{t=0} = \frac{2A}{\sigma^2} e^{-(r/\sigma)^2},$$

where σ and A are the parameters of the initial condition. Second kind is the modified stationary solution, $m|_{t=0} = Am_0(r)$, where $m_0(r)$ is given by Eq. (4.15). Both types of initial data result in similar dynamics for the same values of $N = 2\pi A$. The simulations presented in this paper were performed for Gaussian initial conditions, with $\sigma = 1$ and $A = 4.1$, 4.15, 4.2, and 4.25. The initial grid was comprised of ten subgrids; the finest subgrid had 400 points while all other subgrids had 200 points each. The size of domain was set to $r_{max} = 1600L_0$.

We have verified the AMR code against an independently developed, uniform grid code with an adaptive spatial resolution and an adaptive time step. Similar to the AMR code, the uniform-grid code evolved Eq. (4.14) using fourth order Runger-Kutta integration in time. The spatial derivatives were computed spectrally using the `FFTW-3` library [99]. Since Fourier transforms require periodic boundary conditions, the spatial domain was extended to $r \in [-r_{max}, r_{max}]$ with sufficiently large r_{max} (about $50L_0$). As in the AMR code, we set the value of the mass to zero at the origin point to avoid the singularity in the rhs of the equation. Although uniform in space, the grid resolution was refined at times when the maximum density increases by a factor of four. The new grid had twice as many points with values computed by spectral interpolation. We run the uniform-grid code at $C_{CFL} = 0.2$.

Although the uniform-grid code was useful for cross-comparison, it was significantly less efficient than the AMR code. Typically, we run the uniform grid code until the peak density reached $\approx 10^5$, which required $32,768$ gridpoints with grid resolution $\frac{L}{8} < h < \frac{L}{4}$. On the other hand, in the AMR simulations presented here, the

density reached $\approx 10^{17}$ on approximately $12,000$ total gridpoints, with $\frac{L}{100} < h < \frac{L}{50}$ resolution on the finest subgrid.

4.4   Conclusion and Discussion

In conclusion, we studied the collapsing solution of the 2D RKSE, Eq. (4.1). To leading order, the collapsing solution has the self-similar form (4.2), characterized by the scaling $L(t)$. Our analysis of the dynamics of perturbations about the self-similar form allowed us to find the time dependence of the width of the collapsing solution given by the scaling (4.9).

We found that both ODE (4.6) for $a(\tau)$ and the scaling (4.9) for $L(t)$ are in excellent agreement with numerical simulations of RKSE. We compared the scaling (4.9) with the previously known scalings (4.3)-(4.5) and showed that scaling (4.4) is the correct asymptotic limit. However, this limit dominates only for unrealistically small values $L \lesssim 10^{-10000}$. In contrast, the scaling (4.9) agrees well with simulations for a quite moderate decrease of $L(t)$ compared to the initial condition. E.g., Figure 4.2 shows that six-fold decrease of L compare with the initial value $L(0)$ is enough to achieve the relative error $\lesssim 7\%$ between simulations and the scaling (4.9).
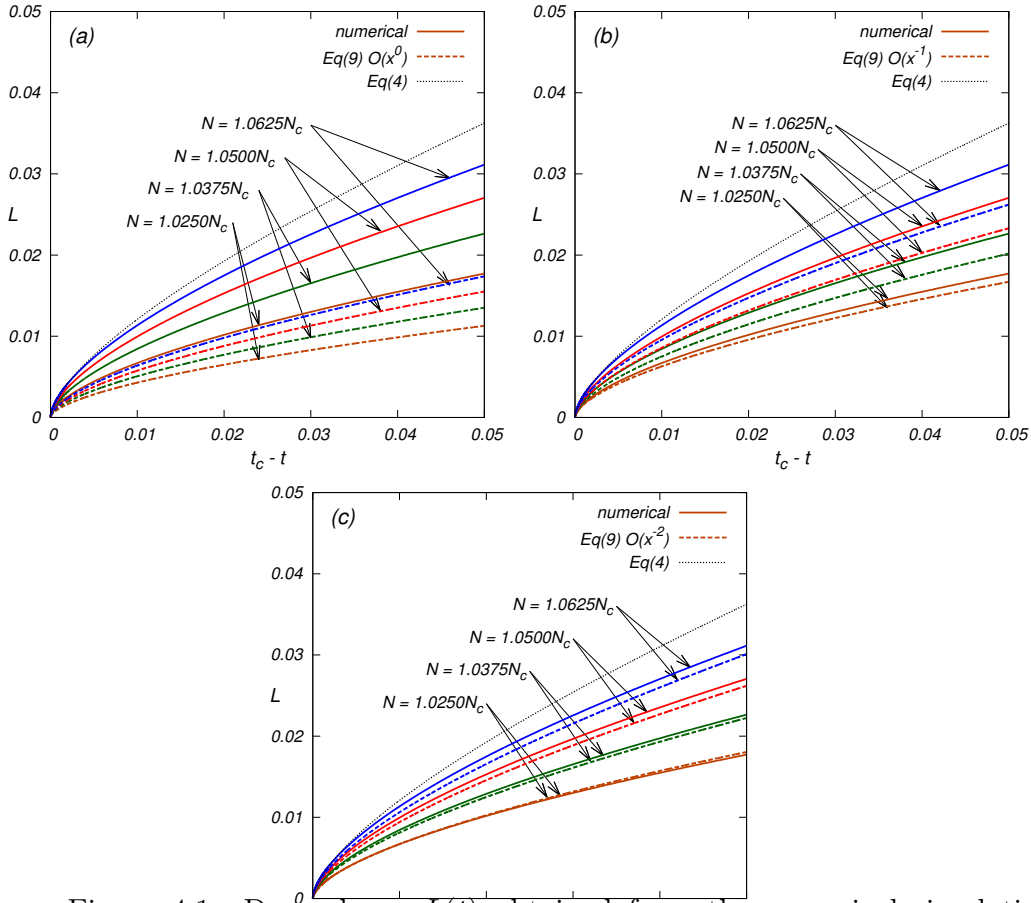
Figure 4.1: Dependence $L(t)$ obtained from the numerical simulations of RKSE (solid lines) is compared to the scaling (4.4) (dotted line) and to the scaling (4.9) (dashed-dotted lines). The lines of different colors correspond to different initial conditions (different values of N). Different panels show the different orders of the scaling in the exponent of the first equation of (4.9): (a) the terms up to $O(x^0)$ are taken into account; (b) the terms up to $O(x^{-1})$ are taken into account; (c) the terms up to $O(x^{-2})$, i.e., all terms except the error term $O(\ldots)$, are taken into account. Convergence of the analytical results to the numerical results with increase of the order in inverse power of x is clearly seen in (a)-(c). The relative difference between numerical and analytical results in (c) is $\lesssim 5\%$ and decreases with the decrease of $(N - N_c)/N_c > 0$. In simulations the initial conditions in the spatial Gaussian form as described in Section 4.3.
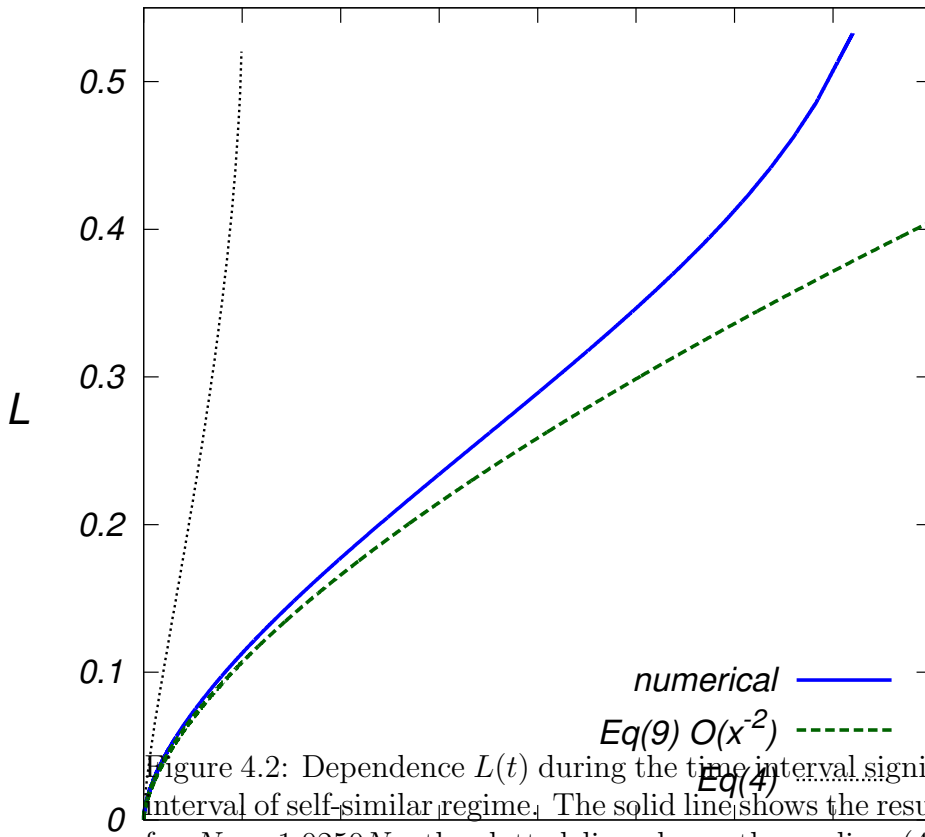
Figure 4.2: Dependence $L(t)$ during the time interval significantly exceeding the time interval of self-similar regime. The solid line shows the result of numerical simulations for $N = 1.0250 N_c$, the dotted line shows the scaling (4.4), while the dashed line shows the scaling (4.9) with all terms up to $O(x^{-2})$. The six-fold decrease of L from the initial value $L(0) = 0.98773$ already gives a good agreement between numerical simulation and (4.9), with relative difference between them $\lesssim 7\%$ for $L < 0.15$. The scaling (4.4) agrees with simulation only in order of magnitude for $L \simeq 0.15$. Figure 4.1c shows the same curves for $N = 1.0250 N_c$ zoomed-in to the origin.
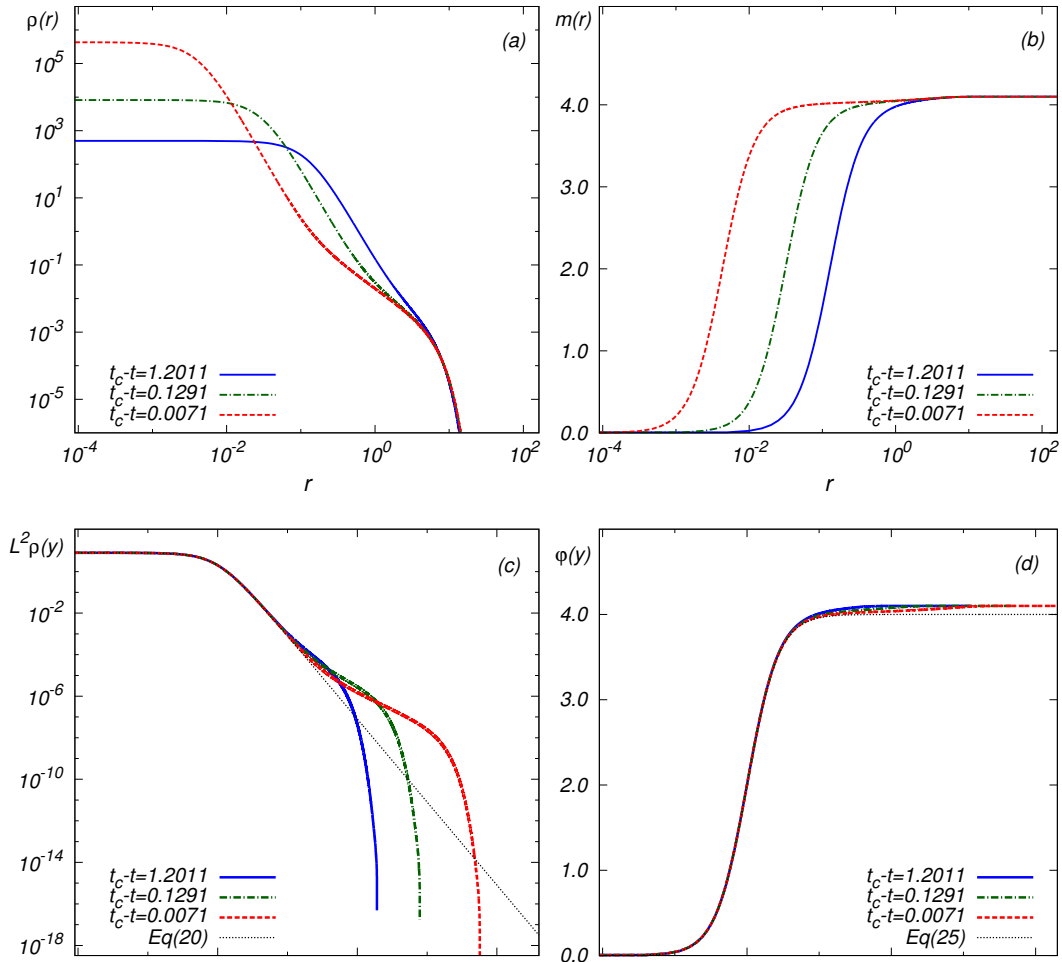
Figure 4.3: The spatial dependence of the density ρ (panels a,c) and the mass m (panels b,d) at different moments of time for the simulation with $N = 1.0250N_c$. In the top row (panels a,b), the data is shown in simulation coordinates. In the bottom row (panels c,d), rescaled density, $L^2\rho(y)$, and mass, $\varphi(y, \tau) \equiv m(r, t)$, are shown as functions of rescaled radius, $y = r/L$. In panel (a), notice the growth of $\rho(r)$ near the origin and a nearly steady tail. In panel (c), notice the convergence to the static solution (4.11),(4.12) in the growing neighborhood of $y = 0$. In loglog scale the deviation from that static solution has the form of a bump. The bump moves away from the origin as $t \to t_c$.
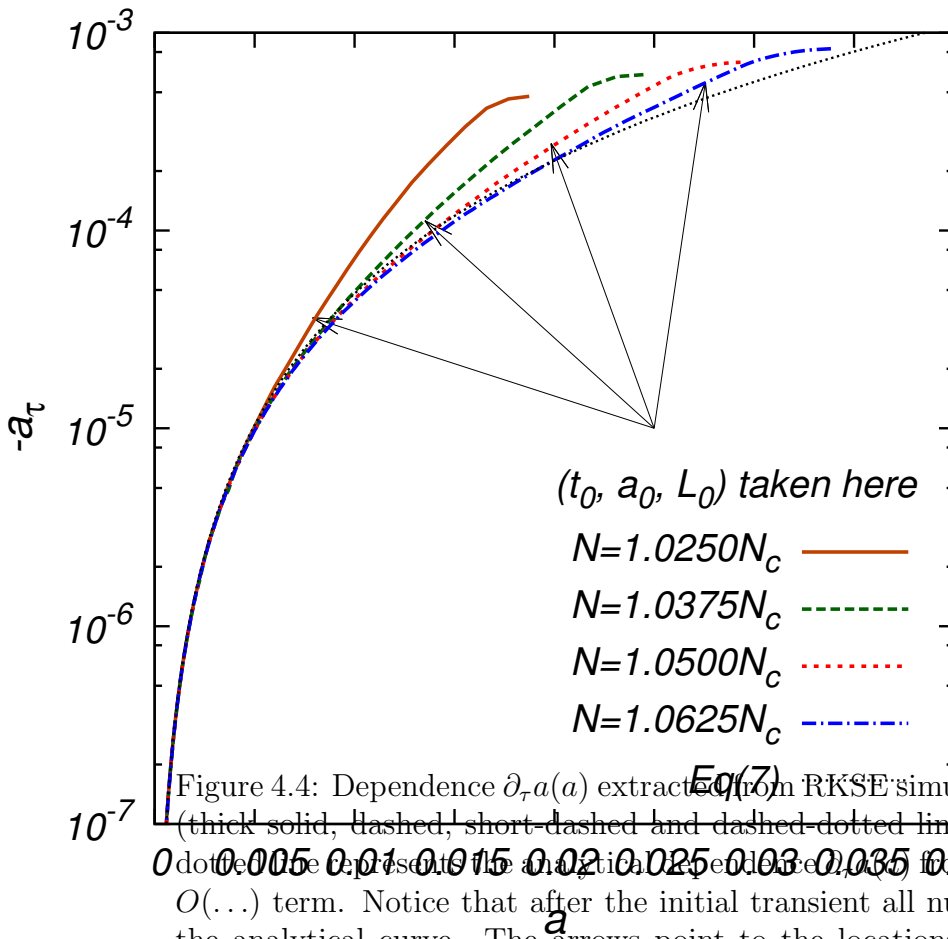
Figure 4.4: Dependence $\partial_\tau a(a)$ extracted from RKSE simulations shown in Figure 4.1 (thick solid, dashed, short-dashed and dashed-dotted lines, respectively). The thin dotted curve represents the analytical expectation $\partial_\tau a(a)$ from Eq. (4.6), with neglected $O(\dots)$ term. Notice that after the initial transient all numerical curves collapse on the analytical curve. The arrows point to the locations where the relative difference between the analytical and numerical curveds reduces to 20%, the criterion for selecting t_0 in Eq. (4.9) and in Figure 4.1.
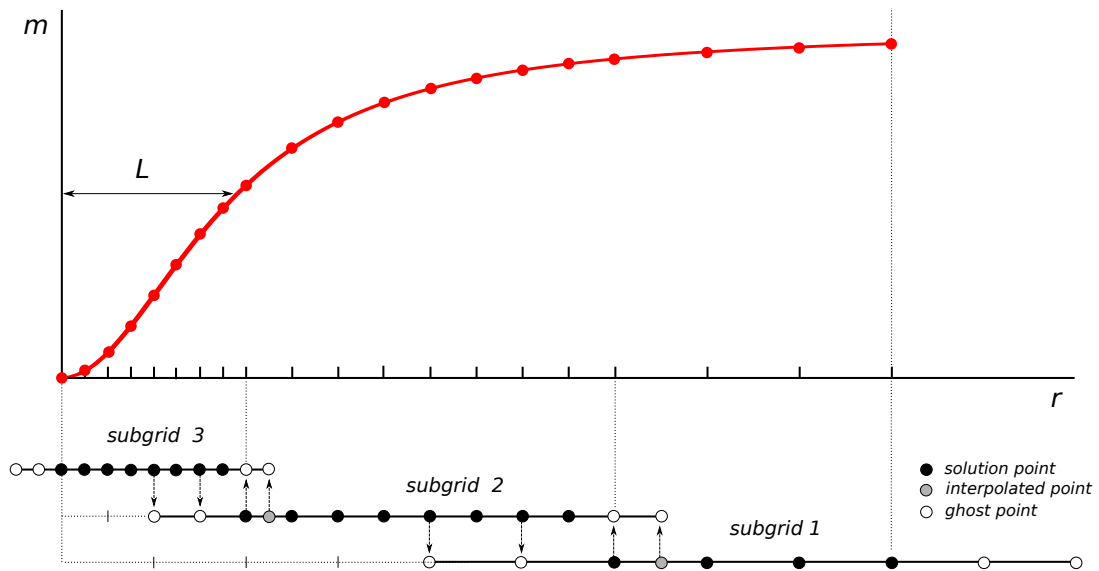
Figure 4.5: Schematic representation of the discretized solution and the grid structure. Three subgrids are shown. The subgrids closer to the center of the collapse have finer resolution. The data at black points are evolved by the discretized Eq. (4.14), the data at white points is copied from neighboring subgrids (the copying is shown by arrows), the data in gray points is interpolated from neighboring points using 6th order polynomial.

References

[1] Sergey A. Dyachenko, Pavel M. Lushnikov, and Natalia Vladimirova. Logarithmic scaling of the collapse in the critical keller-segel equation. *Nonlinearity*, 26:3011–3041, 2013.

[2] S. A. Dyachenko, P. M. Lushnikov, and N. Vladimirova. Logarithmic-type scaling of the collapse of keller-segel equation. *AIP Conf. Proc.*, 1389:709–712, 2011.

[3] C. Sulem and P. L. Sulem. *Nonlinear Schrödinger Equations: Self-Focusing and Wave Collapse*. World Scientific, New York, 1999.

[4] G. Fibich and G. Papanicolaou. Self-focusing in the perturbed and unperturbed nonlinear schrodinger equation in critical dimension. *SIAM J. Appl. Math.*, 60:183, 1999.

[5] Pavel M. Lushnikov, Sergey A. Dyachenko, and Natalia Vladimirova. Beyond leading-order logarithmic scaling in the catastrophic self-focusing of a laser beam in kerr media. *Phys. Rev. A*, 88:013845, Jul 2013.

[6] M. S. Longuet-Higgins and M. J. H. Fox. Theory of the almost-highest wave: the inner solution. *J. Fluid Mech.*, 80(4):721–741, 1977.

[7] L. W. Schwartz and J. D. Fenton. Strongly nonlinear waves. *Ann. Rev. Fluid. Mech*, 14:39–60, 1982.

[8] Sergey A. Dyachenko, Pavel M. Lushnikov, and Alexander O. Korotkevich. The complex singularity of a stokes wave. *JETP Lett.*, 98(12):767–771, 2013.

[9] L Bergé. Wave collapse in physics: principles and applications to light and plasma waves. *Phys. Rep.*, 303:259 – 370, 1998.

[10] Vladimir E. Zakharov. Stability of periodic waves of finite amplitude on a surface. *J. Appl. Mech. Tech. Phys.*, 9(2):190–194, 1968.

References

[11] Alexander I. Dyachenko, Evgenii A. Kuznetsov, and Vladimir E. Zakharov. Dynamics of free surface of an ideal fluid without gravity and surface tension. *[Plasma Phys. Rep.*, 22(829):916–928, 1996.

[12] George G. Stokes. On the theory of oscillatory waves. *Transactions of the Cambridge Philosophical Society*, 8:441–455, 1847.

[13] George G. Stokes. On the theory of oscillatory waves. *Mathematical and Physical Papers*, 1:197–229, 1880.

[14] George G. Stokes. Supplement to a paper on the theory of oscillatory waves. *Mathematical and Physical Papers*, 1:314–326, 1880.

[15] L. W. Schwartz and J. D. Fenton. Strongly nonlinear waves. *Ann. Rev. Fluid. Mech*, 14:39–60, 1982.

[16] Leonard W. Schwartz. Computer extension and analytic continuation of stokes' expansion for gravity waves. *J. Fluid Mech.*, 62(3):553–578, 1974.

[17] J. F. Toland. On the existence of a wave of greatest height and stokes's conjecture. *Proc. R. Soc. Lond. A*, 363:469–485, 1978.

[18] Malcolm A. Grant. The singularity at the crest of a finite amplitude progressive stokes wave. *J. Fluid Mech.*, 59(2):257–262, 1973.

[19] M. S. Longuet-Higgins and E. D. Cokelet. The deformation of steep surface waves on water i. a numerical method of computation. *Proc. R. Soc. Lond. A*, 350:1–26, 1976.

[20] Michael S. Longuet-Higgins. On an approximation to the limiting stokes wave in deep water. *Wave Motion*, 45:770–775, 2008.

[21] Jianke Yang. Newton-conjugate-gradient methods for solitary wave computations. *J Comput. Phys.*, 228(18):7007–7024, 2009.

[22] Bradley Alpert, Leslie Greengard, and Thomas Hagstrom. Rapid evaluation of nonreflecting boundary kernels for time-domain wave propagation. *SIAM J. Num. Anal.*, 37:1138–1164, 2000.

[23] E. F. Keller and L. A. Segel. Initiation of slime mold aggregation viewed as an instability. *J. Theor. Biol*, 26(3):399–415, 1970.

[24] Miguel A. Herrero and Juan J. L. Velázquez. Singularity patterns in a chemotaxis model. *Math. Ann.*, 306(3):583–623, 1996.

References

[25] Michael P. Brenner, Peter Constantin, Leo P. Kadanoff, Alain Schenkel, and Shankar C. Venkataramani. Diffusion, attraction and collapse. *Nonlinearity*, 12(4):1071–1098, 1999.

[26] S. I. Dejak, P. M. Lushnikov, and I. M. Sigal. Blowup of the Keller-Segel system. *To be published*, 2010.

[27] P. M. Lushnikov. Critical chemotactic collapse. *Phys. Lett. A*, 374:1678–1685, 2010.

[28] G. Wolansky. On steady distributions of self-attracting clusters under friction and fluctuations. *Arch. Rational Mech. Anal.*, 119(4):355 – 391, 1992.

[29] P. H. Chavanis and C. Sire. Exact analytical solution of the collapse of self-gravitating brownian particles and bacterial populations at zero temperature. *Phys. Rev. E*, 93(3):031131, 2011.

[30] Robert W. Boyd. *Nonlinear Optics, Third Edition*. Academic Press, 3rd edition, 2008.

[31] V. E. Zakharov and A. B. Shabat. Exact theory of 2-dimensional sef-focusing and one-dimensional self-modulation of waves in nonlinear media. *Sov. Phys. JETP*, 34:62, 1972.

[32] C. S. Patlak. Random walk with persistence and external bias. *Bull. Math. Biophys.*, 15:311–338, 1953.

[33] E. F. Keller and L. A. Segel. Initiation of slime mold aggregation viewed as an instability. *J. Theor. Biol*, 26(3):399–415, 1970.

[34] W. Alt. Biased random walk models for chemotaxis and related diffusion approximations. *J. Math. Biol.*, 9:147–177, 1980.

[35] Miguel A. Herrero and Juan J. L. Velázquez. Singularity patterns in a chemotaxis model. *Math. Ann.*, 306(3):583–623, 1996.

[36] Michael P. Brenner, Leonid S. Levitov, and Elena O. Budrene. Physical mechanisms for chemotactic pattern formation by bacteria. *Biophys. J.*, 74(4):1677–1693, 1998.

[37] E. Ben-Jacob, I. Cohen, and H. Levine. Cooperative self-organization of microorganisms. *Adv. Phys.*, 49:395–554, 2000.

[38] M. D. Betterton and Michael P. Brenner. Collapsing bacterial cylinders. *Phys. Rev. E*, 64:061904, Nov 2001.

References

[39] J. J. L. Velazquez. Stability of some mechanisms of chemotactic aggregation. *SIAM J. Appl. Math.*, 62(5):1581–1633, 2002.

[40] H. G. Othmer and T Hillen. The diffusion limit of transport equations ii: Chemotaxis equations. *Siam J Appl. Math.*, 62(4):1222–1250, 2002.

[41] C. Sire and P. H. Chavanis. Thermodynamics and collapse of self-gravitating brownian particles in d dimensions. *Phys. Rev. E*, 66(4):046133, 2002.

[42] R. Erban and H. G. Othmer. From individual to collective behavior in bacterial chemotaxis. *Siam J Appl. Math.*, 65(2):361–391, 2005.

[43] T. J. Newman and R. Grima. Many-body theory of chemotactic cell-cell interactions. *Phys Rev. E*, 70:051916, 2004.

[44] S. I. Dejak, P. M. Lushnikov, Yu. N. Ovchinnikov, and I. M. Sigal. On spectra of linearized operators for keller-segel models of chemotaxis. *Physica D*, 241:1245–1254, 2012.

[45] S. I. Dejak, P. M. Lushnikov, and I. M. Sigal. On blowup dynamics in the keller-segel model of chemotaxis. 2009.

[46] T. Hofer, J. A. Sherratt, and P. K. Maini. Virial theorem and dynamical evolution of self-gravitating brownian particles in an unbounded domain. i. overdamped models. *Physica D*, 85:425, 1995.

[47] M. Luca, A. Chavez-Ross, L. Edelstein-Keshet, and A. Mogilner. Chemotactic signaling, microglia, and alzheimer's disease senile plaques: is there a connection? *Bull. Math. Biol.*, 65:693, 2003.

[48] R. Grima. Strong-coupling dynamics of a multicellular chemotactic system. *Phys. Rev. Lett.*, 95:128103, 2005.

[49] V. I. Talanov. Focusing of light in cubic media. *JETP Letters*, 11:199 – 201, 1970.

[50] E. A. Kuznetsov and S. K. Turitsyn. Talanov transformations in self-focusing problems and instability of stationary waveguides. *Phys. Lett. A*, 112A:273–275, 1985.

[51] V. M. Malkin. On the analytical theory for stationary self-focusing of radiation. *Physica D*, 64:251–266, 1993.

[52] G. M. Fraiman. Asymptotic stability of manifold of self-similar solutions on self-focusing. *Sov. Phys. JETP*, 61:228, 1985.

References

[53] B. J. LeMesurier, G. Papanicolaou, C. Sulem, and P. L. Sulem. Focusing and multi-focusing solutions of the nonlinear schrödinger equation. *Physica D*, 31:78, 1988.

[54] V. M. Malkin. Dynamics of wave collapse in the critical case. *Phys. Lett . A*, 151:285, 1990.

[55] F. Merle and P. Raphael. On a sharp lower bound on the blow-up rate for the l^2 critical nonlinear schrödinger equation. *J. Amer. Math Soc.*, 19:37, 2006.

[56] N. E. Kosmatov, V. F. Shvets, and V. E. Zakharov. Computer simulation of wave collapses in the nonlinear schrödinger equation. *Physica D*, 52:16–35, 1991.

[57] G. D. Akrivis, V. A. Dougalis, O. A. Karakashian, and W. R. McKinney. Numerical approximation of blow-up of radially symmetric solutions of the nonlinear schrödinger equation. *SIAM J. Sci. Comput.*, 25:186 – 212, 2003.

[58] Sergey A. Dyachenko, Pavel M. Lushnikov, and Natalia Vladimirova. Logarithmic scaling of the collapse in the critical keller-segel equation, 2013. arXiv.org:1301.5604.

[59] Pavel M. Lushnikov, Sergey A. Dyachenko, and Natalia Vladimirova. Beyond leading-order logarithmic scaling in the catastrophic self-focusing of a laser beam in kerr media. *Phys. Rev. A*, 88:013845, Jul 2013.

[60] S. Dyachenko, A. C. Newell, A. Pushkarev, and V. E. Zakharov. Optical turbulence: weak turbulence, condensates and collapsing fragments in the nonlinear schrodinger equation. *Physica D*, 57:96, 1992.

[61] L. D. Landau and L. M. Lifshitz. *Quantum Mechanics Non-Relativistic Theory, Third Edition: Volume 3*. Butterworth-Heinemann, Oxford, 1981.

[62] L. Bergé and D. Pesme. Time dependent solutions of wave collapse. *Phys. Lett . A*, 166:116, 1992.

[63] M. J. Berger and P. Colella. Local adaptive mesh refinement for shock hydrodynamics. *Journal of Computational Physics*, 82(1):64 – 84, 1989.

[64] Vladimir E. Zakharov, Victor S. Lvov, and Grisha Falkovich. *Kolmogorov Spectra of Turbulence I*. Springer-Verlag, Berlin, 1992.

[65] K. Hasselmann. On the non-linear energy transfer in a gravity-wave spectrum part 1. general theory. *J. Fluid Mech.*, 12(4):481–500, 1962.

References

[66] Mark A. Donelan, J. Hamilton, and W. H. Hui. Directional spectra of wind generated waves. *Phil. Trans. R. Soc. London*, A315:509, 1985.

[67] Paul A. Hwang, David W. Wang, Edward J. Walsh, William B. Krabill, and Robert N. Swift. Airborne measurements of the wavenumber spectra of ocean surface waves. part i: Spectral slope and dimensionless spectral coefficient. *J. Phys. Oceanogr.*, 30:2753–2767, 2000.

[68] Miguel Onorato, A. R. Osborne, M. Serio, D. Resio, A. Pushkarev, Vladimir E. Zakharov, and C. Brandini. Freely decaying weak turbulence for sea surface gravity waves. *Phys. Rev. Lett.*, 89:144501, 2002.

[69] Alexander I. Dyachenko, Alexander O. Korotkevich, and Vladimir E. Zakharov. Weak turbulence of gravity waves. *JETP Lett.*, 77(10):546–550, 2003.

[70] Alexander I. Dyachenko, Alexander O. Korotkevich, and Vladimir E. Zakharov. Weak turbulent kolmogorov spectrum for surface gravity waves. *Phys. Rev. Lett.*, 92(13):134501, 2004.

[71] Alexander O. Korotkevich. Simultaneous numerical simulation of direct and inverse cascades in wave turbulence. *Phys. Rev. Lett.*, 101(7):074504, 2008.

[72] M. Phillips O. The equilibrium range in the spectrum of wind-generated ocean waves. *J. Fluid Mech.*, 4:426–434, 1958.

[73] Paul C. Liu. On the slope of the equilibrium range in the frequency spectrum of wind waves. *Geophys. Res.*, 94(C4):5017–5023, 1989.

[74] Alan C. Newell and Vladimir E. Zakharov. The role of the generalized phillips' spectrum in wave turbulence. *Phys. Lett. A*, 372:4230–4233, 2008.

[75] Alexander O. Korotkevich. Influence of the condensate and inverse cascade on the direct cascade in wave turbulence. *Math. Comput. Simul.*, 82(7):1228–1238, 2012.

[76] Alexander O. Korotkevich and Vladimir E. Zakharov. On the applicability of the hasselmann kinetic equation to the phillips spectrum. *submitted in Nonlin. Proc. Geophys.*, 2013.

[77] `http://fluidmechanics.tudelft.nl/swan/index.htm` SWAN. Swan cycle iii user manual.

[78] L. Cavaleri, J.-H. Alves, F. Ardhuin, A. Babanin, M. Banner, K. Belibassakis, M. Benoit, M. Donelan, J. Groeneweg, T.H.C. Herbers, P. Hwang, P.A.E.M.

References

Janssen, T. Janssen, I.V. Lavrenov, R. Magne, J. Monbaliu, M. Onorato, V. Polnikov, D. Resio, W.E. Rogers, A. Sheremet, J.M. Smith, H.L. Tolman, G. van Vledder, J. Wolf, and I. Young. Wave modeling – the state of the art. *Progress In Oceanography*, 74(4):603–674, 2007.

[79] Alexander I. Dyachenko, Vladimir E. Zakharov, and Evgenii A. Kuznetsov. Nonlinear dynamics of the free surface of an ideal fluid. *Plasma Physics Reports*, 22:829–840, Oct 1996.

[80] Lev V. Ovsyannikov. Dynamics of a fluid. *M.A. Lavrent'ev Institute of Hydrodynamics Sib. Branch USSR Ac. Sci.*, 15:104–125, 1973.

[81] Alexander I. Dyachenko, Evgenii A. Kuznetsov, Michael Spector, and Vladimir E. Zakharov. Analytical description of the free surface dynamics of an ideal fluid (canonical formalism and conformal mapping). *Phys. Lett. A*, 221:73–79, 1996.

[82] Vladimir E. Zakharov, Evgenii A. Kuznetsov, and Alexander I. Dyachenko. Dynamics of free surface of an ideal fluid without gravity and surface tension. *Fizika plasmy*, 22:916–928, 1996.

[83] Vladimir I. Petviashvili. Equation for an extraordinary soliton. *Sov. J. Plasma Phys.*, 2:257–258, 1976.

[84] P. M. Lushnikov. Dispersion-managed soliton in a strong dispersion map limit. *Opt. Lett.*, 26:1535 – 1537, 2001.

[85] Taras I. Lakoba and J. Yang. A generalized petviashvili iteration method for scalar and vector hamiltonian equations with arbitrary form of nonlinearity. *J. Comput. Phys.*, 226:1668–1692, 2007.

[86] John M Williams. *Tables of Progressive Gravity Waves*. Pitman, London, 1985.

[87] Jianke Yang. *Nonlinear Waves in Integrable and Nonintegrable Systems*. SIAM, 2010.

[88] J. Stoer and R. Bulirsch. *Introduction to Numerical Analysis*. Texts in Applied Mathematics. Springer, 2002.

[89] M. A. Herrero, E. Medina, and J. J. L. Velázquez. Finite-time aggregation into a single point in a reaction-diffusion system. *Nonlinearity*, 10(6):1739–1754, 1997.

[90] R. Y. Chiao, I. Garmire, and C. H. Townes. Self-trapping of optical beams. *Phys. Rev. Lett.*, 13:479, 1964.

References

[91] S. N. Vlasov, V. A. Petrishchev, and V. I. Talanov. Averaged description of wave beams in linear and nonlinear media. *Izv. Vys. Uchebn. Zaved. Radiofizika*, 14:1353, 1971.

[92] V. E. Zakharov. Collapse of langmuir waves. *Sov. Phys. JETP*, 35:908, 1972.

[93] V. E. Zakharov and E. A. Kuznetsov. Quasiclassical theory of three-dimensional wave collapse. *Sov. Phys. JETP*, 64:773 – 779, 1986.

[94] P. M. Lushnikov. Dynamic criterion for collapse. *JETP Letters*, 62:461–467, 1995.

[95] E. A. Kuznetsov and V. E. Zakharov. *Wave Collapse.* World Scientific Publishing Company, New York, 2007.

[96] C. Sire and P. H. Chavanis. Critical dynamics of self-gravitating langevin particles and bacterial populations. *Phys. Rev. E*, 78:061111, 2008.

[97] Yu. V. Sidorov, M. V. Fedoryuk, and M. I. Shabunin. *Lectures on the Theory of Functions of a Complex Variable.* Mir Publishers, 1985.

[98] F. W. J. Olver. *Asymptotics and Special Functions.* Academic Press, New York, 1974.

[99] `http://fftw.org`.